FUNDAMENTAL STUDY OF SOLUTION PROCESSED INORGANIC HYBRID THIN FILM SOLAR CELLS

by

Minlin Jiang

Bachelor of Science, Jiangxi Normal University, 2000

Master of Science, Shanghai Jiaotong University, 2009

Master of Science, South Dakota State University, 2012

Submitted to the Graduate Faculty of

Swanson School of Engineering in partial fulfillment

of the requirements for the degree of

Doctor of Philosophy

University of Pittsburgh

2017

UNIVERSITY OF PITTSBURGH

SWANSON SCHOOL OF ENGINEERING

This dissertation was presented

by

Minlin Jiang

It was defended on

February 17, 2017

and approved by

William E Stanchina, PhD, Professor
Department of Electrical and Computer Engineering

Hong Koo Kim, PhD, Professor
Department of Electrical and Computer Engineering

Kevin Chen, PhD, Professor
Department of Electrical and Computer Engineering

Paul Leu, PhD, Associate Professor
Department of Industrial Engineering

Dissertation Director: Guangyong Li, PhD, Associate Professor
Department of Electrical and Computer Engineering

FUNDAMENTAL STUDY OF SOLUTION PROCESSED INORGANIC AND HYBRID THIN FILM SOLAR CELLS

Minlin Jiang, PhD

University of Pittsburgh, 2017

Solar energy is inexhaustible. It's effective and widespread utilization is the way to prevent the Earth from being further polluted. Solar cell has been demonstrated to be the most promising technology to produce electricity by absorbing sunlight, with crystal silicon (c-Si) solar cell leading the market. However, significant amount of energy is required for manufacturing of crystal silicon solar cells because of vacuum-based fabrication process and high consumption of raw materials.

Solution processed thin film solar cells have been considered as promising alternatives to c-Si solar cells because of the low-cost process and low consumption of raw materials. In this work, two types of thin film solar cells (TFSCs), namely Cu_2ZnSnS_4 (CZTS) and $CH3NH3PbI_3$ ($MAPbI_3$) have been explored with a focus on the fabrication and characterization. In the case of

CZTS TFSCs, a promising efficiency of 6.2% has been obtained by modifying a water-based process previously developed. In the case of $MAPbI_3$ TFSCs, an efficiency of 15.39% has been achieved from a spin-coating process. By incorporating with Cl into $MAPbI_3$ thin film, the efficiency was significantly increased to 18.60%. To improve the stability of $MAPbI_3$ TFSCs, a device structure incorporating inorganic metal oxides as charge transport layers (CTLs) has been developed. A promising result with a highly stable and a highly efficient perovskite solar cell was obtained.

The mechanisms behind the improvement were revealed by open-circuit voltage decay (OCVD) measurement, admittance spectroscopy (AS), temperature-dependent open-circuit voltage (V_{OC}), and Kelvin probe force microscopy (KPFM). By comparing the device properties of CZTS solar cells and $MAPbI_3$ solar cells, it was found that the interfaces of these two types of solar cells were crucial in improving their efficiencies. Therefore, interface engineering should be prioritized to further improve the efficiencies of these two PV technologies.

TABLE OF CONTENTS

1.0 INTRODUCTION 1

1.1 SOLUTION-PROCESSED THIN FILM SOLAR CELLS 4

1.1.1 Cu_2ZnSnS_4 (CZTS) 4

1.1.2 $CH_3NH_3PbI_3$ ($MAPbI_3$) 6

1.2 MOTIVATION 9

1.3 CHARACTERIZATION METHODS 10

1.3.1 Open-Circuit Voltage Decay (OCVD) 10

1.3.2 Admittance Spectroscopy (AS) 13

1.3.3 Temperature-Dependent Open-Circuit Voltage 17

1.3.4 Kelvin Probe Force Microscopy (KPFM) 19

2.0 EFFECTS OF SELENIUM VAPOR ANNEALING ON CZTS SOLAR CELLS 21

2.1 EXPERIMENTAL PROCEDURES 22

2.1.1 Materials 22

2.1.2 CZTS Precursor Solution Preparation 23

2.1.3 CZTS Precursor Thin Film Preparation 23

2.1.4 CZTS Thin Film Preparation 24

2.1.5 Device Fabrication 26

2.2 RESULTS AND ANALYSIS 26

3.0 EFFECTS OF CHLORINE DOPING ON MAPBI$_3$ SOLAR CELL 44

3.1 EXPERIMENTAL PROCEDURES 45

3.1.1 Synthesis of CH_3NH_3I (MAI) and CH_3NH_3Cl (MACl) 45

3.1.2 Fabrication of $MAPbI_3$ Solar Cells 46

3.1.3 Characterization 47

3.2 RESULTS AND ANALYSIS 48

4.0 CHLORINE-ASSISTED RECOVERY OF PERFORMANCE LOSS IN MAPBI$_3$ PEROVSKITE SOLAR CELL MADE FROM LOW PURITY PBI$_2$ 66

4.1 EXPERIMENTAL PROCEDURES 67

4.1.1 Fabrication of $MAPbI_3$ Solar Cells using PbI_2 with different purtities.... 67

4.2 RESULTS AND ANALYSIS 67

5.0 IMPROVED STABILITY OF MAPBI$_3$ SOLAR CELLS USING ALL INORGANIC CHARGE TRANSPORT LAYERS (CTLS) 79

5.1 EXPERIMENTAL PROCEDURES 81

5.1.1 Synthesis of ZnO Nanoparticles (NPs) 81

5.1.2 Preparation of Li-doped NiOx (Li:NiOx) sol-gel 81

5.1.3 Fabrication of $MAPbI_3$ solar cell with all inorganic CTLs 82

5.2 RESULTS AND ANALYSIS 83

6.0 FUTURE WORK AND CONCLUSION 92

6.1 FUTURE WORK 92

6.1.1 Interface Engineering of CZTS Solar Cells 92

6.1.2 Interface Engineering of $MAPbI_3$ Solar Cells 93

6.1.3 Effects of impurities in $MAPbI_3$ Solar Cells 98

6.2 CONCLUSION 98

BIBLIOGRAPHY 101

LIST OF TABLES

Table 2.1 Chemical composition of the final CZTS thin film. 28

Table 2.2 Averaged I-V parameters of CZTSSe solar cells... 40

Table 3.1 Elemental ratios of the perovskite solar cells. 50

Table 3.2 I-V parameters of the best perovskite solar cells. 55

Table 5.1 I-V parameters the champion perovskite solar cell with different device structures.... 86

LIST OF FIGURES

Figure 1.1 Market share of different PV technology. 3

Figure 1.2 (a) Schematic structure of CZTS solar cell and (b) band diagram of the CdS/CZTS heterojunction (adopted from [8]).. 5

Figure 1.3 (a,c) Schematic structure and (b,d) band diagram of the perovskite solar cells with different structures (adopted from [20] [21]).. 8

Figure 1.4 Illumination from a sunlight simulator and measured values of Voc at different time (adopted from [35]).. 12

Figure 1.5 (a) Schematic of band bending with one deep trap state, (b) charge density variation through the depletion region due to the trap state, and (c) in response to a changing bias, dV/dt, changes in space charge density dρ/dt can occur at both x_T and W, as indicated (adopted from [37]).. 14

Figure 1.6 (a) Raw data of Admittance Spectroscopy for a CIGS device, (b) The Admittance Spectroscopy data after applying Eq. (2.11), showing the characteristic (peak) frequencies at each temperature, (c) Arrhenius plot of each peak (circles) and the linear fitting (line), (d) DLCP data (circles) in comparison of admittance spectroscopy data (-fdC/df) data (solid line) (adopted from [37]).. 16

Figure 1.7 Temperature dependence of the open circuit voltage (V_{OC}) and its linear extrapolation line to 0 K for the 15.2% efficient CIGS device (dashed line) and the 10.1% efficient CZTS device (solid line), which helps to elucidate the dominant recombination process in the two types of devices [40]... 19

Figure 1.8 Experimental set up and working principle of KPFM (amplitude modulation).......... 20

Figure 2.1 Experimental setup and temperature profile of annealing... 25

Figure 2.2 Growth mechanisms of CZTS thin films.. 27

Figure 2.3 Surface (a~e) and cross section (f~j) SEM images of pre-annealed and annealed CZTS thin films (a & f, Pre-annealed; b & g, Sample-0; c & h, Sample-10; d & i, Sample-20; and e & j, Sample-30) (the scale bar is 1 μm). 29

Figure 2.4 XRD patterns of CZTS thin films. The standard XRD patterns for CZTSSe and CZTS are shown above... 32

Figure 2.5 Raman spectra of pre-annealed and annealed CZTSSe thin films. 33

Figure 2.6 $(ahv)^2$ of the annealed CZTS thin films as a function of hν. 36

Figure 2.7 Experimental and calculated band gap energy versus Se/(S + Se) ratio. 38

Figure 2.8 I-V parameters of CZTSSe solar cells... 39

Figure 2.9 J-V curves of the solar cells with the highest efficiency in each sample. 42

Figure 3.1 Schematic growth process for perovskite thin films using mixed halide sources and method adopted from [79]. 47

Figure 3.2 EDS spectra of the perovskite thin films... 49

Figure 3.3 Top-view SEM images of $MAPbI_3$ and $MAPb(I,Cl)_3$ thin films. 51

Figure 3.4 XRD patterns of $MAPbI_3$ and $MAPb(I,Cl)_3$ solar cells: (a) full range, (b) major peak at (110) to calculate the crystal size.. 53

Figure 3.5 I-V curves and parameters of $MAPbI_3$ and $MAPb(I,Cl)_3$ solar cells (the inset is the efficiency distributions of 16 devices for each sample) measured at around 25℃under simulated sunlight of 100 mW/cm2 （AM 1.5G)... 54

Figure 3.6 Topography AFM images (a and b), SP (c and d), and profiles of SP (e and f) of $MAPbI_3$ (a, c, and e) and $MAPb(I,Cl)_3$ (b, d, and f) thin films on ITO. 56

Figure 3.7 Band alignment of devices for (a) $MAPbI_3$ and (b)$MAPb(I,Cl)_3$. ... 57

Figure 3.8 AFM images, KPFM images, and the profiles along the lines in (a) $MAPbI_3$ and (b) $MAPb(I,Cl)_3$ thin films. ... 59

Figure 3.9 Band diagrams around the GB in $MAPbI_3$ and $MAPb(I,Cl)_3$ thin films. ... 61

Figure 3.10 The electron lifetime as a function of V_{OC}. ... 62

Figure 3.11 Admittance spectroscopy of $MAPbI_3$ and $MAPb(I,Cl)_3$ solar cells: (a) Arrhenius plot of the transition frequencies to derive the defect energy levels, (b) the distributions of the density of the defects. ... 65

Figure 4.1 Averaged I-V curves and parameters of perovskite solar cells (10 devices for each sample). ... 69

Figure 4.2 SEM images of perovskite thin films deposited utilizing different purities of PbI_2. (a) 99.999%, (b) 99%, and (c) 99%+Cl. (The scale bar is 1μm). ... 70

Figure 4.3 (a) XRD patterns, (b) major peak at (110), (c) transmittance, and (d) optical bandgap energies of perovskite thin films utilizing different purities of PbI_2. ... 72

Figure 4.4 The electron lifetime derived from OCVD method as a function of V_{OC}. ... 73

Figure 4.5 Admittance spectroscopy of perovskite solar cell fabricated using low purity PbI_2 with Cl. (a) Capacitance spectra at different temperatures. (b) The derivative of the capacitance spectra which show the transition frequency at each temperature. (c) Arrhenius plot of the transition frequencies to derive the defect energy level. (d) The distribution of the density of the defect... 75

Figure 4.6 Arrhenius plots of the transition frequencies to derive the defect energy levels in perovskite solar cells utilizing different purities of PbI_2. ... 77

Figure 4.7 Defect density distributions of perovskite solar cell fabricated using different purities of PbI_2. ... 78

Figure 5.1 Schematic device structures of (a) conventional, and (b) all inorganic CTLs perovskite solar cells. ... 82

Figure 5.2 AFM images of the surface of (a) Li:NiO_x thin film, (b) ZnO NPs, and (c)perovskite thin film. ... 83

Figure 5.3 Thickness of (a) and (b) Li:NiO_x thin film, (c) and (d) ZnO NPs deposited with 10 times coating. ... 84

Figure 5.4 J-V curves of the champion perovskite solar cell with different device structures. ... 85

Figure 5.5 Energy band diagrams of perovskite solar cells with different device structures of (a) TiO2/spiro-OMeTAD, (b) Li:NiOx/unannealed ZnO NPs, (c) Li:NiOx/annealed ZnO NPs. ... 87

Figure 5.6 Distributions of I–V parameters obtained from 28 perovskite solar cells with device structure of Li:NiO_x/annealed ZnO NPs. ... 88

Figure 5.7 Variation of the normalized I-V parameters of the perovskite solar cells with time stored in air at room temperature without encapsulation. ... 90

Figure 6.1 J-V curves of the champion perovskite solar cells with and without Al-doped ZnO NPs. ... 94

Figure 6.2 The statistical distributions of the Voc of perovskite solar cells with and without Al-doped ZnO NPs. ... 96

Figure 6.3 Temperature dependence of the Voc and its linear extrapolation line to 0 K for perovskite solar cells with and without Al-doped ZnO NPs, which helps to elucidate the dominant recombination process in the two types of devices. ... 97

1.0 INTRODUCTION

Pollution of the earth and shortage of energy sources have been the bottleneck of survival and development for human being since the start of the 21st century. Therefore, lowering energy consumption and protecting the environment have gradually gained attention from all over the world. To keep sustainable development, governments, research institutes, and industries have been fighting for the problems caused by the shortage of available energy sources. It is well known that the best way is to exploit renewable energy resources. Solar energy is considered as the most economic and effective among all available renewable energy resources. Solar energy is inexhaustible and it has already been theoretically and experimentally proved that the earth would not be polluted at all if solar energy was utilized effectively. To encourage and to promote the direct utilization of solar energy, developed countries have been legislating and deploying solar initiatives.

Joint Research Centre (Europe) predicted that energy directly harvested from sunlight would be 20% of total energy consumption in 2050, and this value could be over 50% in 2100. Solar energy will be widely utilized in industries, agriculture and daily life. Photovoltaic (PV) systems have gained tremendous development due to intrinsic advantages as follows:

- Directly translate sunlight into electrical energy;
- Movable parts are dispensable when constructing PV systems;
- Lifetime is over 20 years without any maintenance.

It was reported by Solarbuzz that 16.3 GW PV modules had been shipped to customers in 2010 with the lion's share going to crystalline silicon (c-Si) technology (71%). However, market share of thin film PV technologies has been increasing rapidly due to high cost and energy consumption input in manufacturing c-Si PV of modules. There are three main thin film PV technologies, CdTe, $CuIn_xGa_{1-x}S(Se)_2$ (CIGS), and thin film Si, which has gained 14%, 9%, and 6% of PV market share in 2010, respectively (Fig.1.1) [1]. Nevertheless, thin film Si solar cell has been relatively underdeveloped due to low efficiency and instability from the Staebler–Wronski effect. For the other two thin film technologies, there are restriction on usage of heavy metals such as cadmium, limitations in supply for indium and tellurium, and resultant wide fluctuation in prices of indium and tellurium. These render the combined production capacity of the existing CdTe and CIGS technologies to lower than 100 GW per year, a small fraction of energy consumption, which is expected to be 27 TW by 2050 [1, 2].

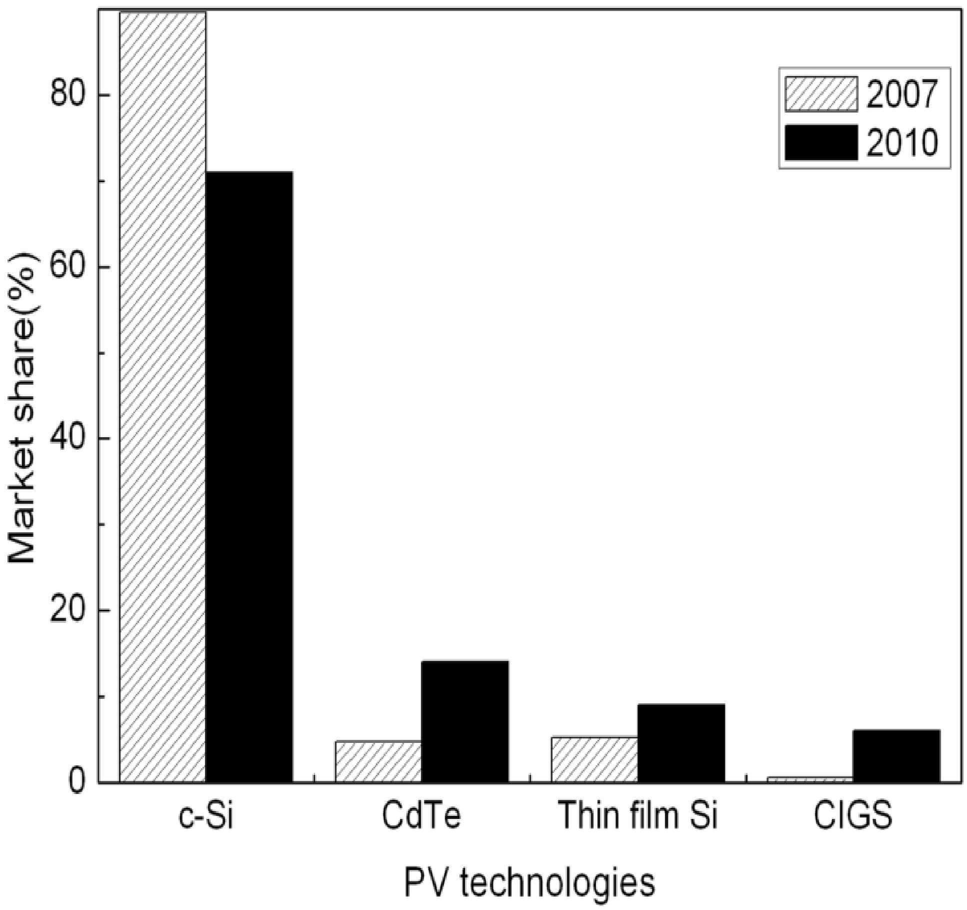

Figure 1.1 Market share of different PV technology.

Recently, quarternary compound Cu_2ZnSnS_4 (CZTS) and methylammonium lead iodide ($CH_3NH_3PbI_3$) ($MAPbI_3$) have been intensively examined as alternative PV materials due to their excellence in material properties and the relative easiness of fabrication process. Both CZTS and MAPbI3 are excellent light absorbers with a high absorption coefficient (> 10^4 cm^{-1}) and a desirable bandgap (~1.50 eV). Most importantly, the highest efficiencies obtained from these two materials were achieved using solution-based processes, indicating low-cost, high-efficiency PV technologies could be realized using these two PV technologies [3] [4].

1.1 SOLUTION-PROCESSED THIN FILM SOLAR CELLS

1.1.1 Cu_2ZnSnS_4 (CZTS)

The first $(I)_2(II)(IV)(VI)_4$ solar cell was developed in 1977 by Wagner and Bridenbaugh [5]. A n-type CdS thin film was evaporation-coated on vapor transportation-grown Cu_2CdSnS_4 single crystal substrate to form the p-n junction. This device showed a short-circuit current density of 7.9 mA/cm^2, an open-circuit voltage of 0.5 V, and a conversion efficiency of 1.6%. The authors pointed out that a large series resistance limited the performance. In 1988, a heterojunction solar cell with an open circuit voltage of 165 mV was achieved by depositing cadmium tin oxide on CZTS thin film [6]. In 1997, the first CZTS TFSC with efficiency of 0.66% was realized by Katagiri using electron beam deposition followed by sulfurization [7].

Most of the reported CZTS solar cells adopt a p-n junction consisting of two different materials with different bandgap energies, which is defined as heterojunction. In the band diagram of a heterojunction, there is a discontinuity in the conduction and valence band edges due to the difference of band gap. As shown in Fig. 1.2, the conduction band offset between CdS and CZTS is a spike where the conduction band edge of CdS lies above that of CZTS [8]. Photogenerated electrons crossing the junction need to tunnel through the spike before they can be collected at the front contact. The efficiency of collection is reduced, leading to increasing of recombination current from tunneling of electrons to interface defects in the CdS. For CZTS solar cell, n-type CdS and p-type CZTS are used to form p-n junction, where external dopants are not needed to make n-type or p-type semiconductors for CZTS solar cell. The above-mentioned CdS and CZTS show n-type conductivity and p-type conductivity, respectively, due to a process called self-doping. For CdS thin film, n-type conductivity was caused by a donor level of 21 meV, which was assigned to excess Cd [78]. Similarly, the commonly observed p-type conductivity in CZTS thin films comes mainly from the Cu_{Zn} antisite defect [9].

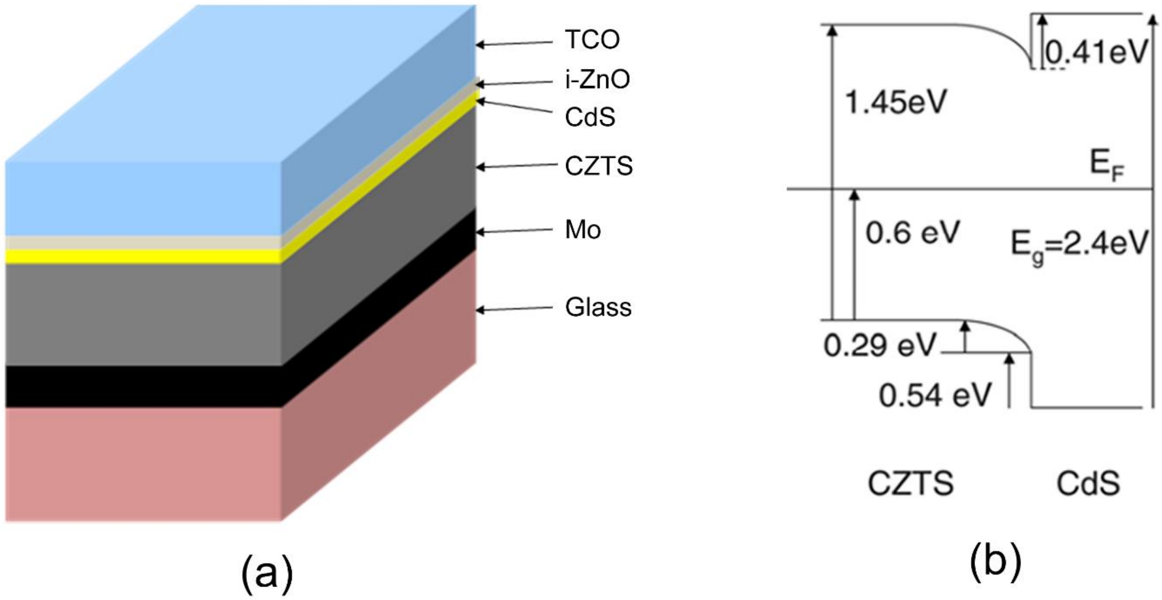

Figure 1.2 (a) Schematic structure of CZTS solar cell and (b) band diagram of the CdS/CZTS heterojunction (adopted from [8]).

The highest efficiency obtained from CZTS is 12.6%, with a Jsc of 35.2 mA/cm^2, a Voc of 0.51V, and a FF of 69.8% [3]. Compared to the record 21.7% CIGS solar cell with similar bandgap, the biggest difference is the Voc [10]. The deficit of Voc, which is defined as the difference between Eg/q and Voc, of the record CZTS solar cell is 0.62V, while that of the record

CIGS solar cell is 0.38V. Finding a way to improve the Voc of CZTS solar cells would significantly increase the efficiency of CZTS solar cells.

The deficit of Voc is mainly affected by the recombination at interfaces of CdS/CZTS, CZTS/Mo, and in the CZTS absorber layer. Polycrystalline CZTS thin film contains a large density of intrinsic defects which is 1.0×10^{16} cm^{-3}, while that of CIGS is 1.3×10^{14} cm^{-3} [11]. The large defect density increases the density of trap states and recombination centers, resulting in the following consequence:

- Diffusion lengths are much shorter than that of silicon wafer-based solar cells. To increase absorption, either a strong optical absorber or multiple junctions must be used. In the case of amorphous silicon solar cell where diffusion lengths are extremely short, p-i-n structure is employed to extend the built-in electric field to aid carrier collection. In the case of organic solar cell where diffusion lengths are even shorter, nanostructure and bulk junction are employed to facilitate carrier collection.
- The presence of defect states in the band gap can limit the built-in voltage due to Fermi level pinning. Also, the presence of defect states will lead to high dependence of minority carrier lifetime and diffusion constant on carrier density.
- The presence of grain boundaries and other intrinsic defects increases the resistivity of CZTS thin films, making the conductivity highly dependent on carrier density.

1.1.2 $CH_3NH_3PbI_3$ ($MAPbI_3$)

The first $MAPbI_3$ solar cell with an efficiency of 3.81% was reported by T. Miyaska in 2009 [12]. Due to the dissolution of $MAPbI_3$ in acetonitrile, the performance degraded quickly under irradiation. Another nonpolar solvent, ethyl acetate, was adopted to prevent the dissolution in 2011

[13]. The performance of $MAPbI_3$ solar cell was improved to 6.54%. It was mentioned that the stability of the $MAPbI_3$ solar cell under continued irradiation was approximately 10 min (about 80% degradation) because $MAPbI_3$ quantum dots tends to be dissolved gradually into the redox electrolyte. A solid hole transporting material (HTM), 2,2',7,7'-tetrakis(N,N-di-pmethoxyphenylamine)-9,9'-spirobifluorene (spiro-OMeTAD) was used to replace liquid electrolyte in 2012 [14]. An efficiency of 9.7% was obtained. Furthermore, compared to the liquid cell, the stability was remarkably improved. A sequential deposition method was developed to deposit $MAPbI_3$ in 2013 and a remarkable efficiency of 15.0% was achieved [15]. In the same year, an evaporation deposition method was applied to fabricate $MAPbI_3$ thin film [16]. The efficiency was further improved to 15.4%. Since then, numerous groups have shifted their research focuses to investigate $MAPbI_3$ solar cells. The efficiency of perovskite solar cells has been surprisingly rapidly improved from 3.8 % in 2009 [12] to 20.1% in 2015 [4]. This great advance is mainly attributed to the rigorous efforts that worldwide research groups have been taking to deposit high quality perovskite thin films [17-19]. The tremendous improvement can also be attributed to the two device structures developed for almost 20 years. One structure is based on TiO_2 as electron transport layer (ETL) and spiro-OMeTAD as hole transport layer (HTL) (Fig. 1.3 (a) and (b)) [20]. The other structure is based on organic ETL such as PCBM and organic HTL such as poly(3,4-ethylenedioxythiophene) polystyrene sulfonate (PEDOT:PSS) and poly(3-hexylthiophene-2,5-diyl) (P3HT) (Fig. 1.3 (c) and (d)) [21]. The perovskite thin film is deposited in between as absorber layer to fabricate perovskite solar cells. Due to the high sensitivity of these organic materials to moisture and oxygen, a nitrogen glove box with strict control on the concentration of moisture and oxygen was usually used to fabricate perovskite solar cells [17, 22-

25]. However, the perovskite solar cells reportedly degraded quickly once they were removed from the nitrogen glove box and stored in ambient environment [26-28].

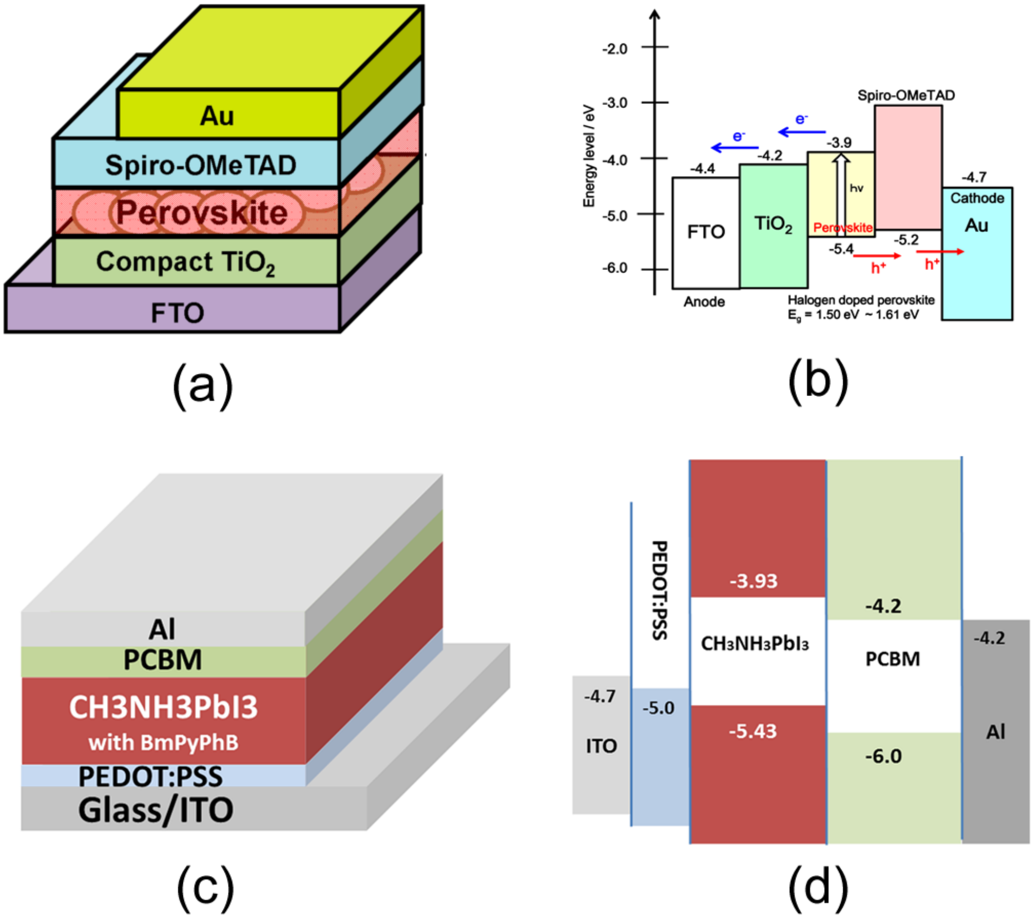

Figure 1.3 (a,c) Schematic structure and (b,d) band diagram of the perovskite solar cells with different structures (adopted from [**20**] [**21**]).

Although $MAPbI_3$ TFSCs have evolved from the dye sensitized solar cell (DSSC) and adopted a device structure similar to bi-layer organic solar cells, it has been found recently that they work differently from organic solar cells [29]. The strong and abroad absorption spectrum, the long diffusion length of minority carriers, the large two-carrier recombination rate, and the polycrystalline structure observed in $MAPbI_3$ thin films indicate that $MAPbI_3$ TFSCs function more like inorganic polycrystalline solar cells such as $Cu(In,Ga)Se_2$ (CIGS) solar cells. The diffusion length of CIGS thin film was estimated to be around 1μm [30]. Passivation of grain boundaries (GBs) by sodium incorporation in polycrystalline CIGS thin film is recognized to be one of the mechanisms for increasing the diffusion length. Similarly, it was observed that the diffusion length of MAPbI3 solar cell was significantly increased by doping MAPbI3 thin films with negligible amount of Cl. However, the mechanisms behind this improvement are unclear. Admittance spectroscopy (AS) has been successfully employed to study the defect density of CIGS and CZTS thin films [31, 32]. As mentioned earlier, polycrystalline CZTS thin film contains a large density of intrinsic defects which is 1.0×10^{16} cm^{-3}, while that of CIGS is 1.3×10^{14} cm^{-3} [11]. Similar fundamental studies should be conducted on $MAPbI_3$ solar cells.

1.2 MOTIVATION

Most of the reported CZTS TFSCs were fabricated either by highly expensive vacuum-based methods, or by highly toxic and flammable solvent-based methods. Fabrication process based on low-cost nonvacuum-based methods and environmentally friendly chemicals such water is needed. For $MAPbI_3$ TFSCs, due to the high sensitivity of the organic charge transport layers to moisture and oxygen, the ultimate advancement in the device stability of perovskite solar cells has yet to be realized. Device structure with inorganic charge transport layers should be developed to improve the stability of $MAPbI_3$ TFSCs.

In addition, the research focus of CZTS and $MAPbI_3$ TFSCs has been on development of new fabrication methods. The working mechanisms of the devices have been rarely addressed in literatures. Considering the solution-based method used to achieve more than 20% MAPbI3 solar cells [4], it would be interesting to investigate the device properties of $MAPbI_3$, such as carrier lifetime and defect density. Not only fundamental studies on these fields are necessary to advance the perovskite PV technologies, but also the results can be utilized as a guidance to improve the performance of solution-processed CZTS solar cells.

1.3 CHARACTERIZATION METHODS

1.3.1 Open-Circuit Voltage Decay (OCVD)

The open-circuit voltage decay (OCVD) method was developed to measure the minority carrier lifetime in solar cells [33]. This technique has certain advantages over frequency or steady-state-based methods [33]. First, the lifetime as a function of V_{OC} at high-voltage resolution can be obtained continuously. Second, this technique does not require special treatment on samples, which are kept undamaged during the measurement. Finally, the data processing is relatively simple. To obtain minority carrier lifetime, only one first derivative is required.

The solar cell is initially under a constant illumination generated from a sunlight simulator (Fig. 1.4). The V_{OC} is continuously measured. Minority carriers are injected into the base region during the illumination. Upon the blockage of the illumination, the V_{OC} starts to decay due to the recombination of minority carriers. To theoretically explain the mechanism, a p$^+$-n junction, where the conductivity of the p$^+$-region is much greater than that of the n-region, is considered [34]. Let p_n be the hole density present in the n-region under thermal equilibrium conditions, and Δp be the excess hole density injected due to the illumination in the n-region at the boundary of the junction transition region. The total hole density at the junction boundary will be

$$p = p_n + \varDelta p. \tag{2.1}$$

From the theory of the p-n junction, the hole density in the n-region at the junction boundary is given by

$$p = p_n e^{qV/kT}, \tag{2.2}$$

where V is the junction voltage. Combing 2.1 and 2.2, the junction voltage V can be obtained:

$$V = (\frac{kT}{q}) ln(1 + \left(\frac{\varDelta p}{p_n}\right)). \tag{2.3}$$

Assuming the excess carrier concentration, $\varDelta p$, decays exponentially according to a single effective lifetime, τ_e, namely,

$$\varDelta p = \varDelta p_0 e^{-t/\tau_e}, \tag{2.4}$$

where $\varDelta p_0$ is the excess carrier density at the specific time when the illumination is blocked. The junction voltage at $t=0$ (at the specific time when the illumination is blocked), V_0, is

$$V_0 = (\frac{kT}{q}) ln(1 + \left(\frac{\varDelta p_0}{p_n}\right)). \tag{2.5}$$

Combing 2.3 and 2.2, and 2.5, the junction voltage, or the V_{OC}, as a function of time, t, can be obtained from:

$$V_{oc} = (\frac{kT}{q}) ln(1 + \left(e^{qV_0/kT} - 1\right) e^{-t/\tau_e}). \tag{2.6}$$

Usually $qV_0 \gg kT$ Eq. 2.6 can be simplified to

$$V_{oc} = (\frac{kT}{q}) ln(1 + e^{\frac{qV_0}{kT} - t/\tau_e}). \tag{2.7}$$

Assuming $-t/\tau_e$ is small, Eq. 2.7 can be further simplified to

$$V_{oc} = (\frac{kT}{q})(\frac{qV_0}{kT} - t/\tau_e). \tag{2.8}$$

Therefore, the effective carrier lifetime can be obtained as

$$\tau_e = -\frac{kT}{q} \times \frac{1}{\frac{dV_{oc}}{d_t}}. \tag{2.8}$$

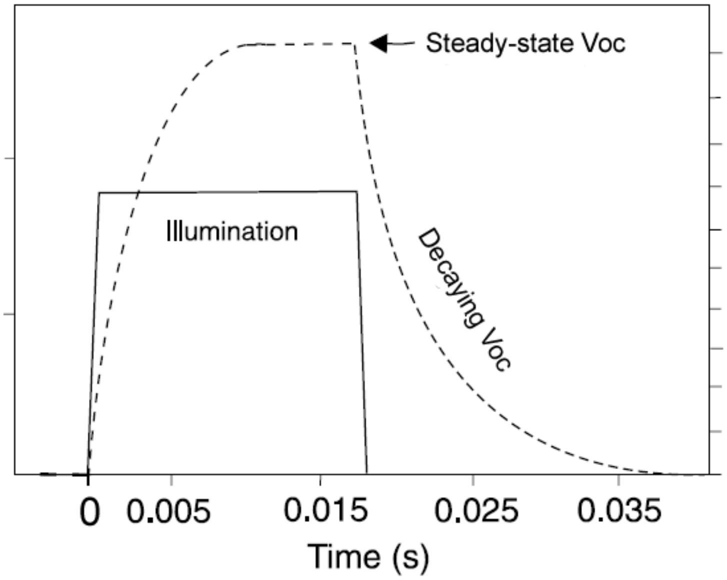

Figure 1.4 Illumination from a sunlight simulator and measured values of Voc at different time (adopted from [**35**]).

1.3.2 Admittance Spectroscopy (AS)

Admittance Spectroscopy is a technique which measures the sample capacitance, C, as a function of applied AC frequency, f, and temperature, T. This technique can yield the thickness of the film, the position of the Fermi energy in the bulk, the energetic position of dominant defect bands that occur between the Fermi energy and mid-gap, and an estimate of the density of those states [36].

The diode capacitance is traditionally analyzed using the depletion approximation, which assumes that that the depletion region is precisely defined, ends abruptly, and is fully depleted of free carriers. In the depletion approximation, the depletion width will vary with applied bias, but the charge density ρ(x) within the depleted region remains constant (where x is measured through the depth of the film, with $x=0$ at the interface), while the bulk region remains neutral. Then, as long as the free carrier relaxation time is short compared with the applied ac frequency, the capacitance response originates from the depletion edge, giving

$$C = \varepsilon\varepsilon_0 A/W \ , \tag{2.9}$$

where W is the width of the depletion region, A is the area of the device, and ε is the semiconductor dielectric constant.

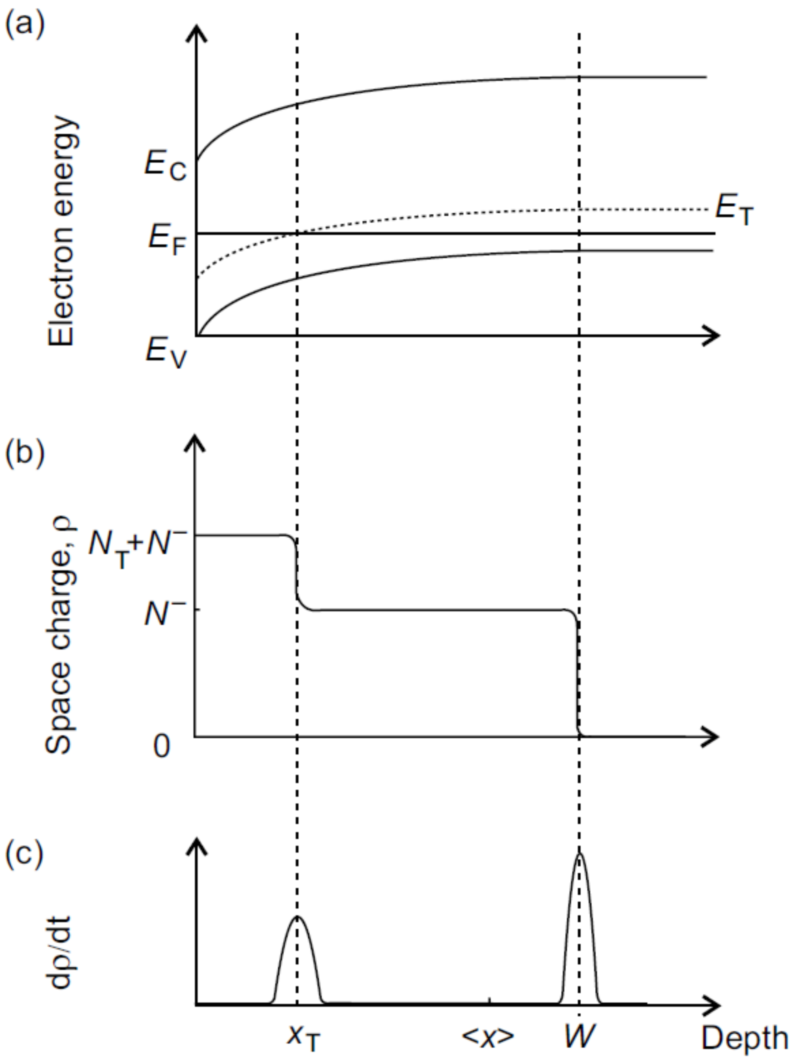

Figure 1.5 (a) Schematic of band bending with one deep trap state, (b) charge density variation through the depletion region due to the trap state, and (c) in response to a changing bias, *dV/dt*, changes in space charge density *dρ/dt* can occur at both x_T and *W*, as indicated (adopted from [**37**]).

When energy level, E_T, with a density of N_T is present deeper in the band gap in the bulk, x_T as shown in Fig. 1.5, the depletion approximation no longer necessarily holds true, and carrier capture and emission from these states must also be considered [37]. However, when the temperature of the sample is too low, or the frequency applied is too high, there is no time for carriers in the bulk to drift in and out of the depletion edge in response to the applied AC voltage. Under this circumstance, the capacitance response will be that of the bulk dielectric,

$$C = \varepsilon\varepsilon_0 A/h \, , \tag{2.10}$$

where h is the distance between the top and back contacts. Increasing the temperature, T, or decreasing the frequency, f, the capacitance will be changed to that shown in Eq. 2.9. A step will be observed in the C-f curves as shown in Fig. 1.6 (a). For electron traps, the electron emission rate, e_n is given by

$$e_n = \gamma\sigma_{na}T^2\exp(-\frac{E_{na}}{kT}) \, , \tag{2.11}$$

where σ_{na} is the capture cross section for electrons, E_{na} is the activation energy of the trap state referenced to the conduction band edge. The characteristic time of the capacitance measurement is defined by the angular frequency of the applied ac voltage, ω, such that states with emission rates $e_n > \omega$ respond to the applied ac voltage. The cut-off energy, E_e , can be derived from

$$\omega = \gamma\sigma_{na}T^2\exp(-\frac{E_e}{kT}) \, . \tag{2.12}$$

Only trap states with activation energy E_{na} up to the cut-off energy E_e will respond dynamically to the applied ac voltage. For a specific defect energy level with activation energy E_{na}, only ω and T are changeable in Eq. 2.12 which can be transformed into

$$ln\frac{\omega}{T^2} = \ln(\gamma\sigma_n) - E_e\frac{1}{kT} \, . \tag{2.13}$$

By taking first derivative of Eq. 2.13, we can get

$$\frac{d\omega}{dE_e} = -\frac{\omega}{kT}, \tag{2.14}$$

$$\frac{dC}{dE_e} = \frac{d\omega}{dE_e}\times\frac{dC}{d\omega}. \tag{2.15}$$

Combining Eqs. 2.14 and 2.15, we get

$$\frac{dC}{dE_e} = -\frac{\omega}{kT}\frac{dC}{d\omega}. \quad (2.16)$$

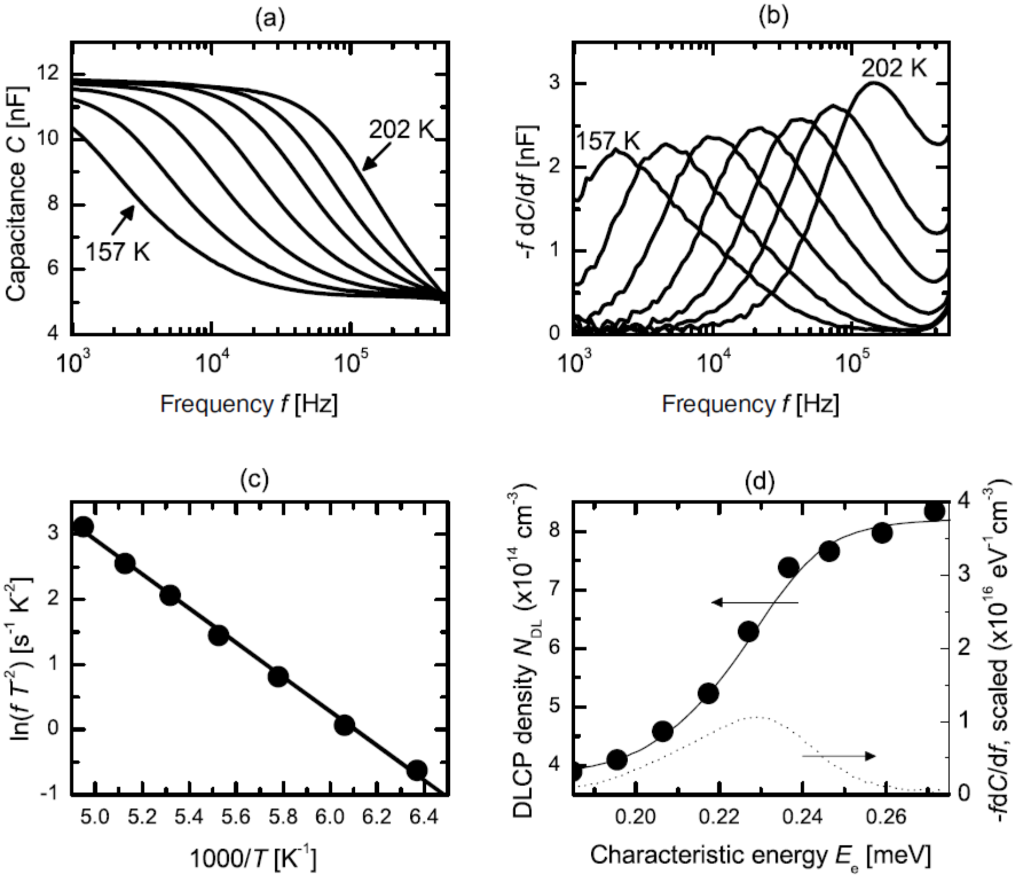

Figure 1.6 (a) Raw data of Admittance Spectroscopy for a CIGS device, (b) The Admittance Spectroscopy data after applying Eq. (2.11), showing the characteristic (peak) frequencies at each temperature, (c) Arrhenius plot of each peak (circles) and the linear fitting (line), (d) DLCP data (circles) in comparison of admittance spectroscopy data (-fdC/df) data (solid line) (adopted from [**37**]).

By applying Eq. 2.16 to the admittance spectroscopy data shown in Fig. 2.3 (a), the characteristic frequencies at each temperature can be obtained as shown in Fig. 1.6 (b). The ($ln\frac{\omega}{T^2}$, $\frac{1}{\mathrm{kT}}$) data points from each peak can then be plotted on an Arrhenius plot as shown in Fig. 1.6 (c). Using Eq. 2.13 to linearly fit the data, the slope then yields the activation energy $\mathrm{E_{na}}$, while the intercept can be used to derive the capture cross section σ_{na}. The trap density, $\mathrm{N_t}$, versus $\mathrm{E_e}$ can be obtained by rescaling the ω axis to $\mathrm{E_e}$ by the following equation:

$$N_t = -\frac{V_{bi}}{qW}\frac{dC}{d\omega}\frac{\omega}{kT}\,, \tag{2.17}$$

where $\mathrm{V_{bi}}$ is the built-in voltage, W is the thickness of the intrinsic layer.

1.3.3 Temperature-Dependent Open-Circuit Voltage

As introduced earlier, both CZTS and $\mathrm{MAPbI_3}$ thin films are polycrystalline. The corresponding PV devices are considered heterojuction solar cells since the p-n junctions in these devices form between two different semiconductors. One diode model has been developed to describe and analyze the *J*-*V* behaviors of these thin film solar cells [38, 39].

The forward current density of the heterojunction under illumination, *J*, is described by

$$J = J_0 \exp\left(\frac{qV}{AkT}\right) - J_{ph}\,, \tag{2.18}$$

where J_0 is the saturation current density of the diode, J_{ph} is the photocurrent, V is the applied voltage, A is the ideality factor, and $\frac{kT}{q}$ is the thermal voltage, a constant of 26 meV. J_0 is caused by the recombination process, which is highly temperature dependent. Therefore, J_0 can be described by

$$J_0 = J_{00}\exp\left(\frac{-E_a}{AkT}\right)\,, \tag{2.19}$$

where J_{00} is the temperature dependent prefactor, while E_a is the activation energy of the recombination.

By combining Eq. 2.18 and 2.19, we get

$$J = J_{00}\exp(\frac{-E_a}{AkT})\exp(\frac{qV}{AkT}) - J_{ph} \ . \tag{2.20}$$

When the illuminated solar cell is short-circuited, the forward current density J is named as short-circuit current density, J_{sc}, which is approximately equal to J_{ph}:

$$J_{sc} \approx J_{ph} \ . \tag{2.21}$$

When the illuminated solar cell is open-circuited, the forward current density J is zero, while the voltage V is named as open-circuit voltage, V_{oc}, which can be expressed as:

$$V_{oc} = \frac{AkT}{q}\ln(\frac{J_{ph}}{J_0}) \ . \tag{2.22}$$

By combining Eq. 2.21 and 2.22, we get

$$V_{oc} \approx \frac{AkT}{q}\ln(\frac{J_{sc}}{J_0}) \ . \tag{2.23}$$

By combining Eq. 2.19 and 2.23, we get

$$V_{oc} \approx \frac{E_a}{q} - \frac{AkT}{q}\ln(\frac{J_{00}}{J_{sc}}) \ . \tag{2.24}$$

Assuming A, J_{sc}, and J_{00} are independent of the temperature T, a plot of V_{oc} versus T should yield a straight line and the extrapolation to $T=0\ K$ gives the activation energy E_a [40]. By comparing the value of E_a with the bandgap energy of the absorber layer in the solar cell, E_g, the dominant recombination process can be figured out. If the value of E_a equals to E_g, the recombination in the bulk dominates. If the value of E_a is less than E_g, the recombination in the interface dominates [40].

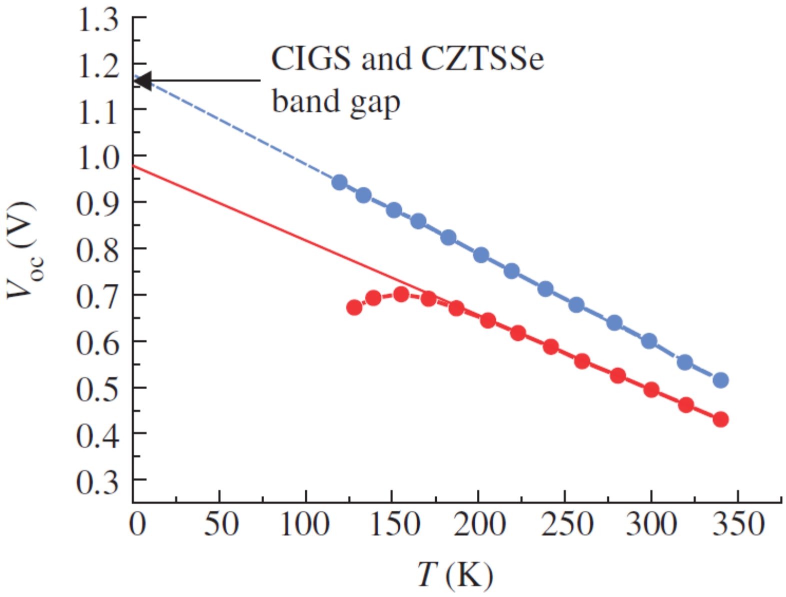

Figure 1.7 Temperature dependence of the open circuit voltage (V_{OC}) and its linear extrapolation line to 0 K for the 15.2% efficient CIGS device (dashed line) and the 10.1% efficient CZTS device (solid line), which helps to elucidate the dominant recombination process in the two types of devices [**40**].

1.3.4 Kelvin Probe Force Microscopy (KPFM)

KPFM is an advanced mode of atomic force microscopy (AFM) that can simultaneously measure the local topography and SP distribution of samples with a lateral resolution in nano scales. Its applications are widely found in semiconductor devices especially in solar cells [41-44]. In the characterization of cross-sectional surfaces of solar cells, one of the most commonly used techniques is to bias the solar cell with different DC voltages [44, 45]. As pointed out by Chen *et al.*, SP distribution within a cell under illumination in an open-circuit condition is equivalent to the SP distribution within the cell when it is measured in dark while being forward biased at its open circuit voltage [45]. This indicates that, by biasing a solar cell with different voltages in dark, we can study the SP distribution of the cell at its operating condition. In this work, a single-path scan KFPM, Agilent SPM 5500, was used in the characterization of planar perovskite solar cells. All KPFM measurements were carried out in dark ambient condition with different DC biases provide by a power supply. Shown in Figure 1 is the experimental set up and the working principle of KPFM. Cathodes of planar perovskite solar cells were connected to the common ground of KPFM and power supply while various DC bias voltages were applied to the anodes of perovskite solar cells. In operation, KPFM system records the DC voltages biased to its conductive probe at the point when the electrostatic force between probe and sample is nullified at the electrical frequency. The corresponding DC values can then be further processed to acquire SP distribution of the sample [46].

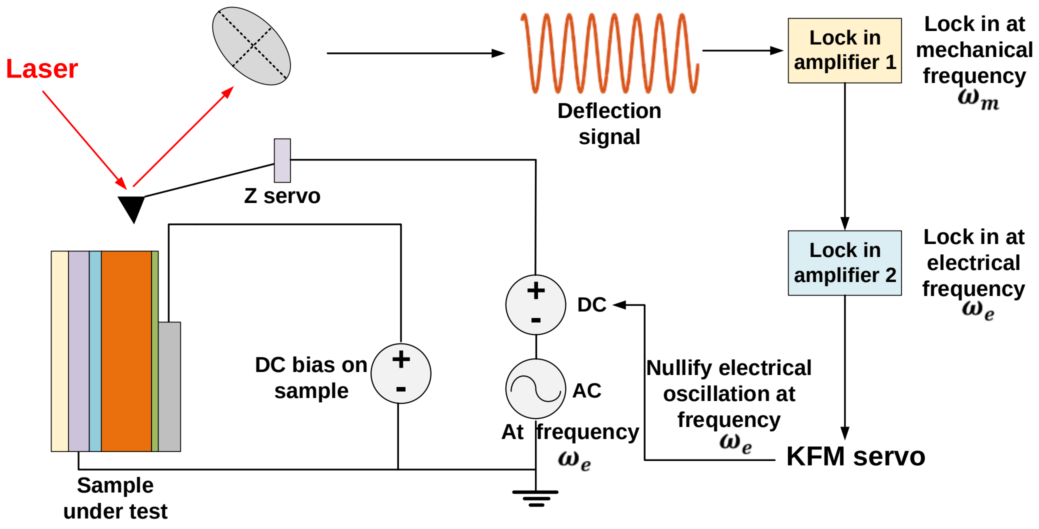

Figure 1.8 Experimental set up and working principle of KPFM (amplitude modulation).

2.0 EFFECTS OF SELENIUM VAPOR ANNEALING ON CZTS SOLAR CELLS

Kesterite $Cu_2ZnSn(S,Se)_4$, or CZTSSe, is one of the most promising materials for high-efficiency, low-cost thin film solar cells. Efficiency of more than 12% has been reported for CZTSSe solar cell using a hydrazine-based solution process [47]. Efficiency greater than 9% was also achieved with CZTSSe solar cells using a coevaporation method [48]. Among various deposition techniques for CZTSSe thin films, solution-based processes have attracted more attention than vacuum-based methods because of their potential low cost. Significant progress has been achieved on CZTSSe thin film solar cells using solution-based methods [49-53].

Yang et al. reported a CZTSSe solar cell, fabricated from a spin-coated hydrazine-based sol gel, with an efficiency of 8.08% [53]. Here, a sol gel containing Cu_2S, SnS_2, Zn, and S was prepared by mixing each constituent dissolved in hydrazine into final ratios of Zn/Sn = 1.2 and Cu/(Zn + Sn) = 0.8. Additionally, Cao et al. reported a CZTSSe solar cell fabricated from a spin-coated CZTSSe precursor ink, containing nanoparticles of Cu_7S_4, ZnS, and SnS dispersed in hexanethiol [54]. The device showed an efficiency of 8.5%. Ki et al. reported an efficiency of 4.1% from a CZTSSe solar cell fabricated using CZTSSe precursor solution [55]. The clear, light yellow CZTSSe precursor solution contained $Cu(CH_3COO)_2 \cdot H_2O$, $ZnCl_2$, $SnCl_2 \cdot 2H_2O$, and thiourea dissolved in dimethyl sulfoxide. Most of the reported solution-based methods rely on non-aqueous solvents such as hydrazine and organic solvents. In the case of hydrazine, toxicity and flammability necessitates careful handling and extreme caution. For organic solvents, carbon is often left in the CZTSSe thin film after annealing, a problem that degrades the solar cell's performance.

We have recently developed a novel water-based, solution-processed method for Cu_2ZnSnS_4 (CZTS) thin film solar cells [56-58]. In this method, commercially available metal chlorides and thiourea are dissolved in water to create a CZTS precursor solution which can be easily deposited on substrates by spin-coating. The efficiency of the water-based, solution-processed CZTS solar cell was low but promising, considering its environmental safety and potential low cost. The performance of the water-based, solution-processed CZTS solar cell has been significantly improved by introducing Se vapor into the annealing chamber [59].

To investigate the mechanisms behind the significant improvement brought by the introduction of Se vapor, CZTSSe thin films and solar cells were obtained from CZTS precursor thin films. These were deposited by a water-based method and annealed with Se vapor for varied durations. The morphological, structural, compositional, and optical properties of CZTSSe thin films were examined. The correlation of CZTSSe solar cell performance with different processing conditions was also investigated.

2.1 EXPERIMENTAL PROCEDURES

2.1.1 Materials

Copper(II) chloride dihydrate (99.99%), zinc chloride (99.99%), tin(II) chloride dihydrate (99.99%), thiourea (99.0%), selenium powder (99.99%), and ethanol (99.5%) were purchased from Sigma Aldrich and used directly without further purification. Deionized water (DI-water) (16 MΩ) was produced in an in-house system.

2.1.2 CZTS Precursor Solution Preparation

The coating solution was prepared by dissolving copper(II) chloride dihydrate (1.12 mmol), zinc chloride (0.75 mmol), tin(II) chloride dihydrate (0.75 mmol), and thiourea (6 mmol) into a mixture solution containing DI-water (2 ml) and ethanol (1ml) at room temperature. A clear solution was obtained after stirring at room temperature for 20 min.

2.1.3 CZTS Precursor Thin Film Preparation

The CZTS precursor solution was spin-coated on low alkaline glass substrates and Mo-coated low alkaline glass substrates. The scanning electron microscopy (SEM) images, optical properties, and Raman spectra of CZTS thin films were obtained from the samples deposited on low alkaline glass substrates. X-ray diffraction (XRD) patterns and device fabrication were conducted using the samples deposited on Mo-coated low alkaline glass substrates. Drying at 110 ℃ in air evaporated the solvents in the as-coated films. Pre-annealing at 250 ℃ in a N_2-filled tube furnace decomposed CZTS precursors for generating metal sulfides (copper sulfide, zinc sulfide, and tin sulfide) nanocrystals. The spin-coating and drying processes as well as pre-annealing were repeated several times to deposit CZTS thin films with designated thickness.

2.1.4 CZTS Thin Film Preparation

The pre-annealed CZTS precursor thin films were placed in a tube furnace. A ceramic box containing Se powder was placed in a separate tube furnace to generate Se vapor; this vapor was simultaneously transported by N_2 flow to the annealing tube furnace (Fig. 2.1(a)). The temperature of the tube furnace was raised to 550 ℃ to grow CZTS polycrystalline thin films (Fig. 2.1(b)). The growth was allowed for 30 min as determined by our optimization tests. The amounts of Se incorporated into the CZTS thin films were controlled by changing the time of introducing Se vapor (Sample-0: no Se vapor was applied, Sample-10: Se vapor was applied for 10 min, Sample-20: Se vapor was applied for 20 min, Sample-30: Se vapor was applied for 30 min) (Fig. 2.1(c)). After cooling under the protection of N_2, CZTS samples were immediately transferred to a vacuum-connected dessicator for later use.

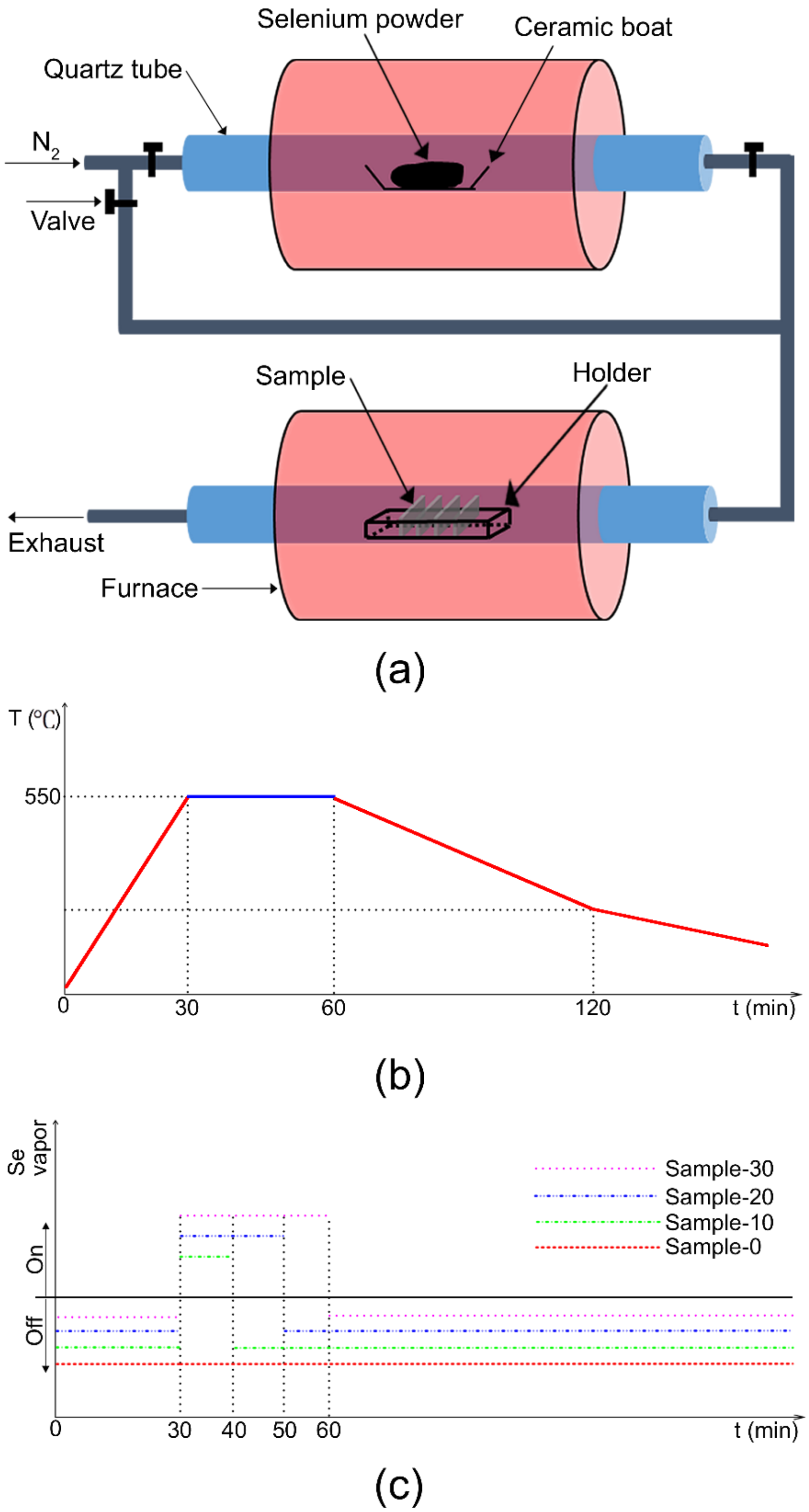

Figure 2.1 Experimental setup and temperature profile of annealing.

2.1.5 Device Fabrication

The CZTS devices were completed using a similar structure as conventional CIGS solar cells [60]. CdS, intrinsic ZnO (i-ZnO), indium-doped tin oxide (ITO), and Ag electrodes were sequentially deposited on CZTS thin films. CdS was coated on the CZTS thin film by chemical bath deposition (CBD). The CZTS samples were vertically inserted into a beaker containing aqueous solution of CdI_2 (1.4 mM), $CS(NH_2)_2$ (0.14 M), and NH_4OH (1 M). The solution was heated to 60 ℃, and the reaction was kept for 12 min. Samples were taken out and cleaned in DI-water. The coating procedures needed to be repeated once to grow CdS thin film with a total thickness of 50 nm. RF sputtering was then used to deposit 60 nm of i-ZnO and 200 nm of ITO. Electron beam evaporation was applied to deposit the Ag electrode with a thickness of 200 nm through a shadow mask. Four CZTS solar cells on each sample were fabricated after mechanical scribing.

2.2 RESULTS AND ANALYSIS

The growth mechanisms of CZTS thin films by the water-based, solution-processed method employed in this paper are illustrated in Fig. 2.2 and summarized below. As demonstrated in Fig. 2.2 (a), ions of Cu^{2+} are reduced to Cu^{+} in the solution of thiourea (tu) dissolved in water [61]. Ions of Cu^{+} then react with thiourea to form $[Cu_2(tu)_6]Cl_2 \cdot 2H_2O$ complex [62]. Similarly, ions of Zn^{2+} and Sn^{2+} react with thiourea to form $ZnCl_2(tu)_2$ complex and $Sn_2(Cl)_4(tu)_5 \cdot 2H_2O$ complex, respectively [63]. These complexes are heated to 250 ℃ under the protection of N_2 and decompose into volatile products such as COS, CS_2, NH_2CN, HNCS, NH_3, HCN, HCl, SO_2, and metal sulfide nanoparticles. These volatile products are discharged from the samples with the flow of N_2. Lastly, samples mainly containing copper sulfide, zinc sulfide, and tin sulfide nanoparticles are annealed at 550 ℃ in N_2. These metal sulfide nanoparticles react to grow polycrystalline CZTS thin films in the presence of Se vapor [64].

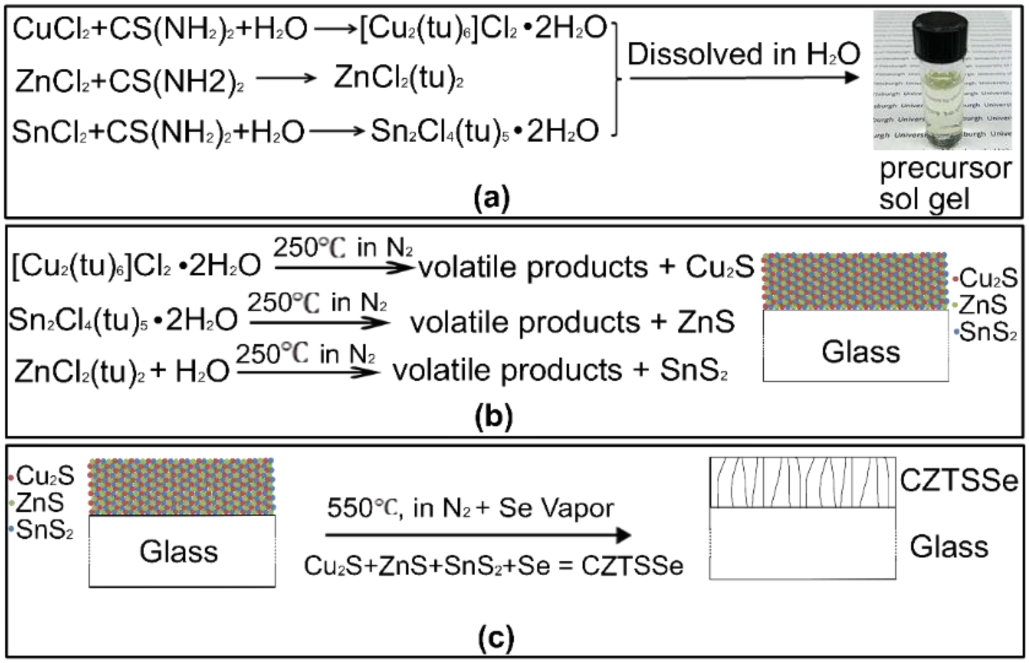

Figure 2.2 Growth mechanisms of CZTS thin films.

Table 2.1 Chemical composition of the final CZTS thin film.

Sample	Cu/(Zn+Sn)	Zn/Sn	Se/(S+Se)
Pre-annealed	0.83	1.12	0
Sample-0	0.88	1.24	0
Sample-10	0.84	1.30	0.08
Sample-20	0.90	1.27	0.19
Sample-30	0.81	1.28	0.25

For the study on the influence of Se vapor feeding, four CZTS precursor thin film samples (pre-annealed) were prepared. The compositions of the pre-annealed and annealed samples were analyzed using EDX and summarized in Table 2.1. The elemental ratios in the pre-annealed sample were carefully controlled by changing the concentrations of raw materials in the CZTS precursor solution. Subsequently, the ratios of Cu/(Zn+Sn) and Zn/Sn were comparable to those reported in highly performed CZTS solar cells [47, 48]. All annealed samples were copper-poor, zinc-rich, which is beneficial to compress the formation of binary phases such as Cu_2S, and to generate self-doped p-type conductivity in CZTS thin films [65]. The ratios of Cu/(Zn+Sn) and Zn/Sn were slightly increased compared to those of pre-annealed sample due to the loss of Sn. The depletion of Sn was not severe because the annealing process was conducted in atmospheric pressure, which helps to minimize the loss of Sn as suggested in literatures [66, 67]. The ratio of Se/(Se+S) was increased by prolonging the Se vapor time during annealing, indicating more atoms of S were replaced by those of Se in CZTS crystals grown with longer Se vapor introducing time. A generally increasing trend in the loss of Sn was observed when the Se vapor introducing duration was increased. This can be attributed to the increase of Se concentration as suggested by P. Salomé et al. who reported that more Se incorporation into CZTS thin films promotes formation of Se compounds and therefore promotes the evaporation of Sn over Zn [66].

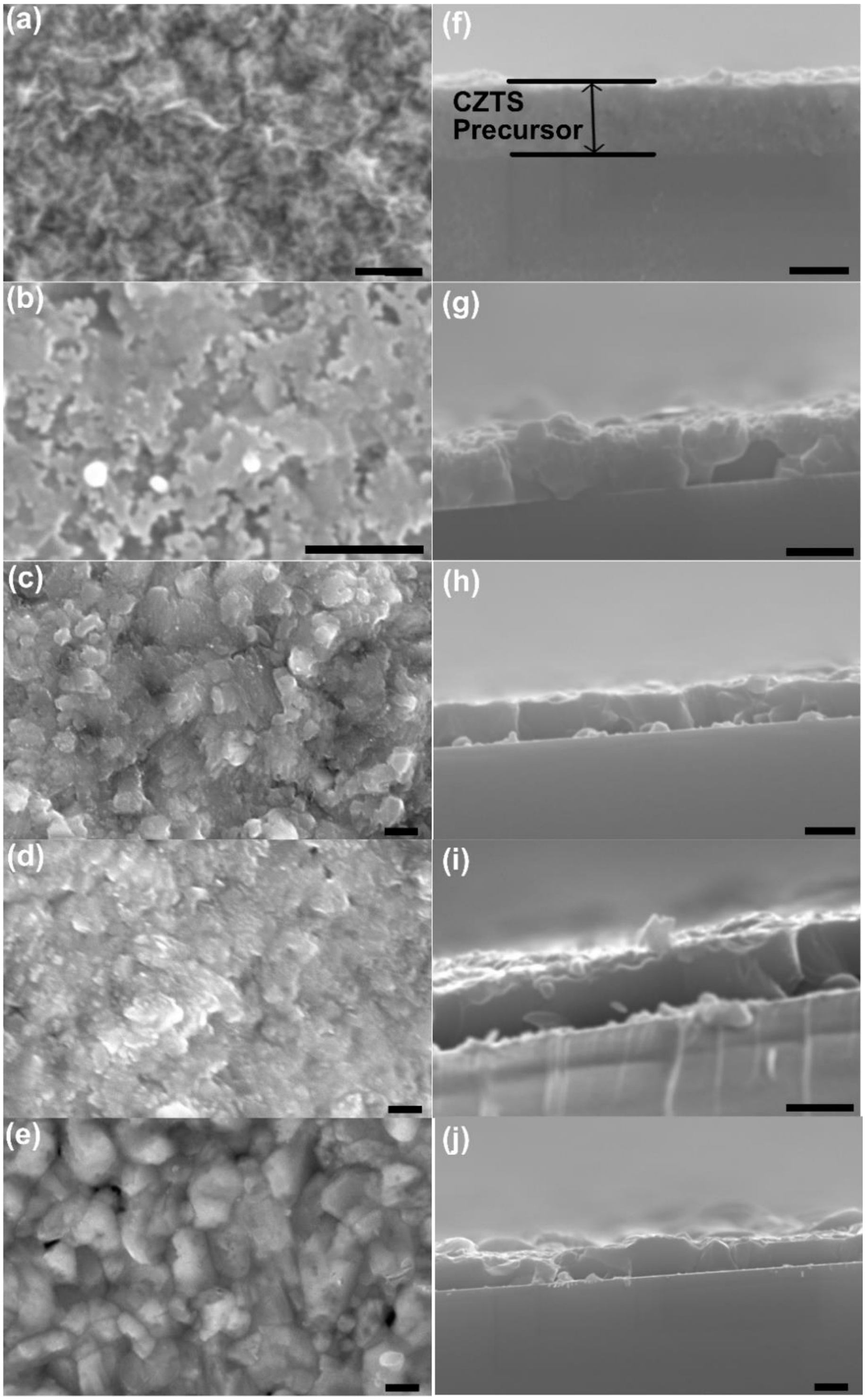

Figure 2.3 Surface (a~e) and cross section (f~j) SEM images of pre-annealed and annealed CZTS thin films (a & f, Pre-annealed; b & g, Sample-0; c & h, Sample-10; d & i, Sample-20; and e & j, Sample-30) (the scale bar is 1 μm).

To suppress the loss of Sn, it was suggested that the deposition of CZTS thin films should be conducted at temperatures below 550 °C and a following annealing step should be applied in an inert gas atmosphere to improve crystal quality [68]. Also, introducing vapor of SnS_2 into the annealing chamber was proven to be effective to reduce the loss of Sn [69]. However, it remains unresolved to what extent the loss of Sn could be endured without detrimental effects on the performance of CZTS solar cells, since CZTS solar cells with promising efficiency have been successfully fabricated with a large variation of composition [70].

The SEM surface and cross section images of pre-annealed CZTS films are shown in Fig. 2.3 (a) and (f). The pre-annealed sample consisted of a mixture of nanoparticles of metal sulfides (Cu_xS, Zn_xS, and Sn_xS), which makes it extremely difficult to delineate the grain boundaries because of the relatively low resolution of the SEM system. As seen in Fig. 2.3 (b) and (g), larger CZTS crystals were produced after annealing at high temperatures. Cracks and voids are observed in the pure CZTS thin films, common features in solution-based CZTS thin films due to volume contraction caused by evaporation of raw materials [71, 72]. The thickness of the Sample-0 is less than 1μm, while the pre-annealed sample has a thickness greater than 1μm, indicating a significant amount of material was evaporated during annealing. Fewer cracks and voids were formed in the samples annealed with Se vapor as observed in the SEM surface and cross section images of Se-incorporated CZTS films which are shown in Fig. 2.3 (c)~(e) and Fig. 2.3 (h)~(j), respectively. Larger crystals and more compact CZTS thin films were obtained when the duration of Se feeding process was extended. Two mechanisms contribute to this improvement of morphology. First, the volume contraction caused by the loss of raw materials during annealing is possibly alleviated by the incorporation of Se into the CZTS thin film. Some S atoms were substituted by larger Se atoms. The unit cell of the crystal was expanded after selenization, which helps shrink the voids commonly encountered in solution-based deposition methods. Another explanation is that Se is a better vapor-transport agent than S for this material system, which might have a more dramatic effect on grain growth than the expansion of the unit cell. This hypothesis is supported by the results reported by S. Riha et al. who deposited CZTS thin films by annealing pure CZTS nanocrystals and Se-rich CZTS nanocrystals coated on substrates [73]. It was found that no transport was observed during annealing for pure CZTS nanocrystal films; however, in some cases of Se-rich CZTS films, material was completely transported off the substrate into the quartz tube. These results indicate that introducing Se vapor into the annealing chamber helps enhance the grain growth of CZTS thin films.

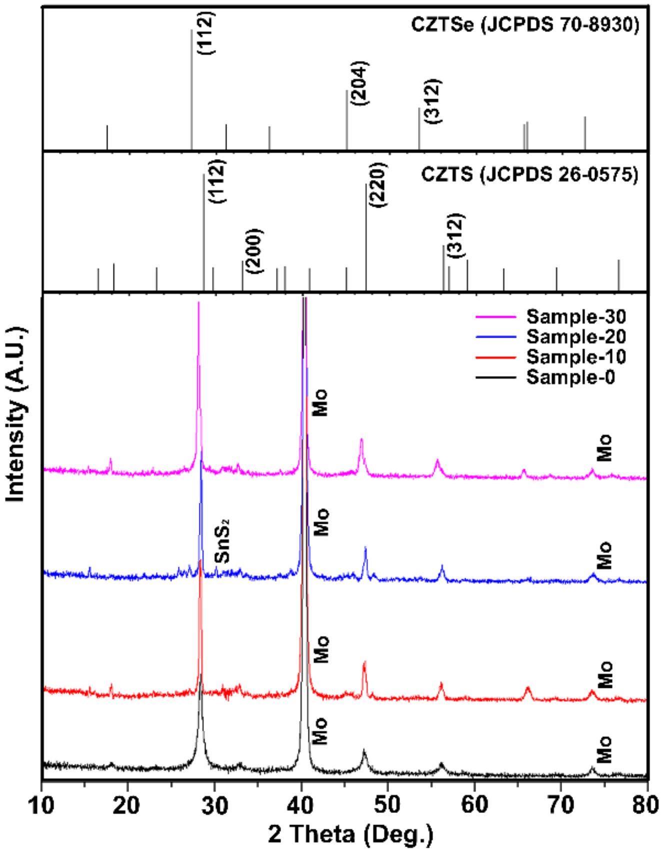

Figure 2.4 XRD patterns of CZTS thin films. The standard XRD patterns for CZTSSe and CZTS are shown above.

The XRD patterns of the samples together with the standard pattern of CZTSe (JCPDS 52-0868) and CZTS (JCPDS 26-0575) are presented in Fig. 2.4. For sample-0, the diffraction peaks can be indexed to those of kesterite CZTS which has a tetragonal structure with three major peaks of (112), (204), and (312). The diffraction peaks of the samples annealed with Se vapor present shift to lower values of 2θ and move closer to those of CZTSe. As the Se vapor introducing duration was extended, more S atoms (1.84 Å) were replaced by larger Se atoms (1.98 Å), leading to an increase in the lattice constant.

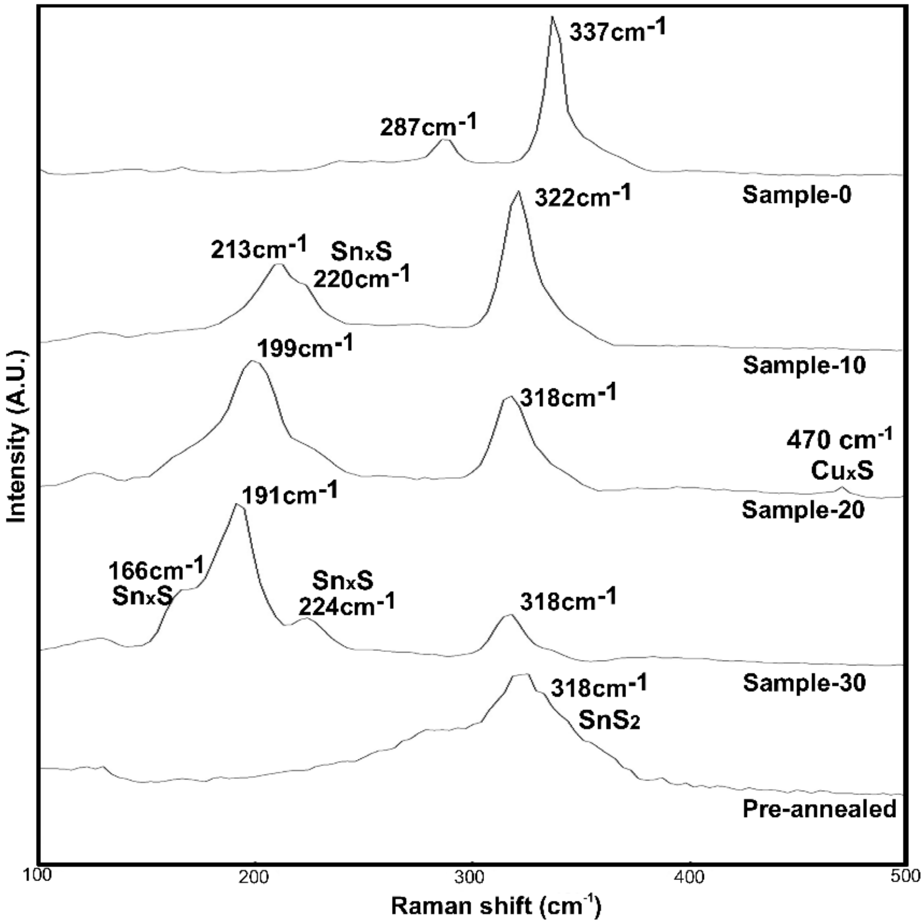

Figure 2.5 Raman spectra of pre-annealed and annealed CZTSSe thin films.

The Raman scattering spectra of pre-annealed samples and samples annealed with Se vapor are plotted in Fig. 2.5. Pre-annealed samples exhibited a prominent peak at 318cm^{-1} that was assigned to SnS_2. This pattern is highly similar to what was observed for a multilayer of $Cu_2S/SnS_2/ZnS$ deposited using atomic layer deposition, indicating that the pre-annealed sample mainly consists of a mixture of nanoparticles of metal sulfides as observed in the SEM images [74]. After annealing in N_2 at 550 °C for 30 min without Se vapor, the main peak shifted to 337 cm^{-1}, and another peak at 287 cm^{-1} was also observed. However, peaks of some secondary phases such as Sn_xS and Cu_xS were also observed as shown in Fig. 4.4 [75, 76]. A peak at 470 cm^{-1} in Sample-20 can be assigned to Cu_xS [77]. This is associated with the fact that Sample-20 had the highest ratio of Cu/(Zn+Sn); a high concentration of Cu resulted in phase precipitation in the form of Cu_xS. For the annealed samples with Se vapor, two main peaks originated from CZTS, shifted towards each other and following the same trend as reported for CZTS with an intermediate S/Se ratio [78].

Secondary phases in CZTS thin films are detrimental to the performance of CZTS solar cells. Firstly, secondary phases such as ZnS have a much larger band gap than CZTS. The large difference in band gap will lead to a mismatch in energy levels of the valence band and conduction band. Internal barriers between secondary phases and CZTS will be formed, which is expected to degrade the performance of the PV device. Secondly, the density of grain boundaries will be increased due to the segregation of secondary phases from the CZTS phase in the polycrystalline thin film absorber layer. The recombination occurring at the grain boundaries is consequently intensified, leading to degraded PV device parameters, such as short-circuit current density (J_{SC}) and fill factor (FF). Lastly, the presence of Cu_xS in CZTS thin films will facilitate the formation of shorting paths in the absorber layer between the front contact and the back contact due to the commonly observed high conductivity of Cu_xS [79]. As a result, the J_{SC} will be significantly decreased. Strategies have been proposed to eliminate secondary phases in CZTS thin films. The first proposal is to strictly control the CZTS thin film composition. One study conducted on the phase diagram of the Cu_2S–ZnS–SnS_2 system by I. Olekseyuk et al. revealed that CZTS only existed in this system as a single phase over a very narrow range of composition varying no more than ±1.5 % absolute from the stoichiometric values for each element [80]. Any large deviation from the stoichiometric values will result in formation of secondary phases. This gives an explanation to why the secondary phases were widely detected in CZTS thin films grown by different methods. Since the elimination of secondary phases during growth of CZTS thin film is extremely difficult, chemical routes have been developed to remove secondary phases after the deposition of CZTS thin films. M. Bar et al. reported that the surface composition of CZTS thin films was significantly altered after KCN etching was applied [79]. This alteration in composition mainly comes from a preferred etching of Cu and, to a lesser degree, Sn. A less toxic chemical approach based on HCl was developed to selectively etch Zn-rich secondary phases on the surface of CZTS thin films [81]. This etching process demonstrated a significant impact on the performance of the solar cells by increasing the J_{SC} and decreasing the series resistance, R_S. Similar approaches are being explored for the CZTS thin films deposited using the same process as reported in this work. Results will be reported elsewhere.

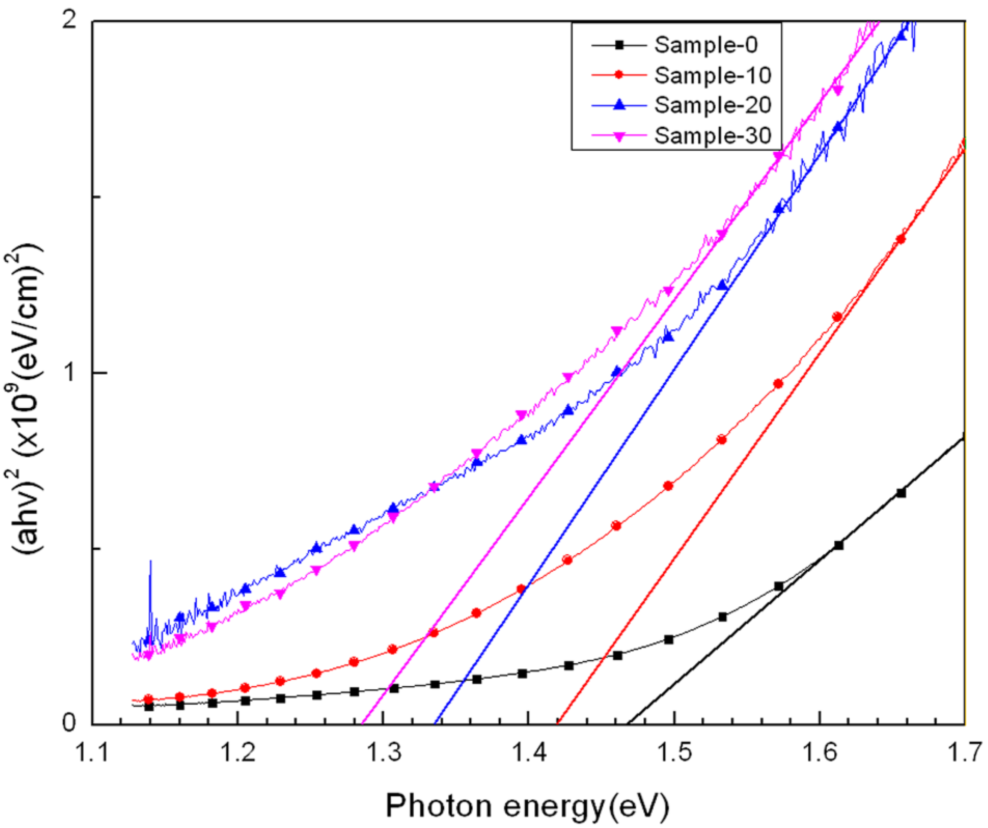

Figure 2.6 $(ahv)^2$ of the annealed CZTS thin films as a function of hv.

The bandgaps were determined by linearly extrapolating $(ahv)^2$ versus photon energy (hv) (Fig. 2.6). Sample-0 had a bandgap of 1.47 eV, a value close to those reported in literatures concerning pure CZTS thin films [82]. For three Se-included CZTS samples, the band gaps were 1.42, 1.34, and 1.28eV, respectively, showing a decreasing trend as the Se vapor introducing time was lengthened. The narrowing of the bandgap partly originated from the enhancement of crystal size when more Se atoms were incorporated into the CZTS thin film to facilitate the growth of crystal. Nevertheless, to a large extent, the decrease of the bandgap was a result of the unit cell expansion due to the substitution of S atoms in CZTS by Se atoms. Although no definite conclusion has been made in literature about the effects of Se inclusion on the optical bandgap of CZTS thin films and nanoparticles as presented earlier, further increasing the concentration of Se is expected to reduce the bandgap of CZTS thin film. A value of ~1.5 eV has been reported on the bandgap of pure CZTS thin films deposited by different methods. While discrepancies on the bandgap of pure CZTSe thin films exist in literature, a value of ~1.0 eV has been widely recognized on the bandgap of pure CZTSe thin films deposited by different methods [82, 83]. It was suggested that the existence of some secondary phases such as ZnSe were the possible reason for the difference in overall bandgap of CZTSe thin films. A simple model to determine the relationship between the ratio of Se/(Se+S) and the bandgap of CZTS nanoparticle was adopted by H. Wei et al. from the model developed by M. Bär et al. to derive the optical bandgap for penternary $Cu(In_{1-x}Ga_x)(S_ySe_{1-y})_2$ (CIGSSe) alloys from its Ga/(Ga+In) ratio as well as from its S/(S+S) ratio [84, 85]. The model is extended to determine the optical bandgaps for penternary CZTSSe alloys, E_g^{CZTSSe}, from its Se/(Se+S) ratio using the linear approximation between the bandgap of the pure CZTS, E_g^{CZTS}, and the bandgap of the pure CZTSe, E_g^{CZTSe}:

$$E_g^{CZTSSe}(x) = (1-x)E_g^{CZTS} + xE_g^{CZTSe} - bx(1-x), \tag{4.1}$$

which is corrected by the alloy specific “optical bowing constant” b. Assumption of a band gap value of 1.5eV for CZTS and 1.0eV for CZTSe was applied in the calculation. The bandgaps derived from the transmittance data were used to calculate the constant b which varied from 0.4 to 0.5. Therefore, different values of b (0.4 and 0.5) were applied in the calculation of the bandgaps for CZTS with a Se/(Se+S) ratio changing from 0 to 1.

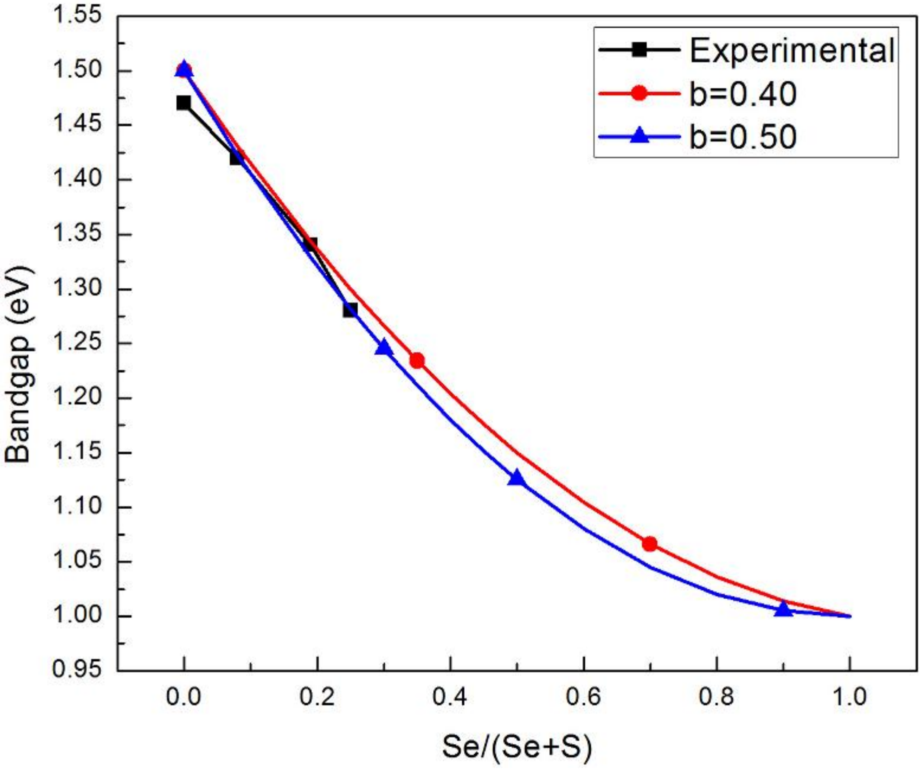

Figure 2.7 Experimental and calculated band gap energy versus Se/(S + Se) ratio.

As shown in Fig. 2.7, the bandgap of CZTS thin films decreases with the increasing of Se concentration nonlinearly. High efficiencies have been obtained from solution-based CZTS thin film absorber layers where the bandgap was determined to be around 1.1 eV from the external quantum efficiency (EQE) data [86]. This value indicates a high level of substitution of S by Se during annealing. The authors reported that around 90% of S atoms were replaced by Se atoms, while a substitution level of 60% was derived from the model based on our results. Regardless of which is more accurate, compared to the highest substitution level of 25% obtained in Sample-30, the ratio of Se/(Se+S) in the reported solution-based high-performance CZTS solar cells was undoubtedly higher, indicating that further incorporation of Se can be achieved by adjusting the annealing process. The bandgap of CZTS thin films can be conveniently tuned, and the growth of CZTS crystals will be enhanced, which is expected to improve the performance of CZTS thin film solar cells.

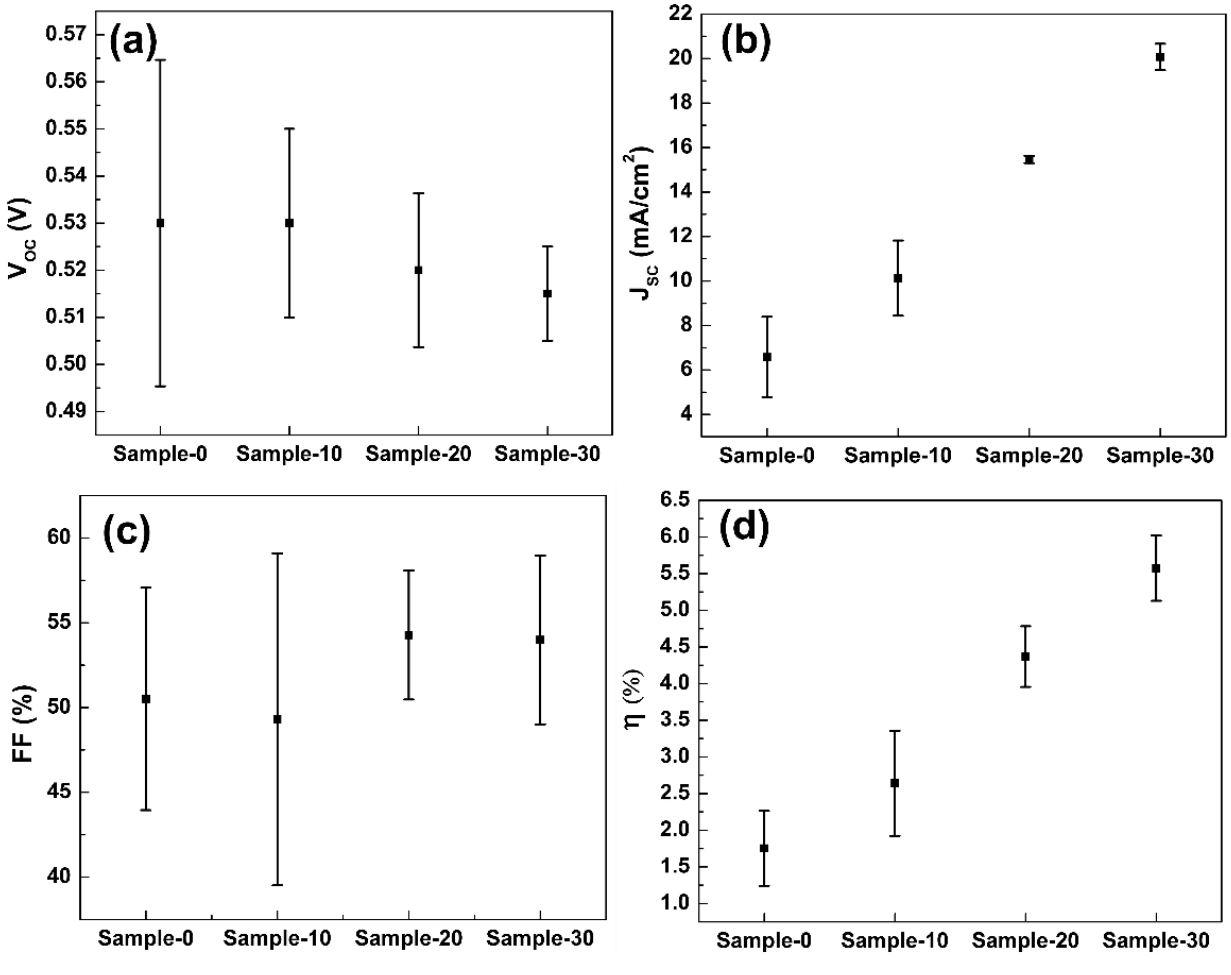

Figure 2.8 *I-V* parameters of CZTSSe solar cells.

Table 2.2 Averaged *I-V* parameters of CZTSSe solar cells.

Sample	V_{OC} (V)	J_{SC} (mA/cm^2)	FF (%)	η (%)
Sample-0	0.53±0.03	6.58±1.80	50.51±6.56	1.75±0.51
Sample-10	0.53±0.02	10.13±1.69	49.30±9.79	2.64±0.72
Sample-20	0.52±0.02	15.46±0.16	54.23±3.80	4.37±0.41
Sample-30	0.52±0.01	20.07±0.59	53.99±4.98	5.57±0.44

Fig. 2.8 displays the variation of the PV parameters of completed devices, corresponding to CZTS absorber layers grown under Se vapor with varied durations. The averaged PV parameters of CZTS solar cells are also summarized in Table 2.2. While general nonuniformity of open-circuit voltages (V_{OC}) existed in all samples, the highest V_{OC} of each sample decreased as the Se vapor feeding time was increased, which can be attributed to the decreasing trend in the bandgap. The deficits in V_{OC} (defined as difference between the optical band gap and the highest V_{OC} for each sample) for the four samples are 0.91, 0.88, 0.80, and 0.76 V, respectively. These values are much higher than the 0.5 V commonly observed for CIGS solar cells, indicating the recombination at the interfaces such as CZTS/CdS and Mo/CZTS is possibly dominant [77]. Modification of the interfaces between the active layer with the buffer layer and the back metal electrode is expected to increase the V_{OC}. The V_{OC} obtained from the four samples were higher than those reported on CZTS thin film solar cells. This can be mainly attributed to the comparably lower S substitution levels obtained in the Se vapor feeding process, leading to a higher bandgap, a major impact factor for V_{OC} in inorganic solar cells. Further extending the Se vapor feeding duration is expected to decrease the Voc.

Significant enhancement was achieved on J_{SC} of CZTS solar cells with longer Se vapor feeding duration. The J_{SC} was increased from around 8 mA/cm^2 in CZTS solar cells fabricated without Se vapor present to more than 20 mA/cm^2 in Sample-30, which was annealed under Se vapor for 30 min. Although the red shift of the onset wavelength and the higher absorption coefficients seen in the absorbance of Sample-30 contributed to the increase of J_{SC}, the improvement on the optical properties alone is not likely to significantly boost the J_{SC}. The enhancement in crystal size and the passivation of the grain boundaries by Se-rich surfaces are most likely the two critical driving forces for J_{SC}. The former helps improve J_{SC} in a way that the recombination is reduced due to lower the density of grain boundaries associated with large grain domains. The latter leads to a lower bandgap surface layer where the potential barriers are removed for grain-grain carrier transport. Similar to the nonuniformity in V_{OC}, the FF was also widely distributed. This was partly caused by the nonuniformity of CdS deposited on CZTS thin film. The size of the samples used in this work was 1"×1", while the volume of the solution where CdS was deposited was 150 ml. Upgrading of the CBD setup is expected to fabricate CZTS solar cells with more uniform PV parameters. The highest FF of each sample increased with greater Se introducing times. This is partly related to the series and shunting resistances since the electrical properties of the CZTS thin films are highly dependent on the ratio of Se/(Se+S). Mainly due to the significant improvement of J_{SC}, the CZTS solar cells obtained from the CZTS thin films annealed with Se vapor showed remarkably improved efficiencies.

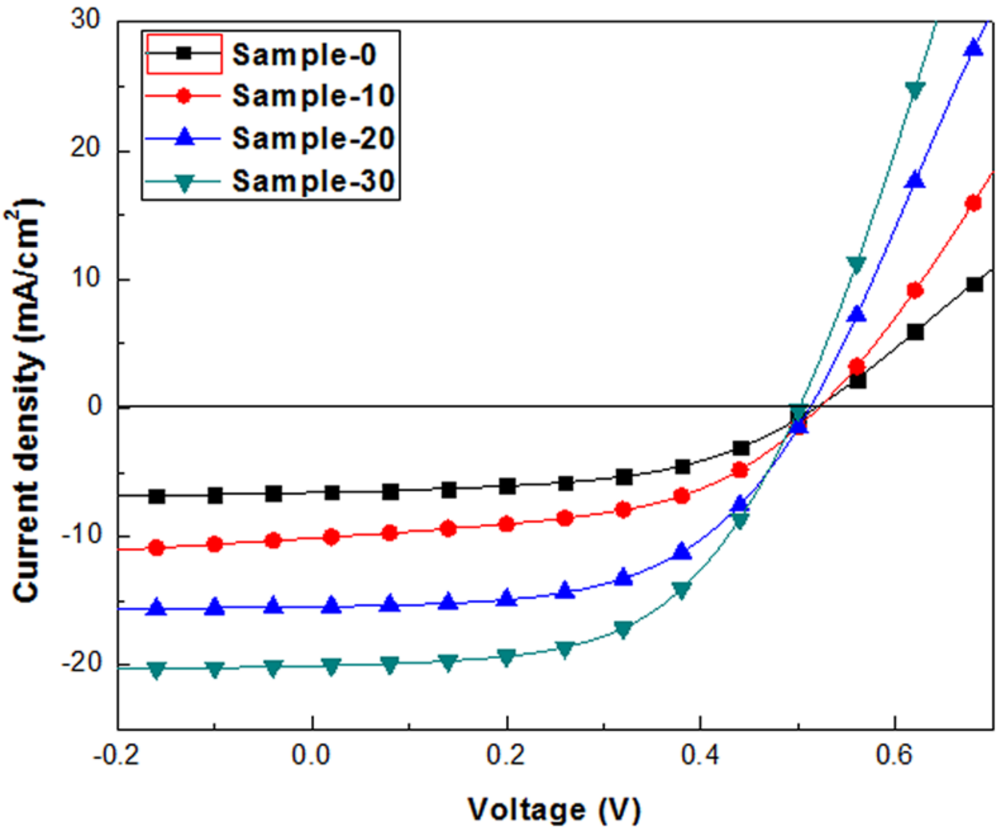

Figure 2.9 J-V curves of the solar cells with the highest efficiency in each sample.

The J-V curves of the highest efficiency obtained from each sample are shown in Fig. 2.9. The best CZTS solar cell, Sample-30, exhibited an efficiency (η) of 6.16% with a V_{OC} of 0.50V, a J_{SC} of 20.06mA/cm^2, and a FF of 61.37%. Compared to the pure CZTS solar cells without Se inclusion, the performance of the CZTS thin film solar cell is impressive, signifying that the selenization step is necessary to achieve high performance for solution-based CZTS solar cells. However, compared to other solution-based CZTS solar cells such as IBM's hybrid slurry method (11.1%) and Dupont's nanocrystal dispersion (8.5%), there is much room to improve the efficiency

[54, 86]. Three more issues could be readily addressed to further improve the efficiency of the water-based, solution-processed CZTS solar cell. Firstly, diffusion of sodium from soda lime glass was also found to profoundly affect grain size, crystal texture, and conductivity of CZTS thin films. Replacing the low alkaline glass substrates used in this work with soda lime glass substrates may further improve the performance of CZTS solar cells [87]. Secondly, the layers of CdS and ZnO were prepared using process parameters optimized for CIGS solar cells [60]. Optimization of these layers will possibly further improve the performance of CZTS solar cells. Lastly, while further extending the Se vapor feeding duration could enhance the incorporation of Se into CZTS thin films and presumably lead to higher efficiency, it is difficult to be realized at this stage because the total annealing time of 30 min is the presently optimized. This must be done in conjunction with the modification of other process parameters, such as lowering the annealing temperature and increasing the Se vapor pressure. Corresponding experiments are under way and expected to fabricate CZTS thin film solar cells with higher efficiencies.

3.0 EFFECTS OF CHLORINE DOPING ON $MAPBI_3$ SOLAR CELL

Methylammonium lead halide perovskites have emerged as promising photovoltaic (PV) materials because of their excellent optical properties such as high absorption coefficients for a broad range of sunlight absorption. Also, the abundance of raw materials and the ability of being solution processed make methylammonium lead halide perovskites more suitable for low cost PV technologies. High power conversion efficiencies of more than 15% have been reported from both mesoporous structure devices and planar structure devices. The planar structure devices are more advantageous than the mesoporous structure devices because high temperature annealing necessary for mesorporous structure is not required for planar structure devices. Thus, low temperature processing, which is suitable for plastic solar cells, can be applied to fabricate methylammonium lead halide perovskite solar cells. Conversion efficiency over10% has been reported for methylammonium lead halide perovskite solar cell fabricated on plastic substrates.

So far, two processes have been developed to fabricate planar perovskite solar cells. The first process is called one-step process where metal halide is mixed with methylammonium iodide and the as-synthesized methylammonium lead halide perovskite is spin-coated on substrates. The other process is called two-step process where metal halide is spin-coated on substrates and methylammonium lead halide perovskite is formed by inserting the substrates into methylammonium iodide solution. In one-step process, two metal halides, lead iodide (PbI_2) and lead chloride ($PbCl_2$), have been commonly used to synthesize methylammonium lead halide perovskites which are denoted as $MAPbI_3$ and $MAPb(I,Cl)_3$, respectively, with $MAPb(I,Cl)_3$ solar cells leading the performance due to its long diffusion length of carriers. Nevertheless, it is extremely difficult to control the morphology of perovskite thin films because it is significantly affected by the environment of one-step process. In two-step process, the morphology of perovskite thin film is very uniform. However, PbI_2 has been exclusively used because the solubility of $PbCl_2$ is extremely low. Therefore, the advantages associated with Cl incorporation cannot be taken.

3.1 EXPERIMENTAL PROCEDURES

3.1.1 Synthesis of CH_3NH_3I (MAI) and CH_3NH_3Cl (MACl)

MAI and MACl were synthesized according to a reported procedure [88]. MAI was synthesized by reacting 30 mL of methylamine (40 % in methanol, TCI) and 32.3 mL of hydroiodic acid (57 wt% in water, Aldrich) in an ice bath for 2 h with stirring. The precipitate was collected through removing the solvents by a rotary evaporator. The as-obtained product was washed three times with diethyl ether, and then recrystallized from a mixed solvent of diethyl ether and ethanol. After filtration, the final MAI was collected and dried at 60 °C in a vacuum oven for 24 h. MACl was synthesized by reacting 30 mL of methylamine (40 % in methanol, TCI) and 20.4 mL of hydrochloric acid (37 wt% in water, Aldrich) in an ice bath for 2 h with stirring. The precipitation and collection of MACl was carried out using as same procedures as used for MAI.

3.1.2 Fabrication of $MAPbI_3$ Solar Cells

Planar perovskite solar cells were fabricated in air with a structure of FTO/TiO_2/perovskite/spiro-MeOTAD/Au. A modified one-step process capable of incorporating Cl is used to grow the perovskite thin films [89]. The experimental procedures for this process are briefly shown in Fig. 3.2. First, MAI (159mg), PbI2(461mg), DMSO(78mg), and DMF(600mg) were mixed at room temperature and stirred for 1h. The completely dissolved solution was spin-coated on the TiO2 layer at 4000 rpm for 30 s. 8 s after the start of the rotation, 0.5 ml of diethyl ether was quickly dropped on the rotating substrate in 1 sec before the surface changed to be turbid caused by rapid vaporization of DMF. The transparent film was heated at 100°C on hotplate in air for 10 min to obtain a dense $MAPbI_3$ film. These samples were denoted as $MAPbI_3$. To deposit Cl-doped MAPbI3 film, 8mg of MACl was added to the precursor solution. These samples were named as $MAPb(I,Cl)_3$. A layer of electron blocking material based on spiro-OMeTAD (80 mg spiro-OMeTAD, 29 μL tBP and 18 μL Li-TFSI solution (520 mg Li-TFSI in 1 mL acetonitrile) all dissolved in 1 mL chlorobenzene) was deposited on perovskite thin film by spin-coating at 4000 RPM for 30 s. Please note all the processes mentioned above were carried out in air. Finally, a gold layer with a thickness of 100 nm was deposited by electron beam evaporation. A mask was used during the gold deposition to define the active area of perovskite solar cells. The active area of each cell was 4 mm^2.

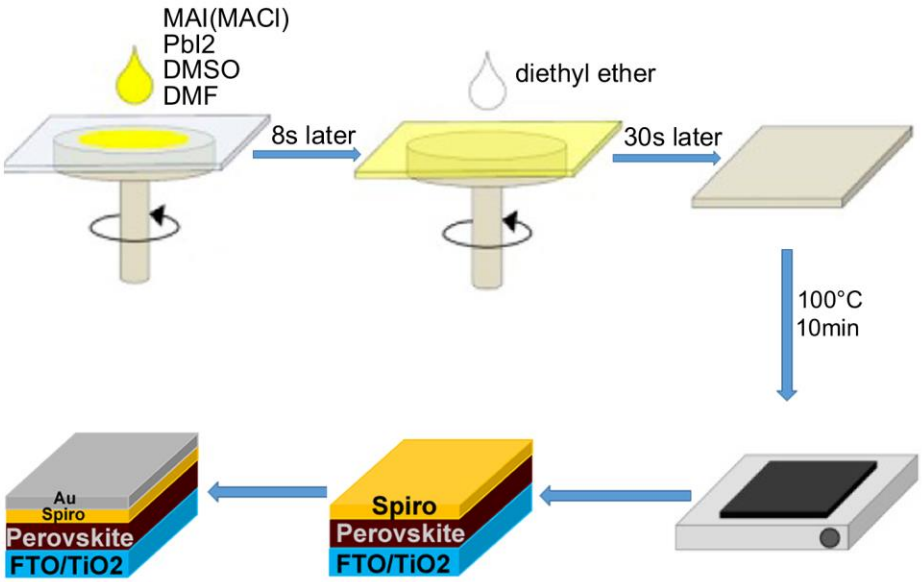

Figure 3.1 Schematic growth process for perovskite thin films using mixed halide sources and method adopted from [89].

3.1.3 Characterization

A UV-visible spectrometer (Agilent 8453) was used to obtain the transmittance (T) of CZTS and MAPbI3 thin films. SEM surface and cross section images of CZTS and $MAPbI_3$ samples were taken from a scanning electron microscope (Philips XL30-FEG). An electron beam with high energy (10 keV~15 keV) was used on the CZTS samples and $MAPbI_3$ thin films. The compositions of the films were analyzed by an energy-dispersive X-ray (EDX) spectroscope (eumex Instrumentebau GmbH SphinX 130), which attached to the SEM system. The energy of the electron beam was raised to 30keV when recording EDX data captured by a Si(Li) detector. X-ray diffraction (XRD) spectra were taken from an XRD system (PANalytical X'Pert Pro MRD) equipped with a CuK$_{\alpha 1}$ X-ray generator. The Raman spectra were recorded by a self-assembled Raman spectrometer with a laser power of 150 mW at 532 nm. The monochromator (Acton SP2500) had a 0.5nm single-pass spectrometer. The photon counter (Princeton Instruments Spec-10) had a N_2-cooled CCD array. Current−voltage responses were measured using an Agilent 4155C semiconductor parameter analyzer under airmass 1.5 global (AM1.5G) 1 sun (100 mW/cm^2.) illumination which was calibrated using a light intensity meter. The voltage was swept from -0.1 V to 1.1 V at a rate of 10 mV/s with a step of 10 mV/step. For the hysteresis investigation, the voltage was swept from either from -0.1 V to 1.1 V (forward bias) or from 1.1 V to -0.1 V (reverse bias) at a rate of 10 mV/s with a step of 10 mV/step. KPFM measurement was carried out using Agilent 5500 AFM with MAC III mode. The conductive AFM tip (Veeco SCM-PIT, k=2.8 N/m, coated with Pt/Ir) was simultaneously excited by mechanical drive at its resonant frequency (75 kHz), and by electrical drive around 10 kHz.

3.2 RESULTS AND ANALYSIS

The content of Cl has been checked by energy-dispersive X-ray spectroscopy (EDS). The EDS spectra of $MAPb(I,Cl)_3$ and $MAPbI_3$ thin films are shown in Fig. 3.2. The weight ratios of Pb, I, and Cl derived from the EDS spectra are summarized in Table 3.1. The weight ratios of Cl in $MAPb(I,Cl)_3$ and $MAPbI_3$ thin films are same. This indicates that the concentration of Cl in $MAPb(I,Cl)_3$ should be lower than the detection limit of the EDS system because no Cl has been intentionally added to the so-called $MAPbI_3$ thin film.

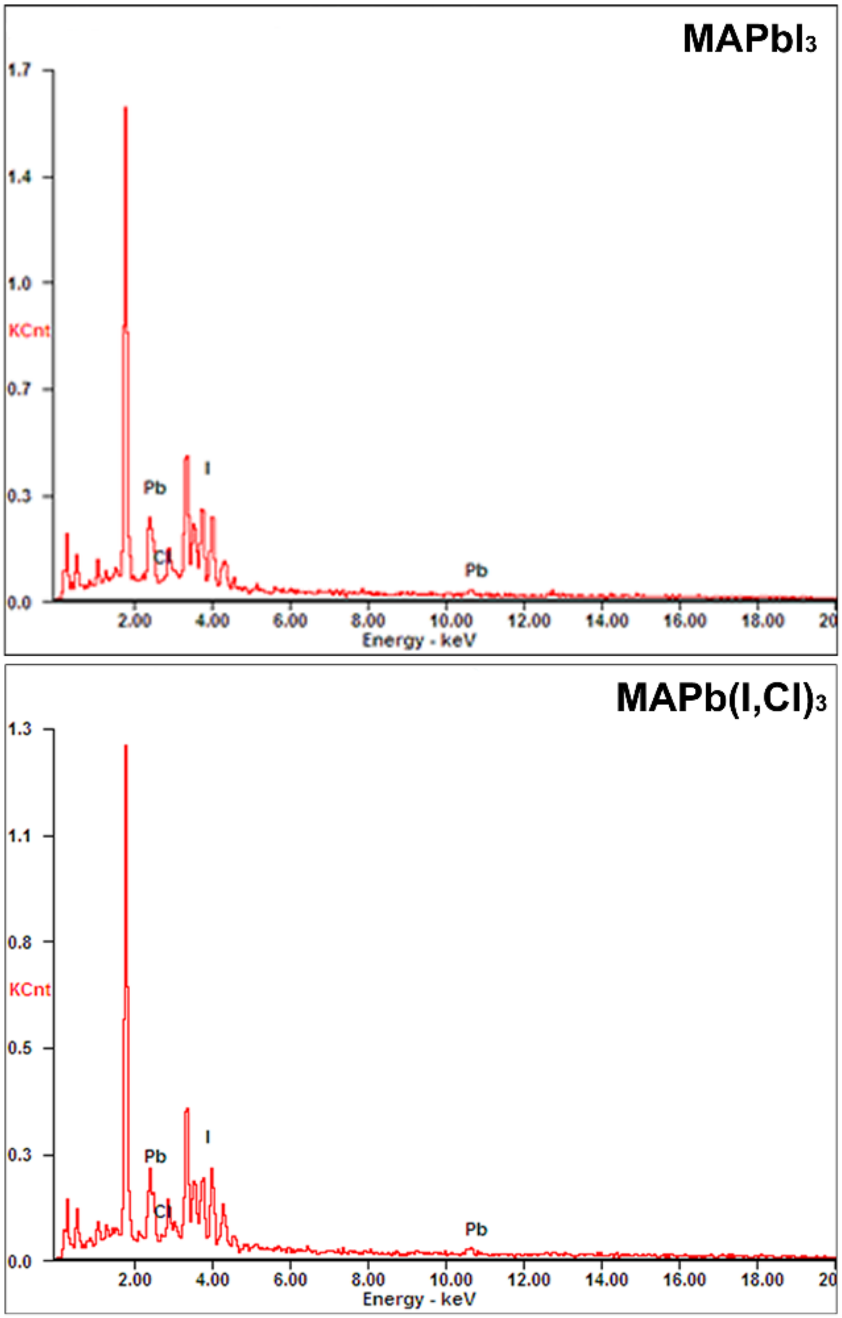

Figure 3.2 EDS spectra of the perovskite thin films.

Table 3.1 Elemental ratios of the perovskite solar cells.

	Pb (wt%)	**I (wt%)**	**Cl (wt%)**
$MAPbI_3$	38.95	60.06	0.99
$MAPb(I,Cl)_3$	38.36	60.65	0.99

The SEM images of the surfaces of $MAPbI_3$ and $MAPb(I,Cl)_3$ thin films are shown in Fig. 3.3. the deposited perovskite thin films are homogeneous and densely packed. This demonstrates the advantage of the modified one-step process for preparing perovskite thin films, comparing to other one-step processes which usually lead to incomplete coverage of substrate [90]. In the case of $MAPb(I,Cl)_3$ thin film that was prepared using mixed halide source, no difference is observed in the morphology, indicating the addition of MACl does not affect the growth of perovskite thin film and the interaction between the substrate and the perovskite thin film.

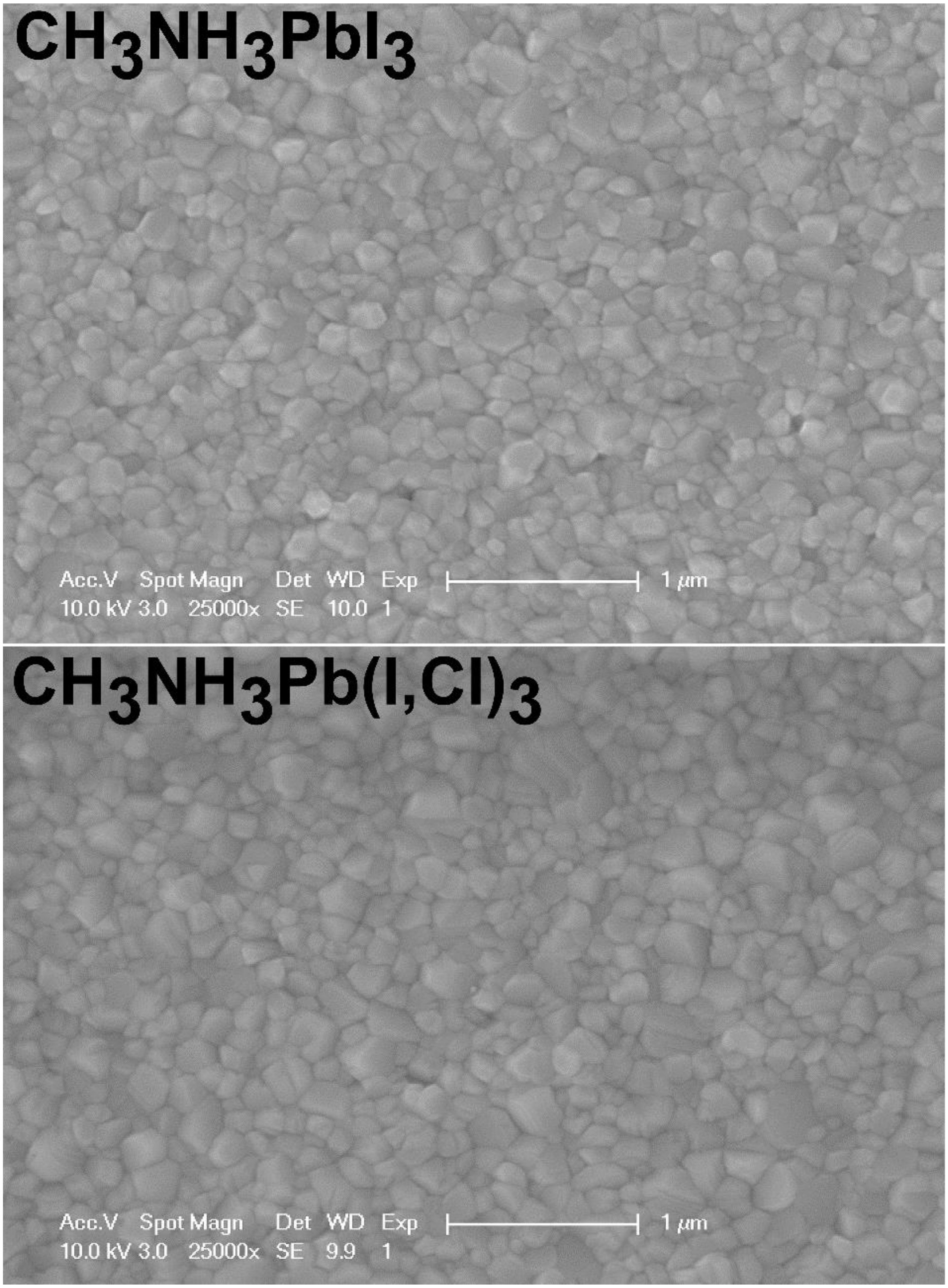

Figure 3.3 Top-view SEM images of $MAPbI_3$ and $MAPb(I,Cl)_3$ thin films.

The typical XRD patterns of the $MAPbI_3$ and $MAPb(I,Cl)_3$ thin films deposited in this work are shown in Fig. 3.4 (a). No obvious difference is observed. The three major peaks at 14.09°, 28.44° and 31.87° can be indexed to the $MAPbI_3$ phase, corresponding to the lattice planes of (110), (220), and (310) [91]. No $MAPbCl_3$ peaks are found in $MAPb(I,Cl)_3$ thin film because of the small quantity of Cl source added. The peak located at 12.06°, which can be ascribed to PbI_2 phase, is observed with both the $MAPbI_3$ and $MAPb(I,Cl)_3$ thin films [89]. It is due to the excess PbI_2 in perovskite precursor solution, which is reported to boost the performance of perovskite solar cells [92]. The magnified XRD patterns peaking at 14.09° from lattice plane (110) of both samples are shown in Fig. 3.4 (b). Full width at half maximum (FWHM) of this peak is used to calculate the crystal size of perovskite thin films according to Scherrer equation. The average crystal sizes of $MAPbI_3$ and $MAPb(I,Cl)_3$ thin films are 102 nm and 106 nm, respectively. This confirms what has been observed in SEM images of $MAPbI_3$ and $MAPb(I,Cl)_3$ thin films. The effects caused by difference in morphologies crystal structures can be excluded. The results obtained from other characterization methods would be more reliable.

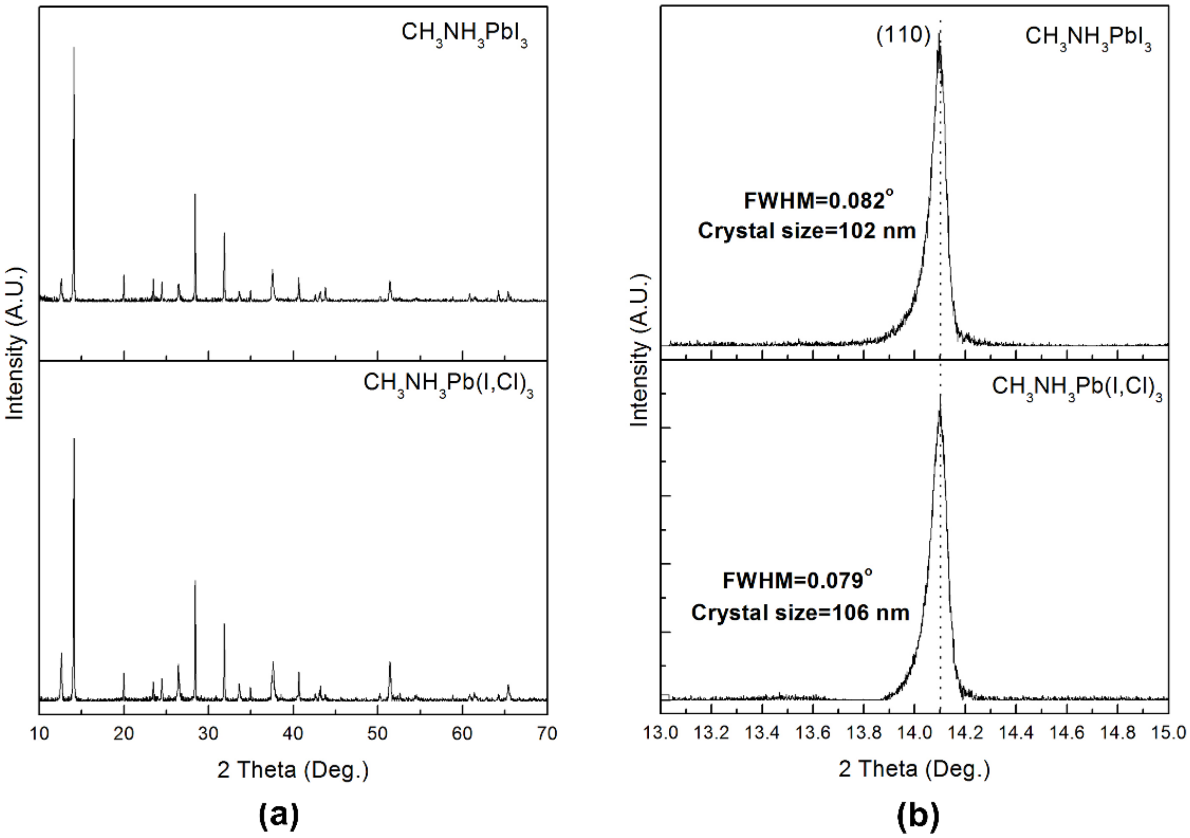

Figure 3.4 XRD patterns of $MAPbI_3$ and $MAPb(I,Cl)_3$ solar cells: (a) full range, (b) major peak at (110) to calculate the crystal size.

The typical *I-V* characteristics of $MAPbI_3$ and $MAPb(I,Cl)_3$ solar cells are shown in Fig. 3.5. A general trend of enhancement of efficiency in $MAPb(I,Cl)_3$ solar cells can be observed from the comparison with $MAPbI_3$ solar cells as shown in the inset of Fig. 3.5. Not only has the enhancement in efficiency been observed but also in short-circuit current density (J_{SC}), fill factor (*FF*) (not shown), and open circuit voltage (V_{OC}) (not shown). The best $MAPbI_3$ solar cell produced a J_{SC} of 22.47 mA/cm^2, a V_{OC} of 1.04 V and a *FF* of 65.90%, while the most efficient $MAPb(I,Cl)_3$ solar cell had a J_{SC} of 24.10 mA/cm^2, a V_{OC} of 1.08 V and a *FF* of 71.50%. As a result, the efficiency of MAPb(I,Cl)$_3$ solar cell was significantly improved from 15.39% to 18.60%. The reasons of the enhancement of photovoltaic parameters were investigated and discussed below. The best I-V parameters are summarized in Table 3.2.

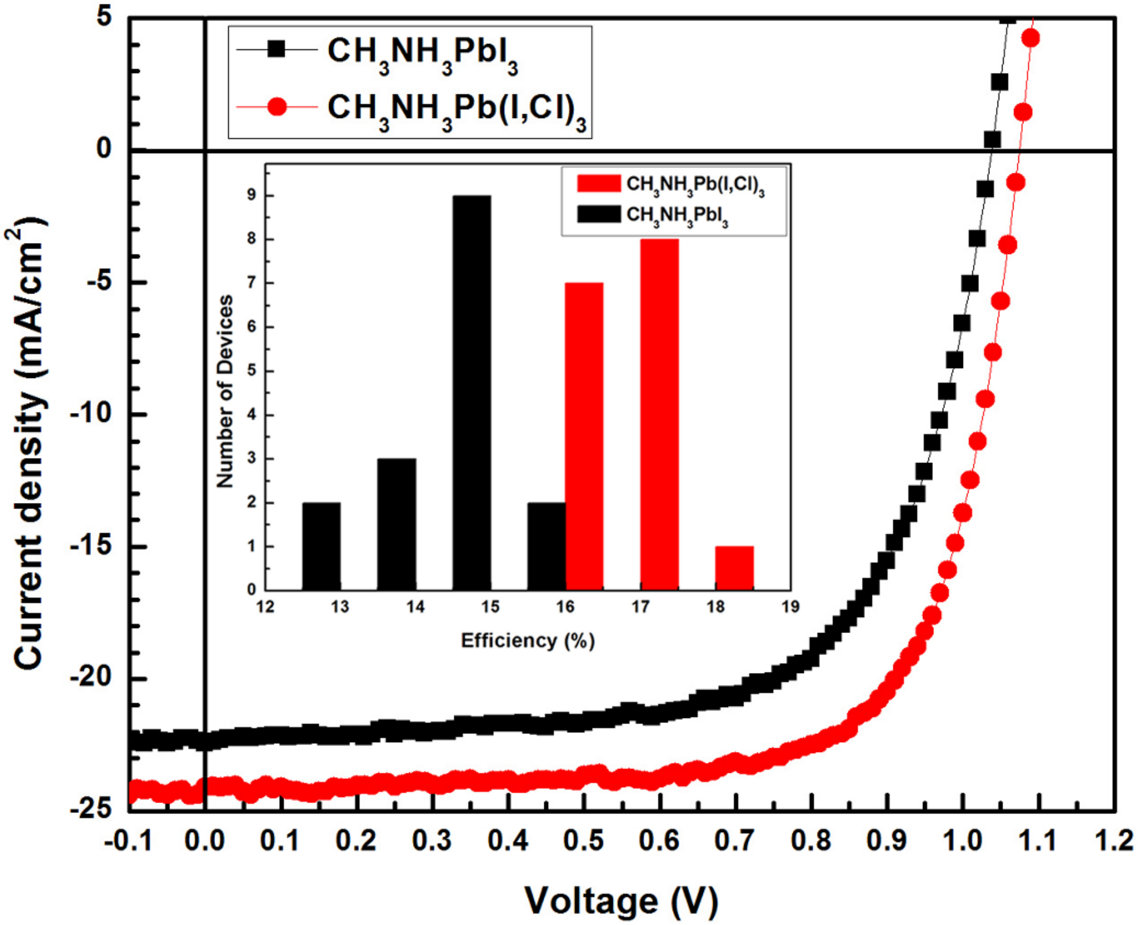

Figure 3.5 *I-V* curves and parameters of MAPbI$_3$ and MAPb(I,Cl)$_3$ solar cells (the inset is the efficiency distributions of 16 devices for each sample) measured at around 25°Cunder simulated sunlight of 100 mW/cm^2 (AM1.5G).

Table 3.2 *I-V* parameters of the best perovskite solar cells.

	V_{OC} (V)	J_{SC}(mA/cm^2)	FF(%)	η(%)
$MAPbI_3$	1.04	22.47	65.90	15.39
$MAPb(I,Cl)_3$	1.08	24.10	71.50	18.60

To investigate the mechanisms behind the significant improvement in the performance of $MAPb(I,Cl)_3$ solar cells, the surface potential (SP) distributions of both materials were mapped using KPFM [42]. As shown in Fig. 3.6, the dark regions around grain boundaries indicate the band bending that favour electron accumulation. KPFM measurement of $MAPbI_3$ shows a uniform distribution of SP among grain bodies and grain boundaries indicating a narrower and smaller band bending, while KPFM measurement of $MAPb(I,Cl)_3$ shows a large variation of SP among grain bodies and grain boundaries indicating a deeper and wider band bending at the grain boundaries .

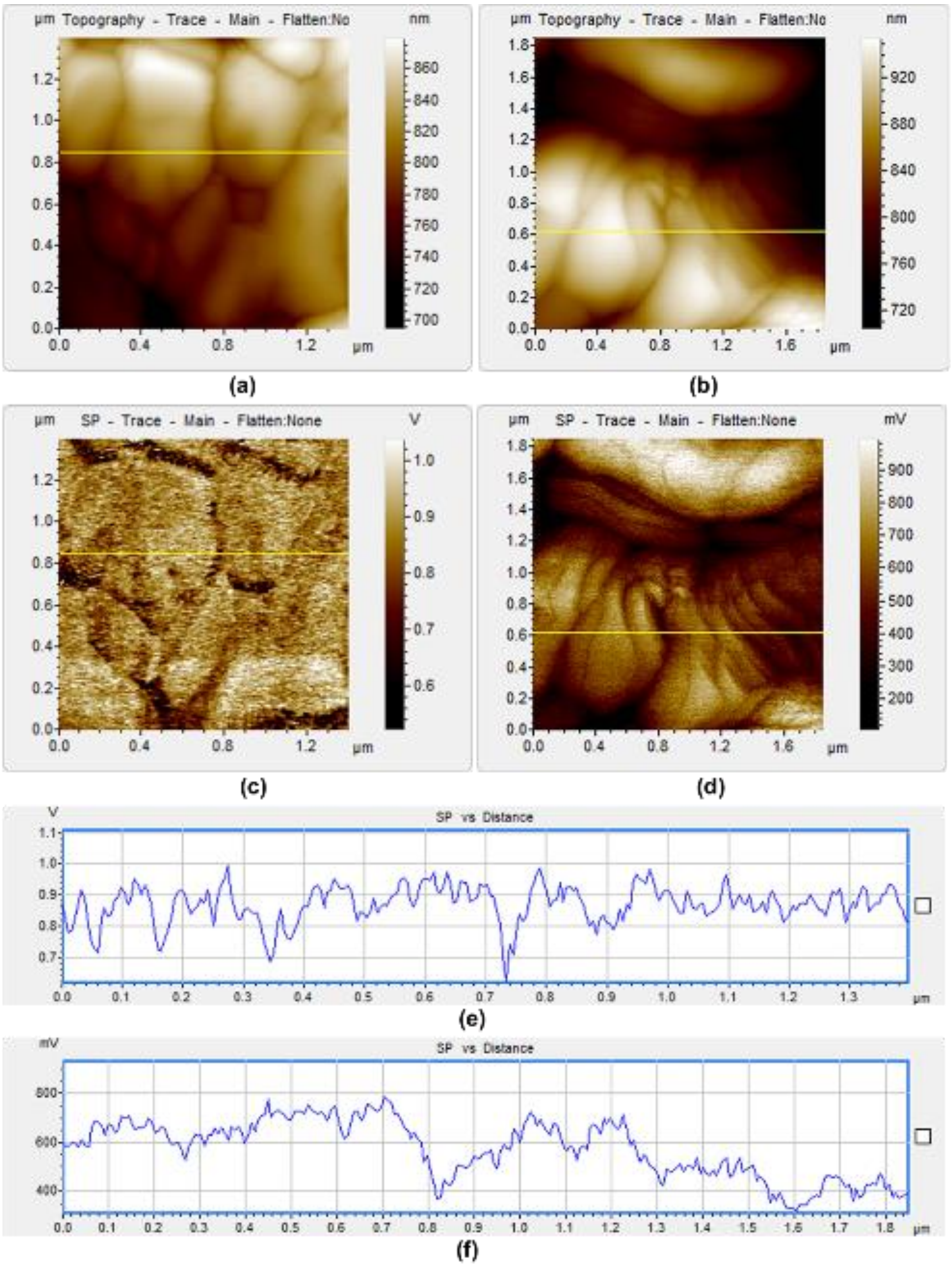

Figure 3.6 Topography AFM images (a and b), SP (c and d), and profiles of SP (e and f) of $MAPbI_3$ (a, c, and e) and $MAPb(I,Cl)_3$ (b, d, and f) thin films on ITO.

$MAPbI_3$ was found to be a p-type material [93], thus a single p-n heterojunction should be formed at the cathode side of the device (Fig. 3.7 (a)). For this single p-n heterojunction, an electron blocking layer is needed on the anode side. The charge collection efficiency is higher on the junction side (cathode) but lower on the anode side because only diffusion contributes to the charger transport on the anode side. The observation of wider and deeper band bending at the grain boundaries of $MAPb(I,Cl)_3$ from KPFM measurements indicates that electron accumulation is enhanced at the grain boundaries thus bring the Fermi level closer to the center band to make $MAPb(I,Cl)_3$ less p-type. Such Fermi level shift results in a p-i-n heterojunction in the device (Fig. 3.7 (b)), first speculated in mesoporous $MAPb(I,Cl)_3$ solar cells [94] and later observed in planar $MAPb(I,Cl)_3$ solar cells by electron beam-induced current study [95]. The p-i-n heterojunction facilitates the charge collection on both sides because both drift and diffusion contribute to the charge transport. In addition, the junction on the anode side provides a blocking barrier to prevent electrons reaching the anode, thus to reduce recombination loss.

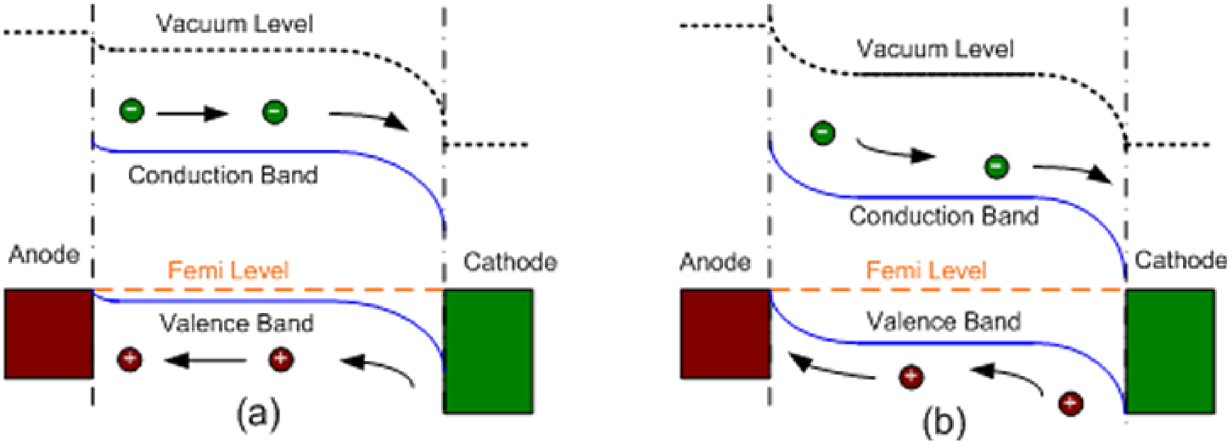

Figure 3.7 Band alignment of devices for (a) $MAPbI_3$ and (b)$MAPb(I,Cl)_3$.

KPFM was employed to study the GBs of $MAPbI_3$ and $MAPb(I,Cl)_3$ thin films. Fig. 3.8 shows the surface morphology images and the surface potential (SP) images of $MAPbI_3$ and $MAPb(I,Cl)_3$ thin films. The topography images were used to identify the location of GBs and the SP images were used to derive the difference of work functions of the GBs and the bulk crystals. In KPFM measurement, two separate oscillation frequencies are applied to AFM cantilever to detect the topography and the SP simultaneously, cross-talk of signals from topography and SP cannot be completely eliminated. The line profiles were then used to check the existence of cross-talk. The line profiles in Fig. 3.8 indicate the SP does not follow the topography. By checking the line profiles in Fig. 3.8 (a), it was revealed most of the GBs (G1, G2, G3, G6, G7) in $MAPbI_3$ thin film demonstrated a higher potential than the center of the grain surface. Conversely, it was shown in Fig. 3.8 (b), most of the GBs (G1, G2, G3, G5, G8, G9) in $MAPb(I,Cl)_3$ demonstrated a lower potential than the center of the grain surface. This indicates that upward band bending around the GB dominates in the $MAPbI_3$ thin film and downward band bending around the GB dominates in the $MAPb(I,Cl)_3$ thin film. Upward band bending around the GB in the MAPbI3 thin film has been reported [95]. To our knowledge, this is the first time that downward band bending around the GB in the $MAPb(I,Cl)_3$ thin film is reported.

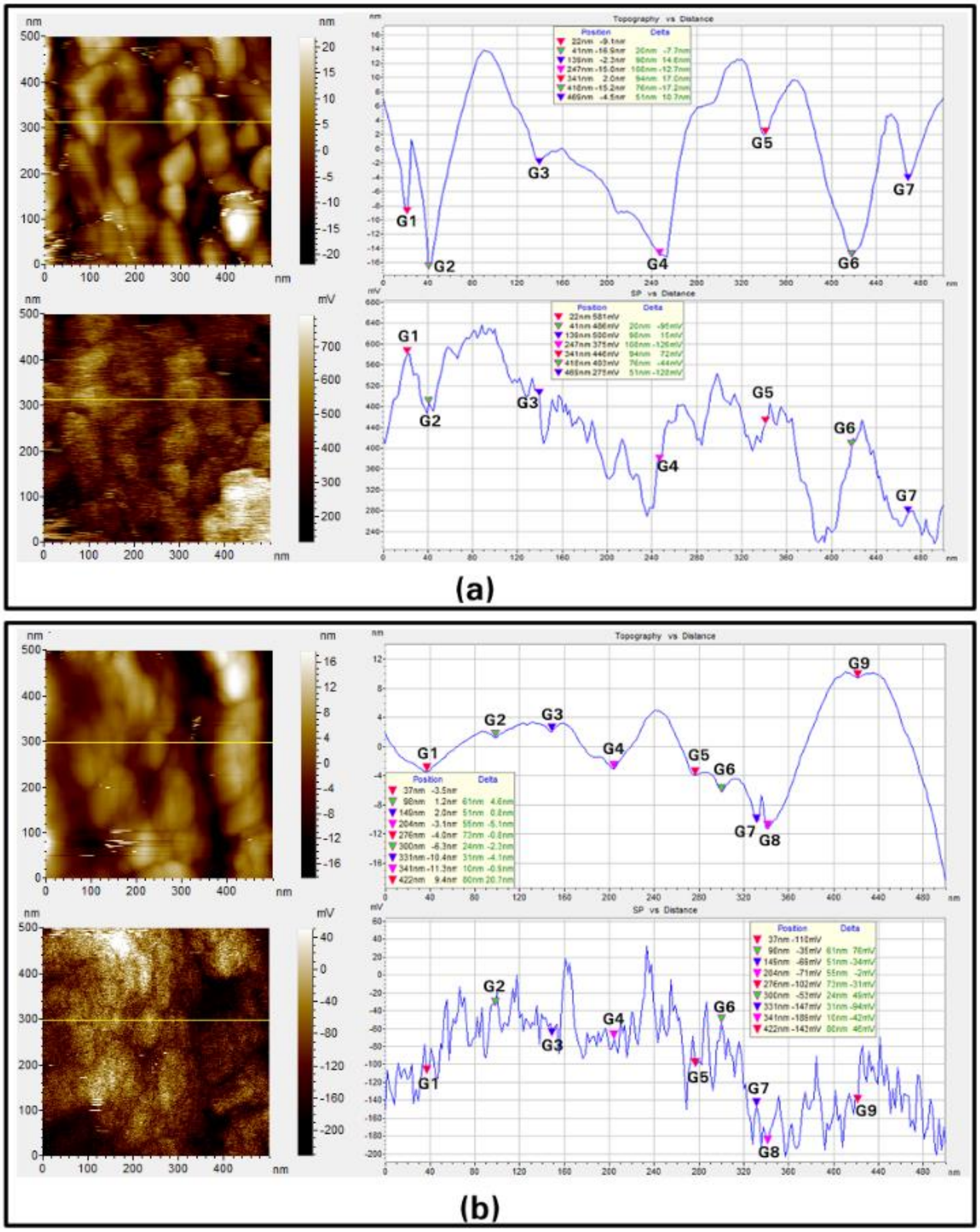

Figure 3.8 AFM images, KPFM images, and the profiles along the lines in (a) $MAPbI_3$ and (b) $MAPb(I,Cl)_3$ thin films.

The band diagrams around the GB in $MAPbI_3$ and $MAPb(I,Cl)_3$ thin films are plotted in Fig. 3.9 with an assumption that the GB and the grain have same bandgap values. It has been reported $MAPbI_3$ thin film shows p-type conductivity [96]. The incorporation of a small amount of Cl atoms into $MAPbI_3$ thin film does not likely reverse the conductivity type because Cl and I belong to the same halogen group. Therefore, the transport behavior of electrons (minority carriers) in $MAPbI_3$ and $MAPb(I,Cl)_3$ thin films significantly affects the performance of perovskite solar cells. The potential barrier due to the upward band bending at GB in $MAPbI_3$ thin film repels electrons and attracts holes. The electrons will have to be transported to the cathode through the grain bulk where majority holes (majority carriers) have a high concentration, resulting in higher recombination rate. On the contrary, the potential barrier due to the downward band bending at GB in $MAPb(I,Cl)_3$ thin film repels holes and attracts electrons. The electrons will be transported to the cathode through both the grain bulk and GB where majority holes (majority carriers) are depleted, resulting in a higher collection area and a lower recombination rate. This will again benefit the diffusion length and the performance of solar cells such as V_{OC} and FF. Considering the low concentration of Cl allowed to be incorporated into $MAPbI_3$ thin film, the properties of bulk grains should not change significantly. As observed in the KPFM measurement, the properties of the GBs in $MAPbI_3$ thin film have been significantly affected, which could be attributed to the accumulation of Cl atoms in the GBs as sodium atoms do in CIGS thin films[97]. This would be verified by high definition element mapping technique such as TEM, which is ongoing in our research.

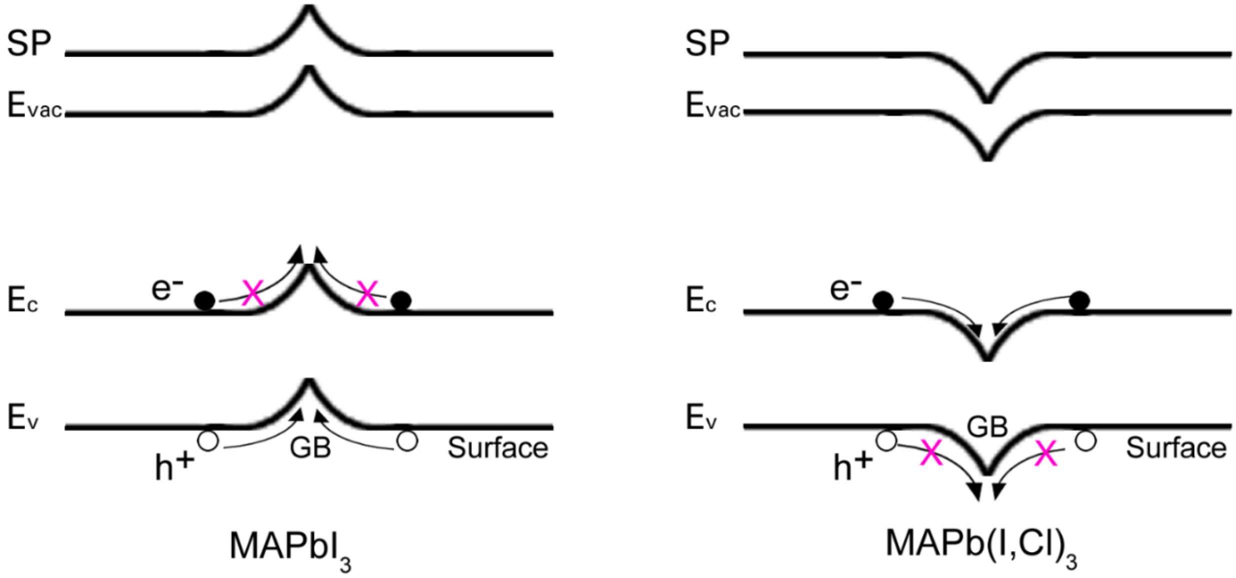

Figure 3.9 Band diagrams around the GB in $MAPbI_3$ and $MAPb(I,Cl)_3$ thin films.

The measurement of electron lifetime can be applied to quantify the extent of electron recombination in perovskite solar cells [33]. The dependence of electron lifetime on the V_{OC} for planar perovskite solar cells fabricated with single and mixed halide source is shown in Fig. 3.10. It clearly demonstrates that the electron lifetime of the $MAPb(I,Cl)_3$ solar cells is longer than that of the $MAPbI_3$ solar cell. This suggests that the electrons in $MAPb(I,Cl)_3$ thin film can survive longer and demonstrate a longer diffusion length as reported in literatures [98, 99].

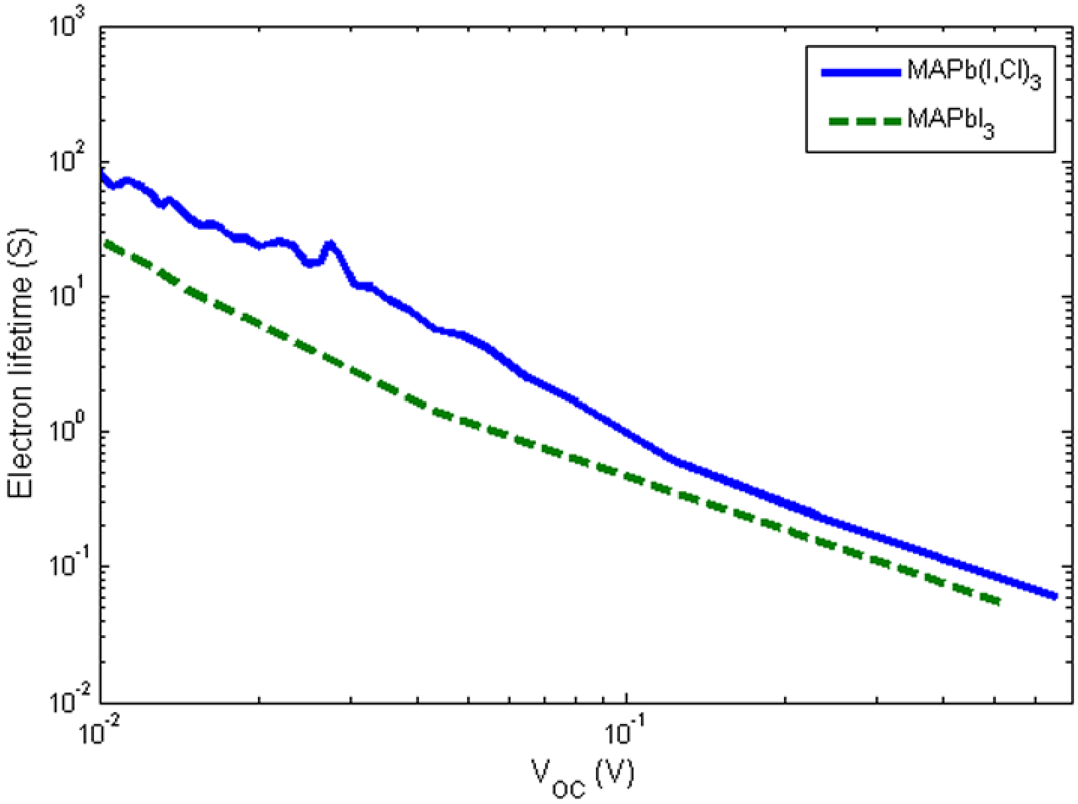

Figure 3.10 The electron lifetime as a function of $V_{OC.}$

The longer electron lifetime in $MAPb(I,Cl)_3$ solar cells, indicating a reduced recombination, can also be explained by the KPFM observation. The lack of SP difference at grain boundaries and grain bulk of $MAPbI_3$ may render free carriers generated during illumination to easily recombine, thus shorten carrier lifetime. On the contrary, the large variation of SP between grain boundary and grain bulk means abundant potential wells are formed at the grain boundaries to accommodate electrons, which physically separate electrons from holes preventing the carrier recombination. In addition, the locally formed junctions between the grain bodies and grain boundaries enhance the dissociation of excitons and further suppress recombination. As a result, carrier life time is greatly improved in $MAPb(I,Cl)_3$ solar cells.

The AS technique has been well established to investigate the defect levels of thin film solar cells such as CIGS and CdTe [100-102]. It has been rarely applied to perovskite solar cells. So far, only two groups have addressed the defect density of $MAPbI_3$ solar cells using AS technique. In 2014, Dalal et al. found two defect levels in $MAPbI_3$ solar cell. One is 0.24 eV and the other is 0.65 eV above the valence band with a peak density value of $3\times10^{16}/(cm^3\cdot eV)$ [103]. In the same year, Yang et al. revealed a deep defect state of 0.17 eV above the valence band with a peak density value of $2\times10^{17}/(cm^3\cdot eV)$ [104]. The cause of the difference in defect levels and densities is not clear. They might be attributed to the difference in $MAPbI_3$ thin films because the deposition method for $MAPbI_3$ thin film used by one group is different from the method used by the other group. To investigate the mechanisms behind the significant improvement in the $MAPb(I,Cl)_3$ solar cell, we applied the AS method to $MAPbI_3$ and $MAPb(I,Cl)_3$ solar cells fabricated by the exactly same procedures. As discussed earlier, the resultant $MAPbI_3$ and $MAPb(I,Cl)_3$ thin films were highly similar in morphology and crystal structure. The results obtained from AS method, as shown in Fig. 3.11, should be more reliable to reveal the origin of the significant performance improvement observed in $MAPb(I,Cl)_3$ solar cells. The defect levels of $MAPbI_3$ and $MAPb(I,Cl)_3$ solar cells derived from Arrhenius plot, as shown in Fig. 3.11 (a), are 0.214 eV and 0.208 eV, respectively. The difference of 6 meV could come from the measurement error. The energy distributions of the defects are shown in Fig. 3.11 (b). For $MAPbI_3$ solar cell, the defect density peaks at $7.2\times10^{17}/(cm^3\cdot eV)$, while the peak defect density of $MAPb(I,Cl)_3$ solar cell is reduced to $3.8\times10^{17}/(cm^3\cdot eV)$. The spans of defect states can be fitted as a Gaussian distribution (the solid lines). The integrated defect density of $MAPbI_3$ solar cell is 4.68×10^{16} cm^{-3}

and that of $MAPb(I,Cl)_3$ solar cell is reduced to 2.34×10^{16} cm^{-3}. A reduced defect density has been experimentally observed in $MAPb(I,Cl)_3$ solar cells. The result is in good agreement with what has been proposed in the electron lifetime measurement: Cl helps to passivate the defects in $MAPb(I,Cl)_3$ solar cells, leading to a lower defect density and higher electron lifetime. Thus, OCVD and AS jointly demonstrate that Cl plays an extremely important role in suppressing the defect in perovskite devices. Further investigation is required and under way to understand the origin of this defect and why Cl is able to suppress the formation of defect when depositing perovskite thin films.

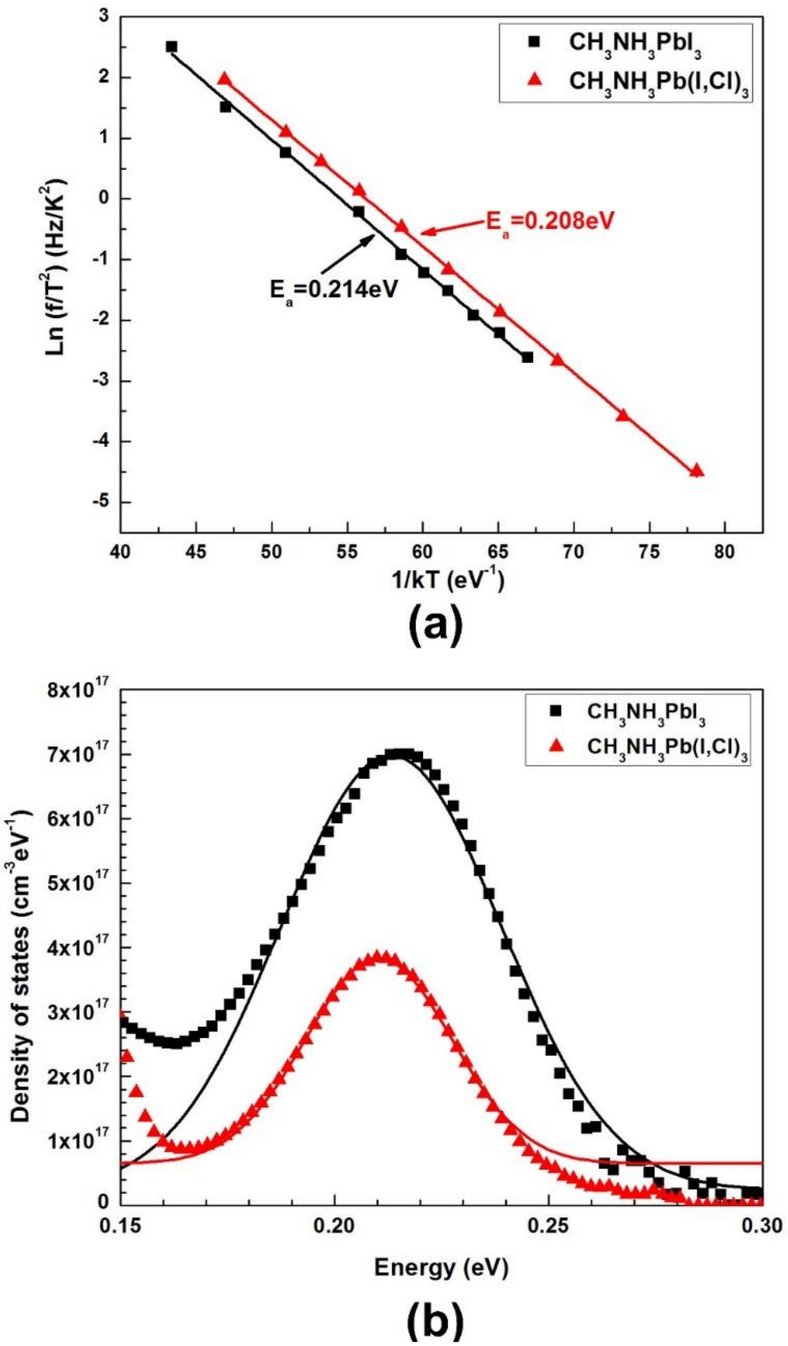

Figure 3.11 Admittance spectroscopy of $MAPbI_3$ and $MAPb(I,Cl)_3$ solar cells: (a) Arrhenius plot of the transition frequencies to derive the defect energy levels, (b) the distributions of the density of the defects.

4.0 CHLORINE-ASSISTED RECOVERY OF PERFORMANCE LOSS IN MAPBI$_3$ PEROVSKITE SOLAR CELL MADE FROM LOW PURITY PBI$_2$

High purity (9~11N) silicon has been required to manufacture integrated circuits and was traditionally used to fabricate photovoltaic (PV) devices [105, 106]. Due to the nature of low density of sunlight, large area of PV devices is needed to generate applicable electricity [107]. The high cost and shortage of high purity silicon, however, limit the deployment of PV devices. Comparatively low purity silicon such as solar-grade (5~6N) silicon has been developed and currently widely used in the PV industry [108]. Nevertheless, the impurities in low purity silicon are known to reduce minority carrier diffusion length in silicon-based PV devices [109, 110], leading to degraded solar-to-electricity conversion efficiency [111-113]. Several methods, such as external and internal gettering, have been approved to be capable of improving the quality of low purity silicon, especially for minority carrier lifetime [105, 114, 115].

Organic-inorganic hybrid perovskite solar cell has recently become an intensively explored topic in PV field because of its high performance and potentially low manufacturing cost. Significant efforts have been focused on developing high quality perovskite thin films and improving the stability of perovskite solar cells. To this date, lead sources such PbI_2 and $PbCl_2$ with a purity of 99.999% (5N), have been widely in fabricating highly efficient perovskite solar cells [116], which is the major concern regarding the mass deployment of perovskite solar cells, not to mention the high cost and the adverse impact on the environment associated with the purifying process [117]. Recently, the purity of raw materials, which is known to significantly affect the performance of both organic [118] and inorganic [119] solar cells, as well as silicon-based solar cells, has been investigated for perovskite solar cells [120]. It was found that perovskite solar cells using highly pure (5N) PbI_2 showed an efficiency of 16.4%, which was higher than that of perovskite solar cells with low purity (2N) PbI_2 by 30–40%, indicating highly pure PbI_2 is indispensable for highly efficient perovskite solar cells.

4.1 EXPERIMENTAL PROCEDURES

4.1.1 Fabrication of $MAPbI_3$ Solar Cells using PbI_2 with different purtities

Planar perovskite solar cells were fabricated in air with a structure of FTO/TiO_2/perovskite/spiro-MeOTAD/Au. A modified one-step process capable of incorporating Cl is used to grow the perovskite thin films [89]. PbI_2 with different purities (99% and 99.999%) were purchased from Sigma Aldrich and were used without further processing. The experimental procedures described in 3.1.2 were employed to deposit MAPbI3 thin films and fabricate $MAPbI_3$ solar cells.

4.2 RESULTS AND ANALYSIS

In this work, the effects of Cl on perovskite solar cells fabricated using high and low purity PbI_2 were investigated. The averaged I–V curves of these devices fabricated using the same experimental procedures are shown in Fig. 4.1. As shown in the inserted table in Fig. 4.1, the averaged performance parameters, including V_{OC}, J_{SC}, FF, and efficiency (Eff.), are significantly affected by the purity of PbI_2. The perovskite solar cell with high purity PbI_2 exhibited a high efficiency of 16.39 % with a J_{SC} of 23.46 mA/cm^2, V_{OC} of 1.07 V, and FF of 65.31%, while that with low purity PbI_2 had a comparatively low efficiency of 14.16% with a J_{SC} of 21.94 mA/cm^2, V_{OC} of 1.04 V, and FF of 62.07 %. This agrees well with what has been reported in literature [120]. Excitingly, the efficiency of perovskite solar cell with low purity PbI_2 was significantly boosted to 16.58% after a small amount of Cl source was added. The lost efficiency in low purity perovskite solar cells is fully recovered when Cl is added. The resulted efficiency is even slightly higher than that obtained from high purity perovskite solar cells. This indicates that, besides the costly way of increasing the purity of raw materials, Cl doping could provide a cost-effective way to further improve the performance of perovskite solar cells.

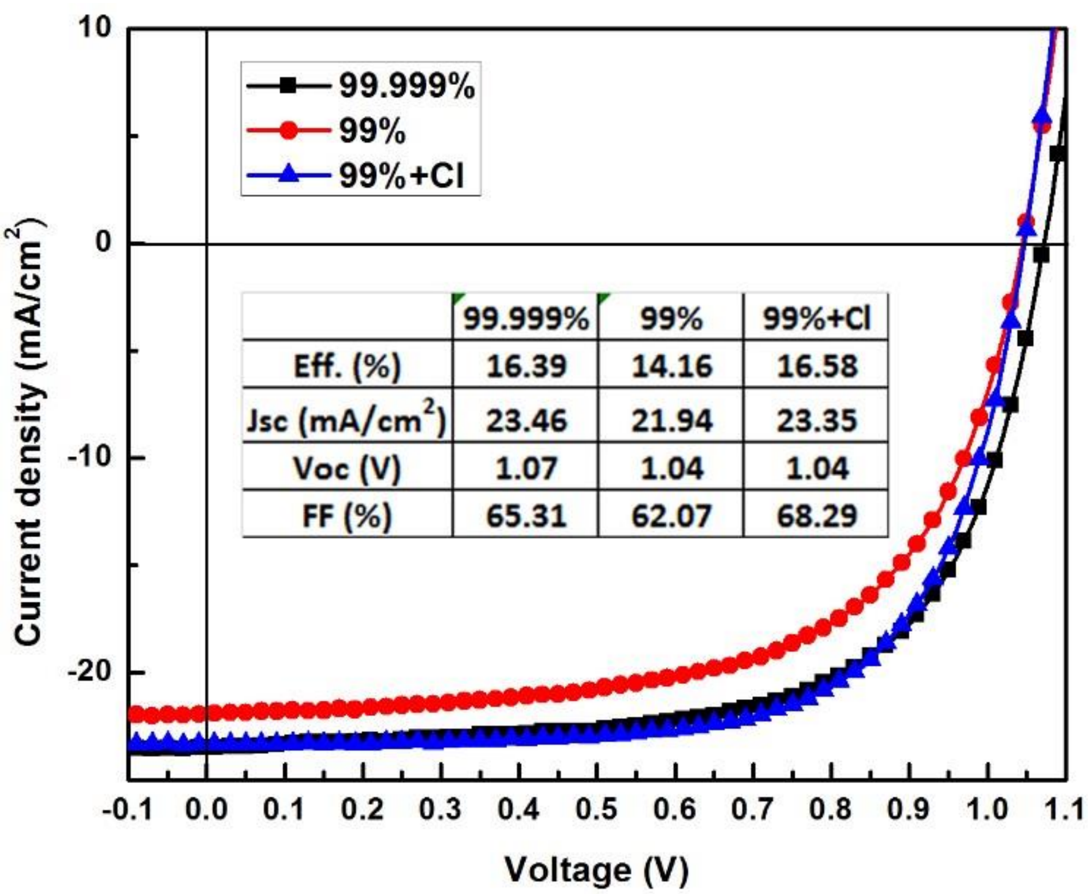

	99.999%	99%	99%+Cl
Eff. (%)	16.39	14.16	16.58
Jsc (mA/cm^2)	23.46	21.94	23.35
Voc (V)	1.07	1.04	1.04
FF (%)	65.31	62.07	68.29

Figure 4.1 Averaged I-V curves and parameters of perovskite solar cells (10 devices for each sample).

To investigate the mechanisms behind the significantly improved performance of low purity perovskite solar cells brought by Cl, the morphology of the perovskite thin films was checked by SEM. The SEM images are shown in Fig. 4.2. The average crystal size of the high purity thin film is slightly smaller compared to the low purity thin film. This is contrary to what has been reported by J. Chang et al. who found that the average crystal size of the high purity perovskite thin film was 20 nm larger compared to the low purity thin film [120]. The contradiction in this aspect could be caused by the different solvents used for perovskite precursors, which are known to significantly affect the morphology of perovskite thin films. No obvious difference can be observed once Cl is added.

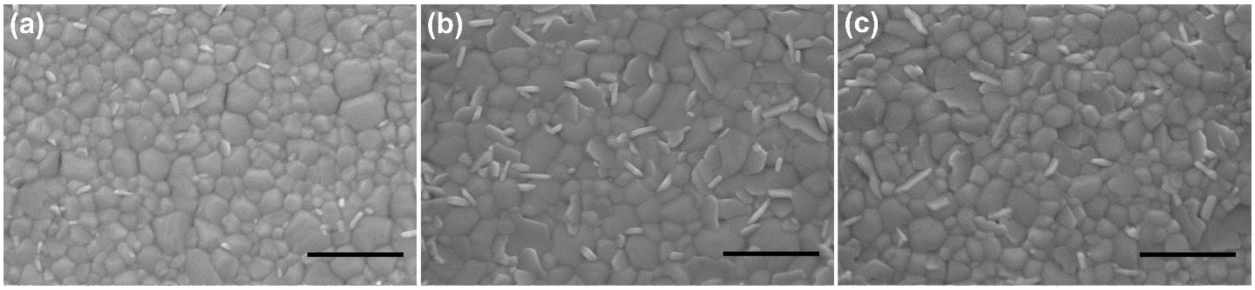

Figure 4.2 SEM images of perovskite thin films deposited utilizing different purities of PbI_2. (a) 99.999%, (b) 99%, and (c) 99%+Cl. (The scale bar is 1μm).

This result is consistent with the XRD results (Fig. 4.3 (a-b)). Further investigation of the transmittance spectra (Fig. 4.3 (c)) and optical bandgap (Fig. 4.3 (d)) of these films is not able to reveal the mechanisms behind the recovery of performance loss by Cl because no distinct difference can be observed. Most of the studies regarding the effects of Cl on perovskite solar cells found that the morphology is improved and crystallinity is enhanced, which is caused by the relatively high concentration of Cl source in perovskite precursor solution, even though the amount of Cl in the final perovskite thin film is negligible [121-123]. The concentration of the Cl source used in this work was deliberately controlled to be extremely low so that the addition of Cl would not obviously affect the morphology and structure of perovskite thin films, which is able to exclude the effects of morphology and structure when investigating the mechanisms behind the Cl-assisted recovery of performance loss in low purity $MAPbI_3$ solar cells.

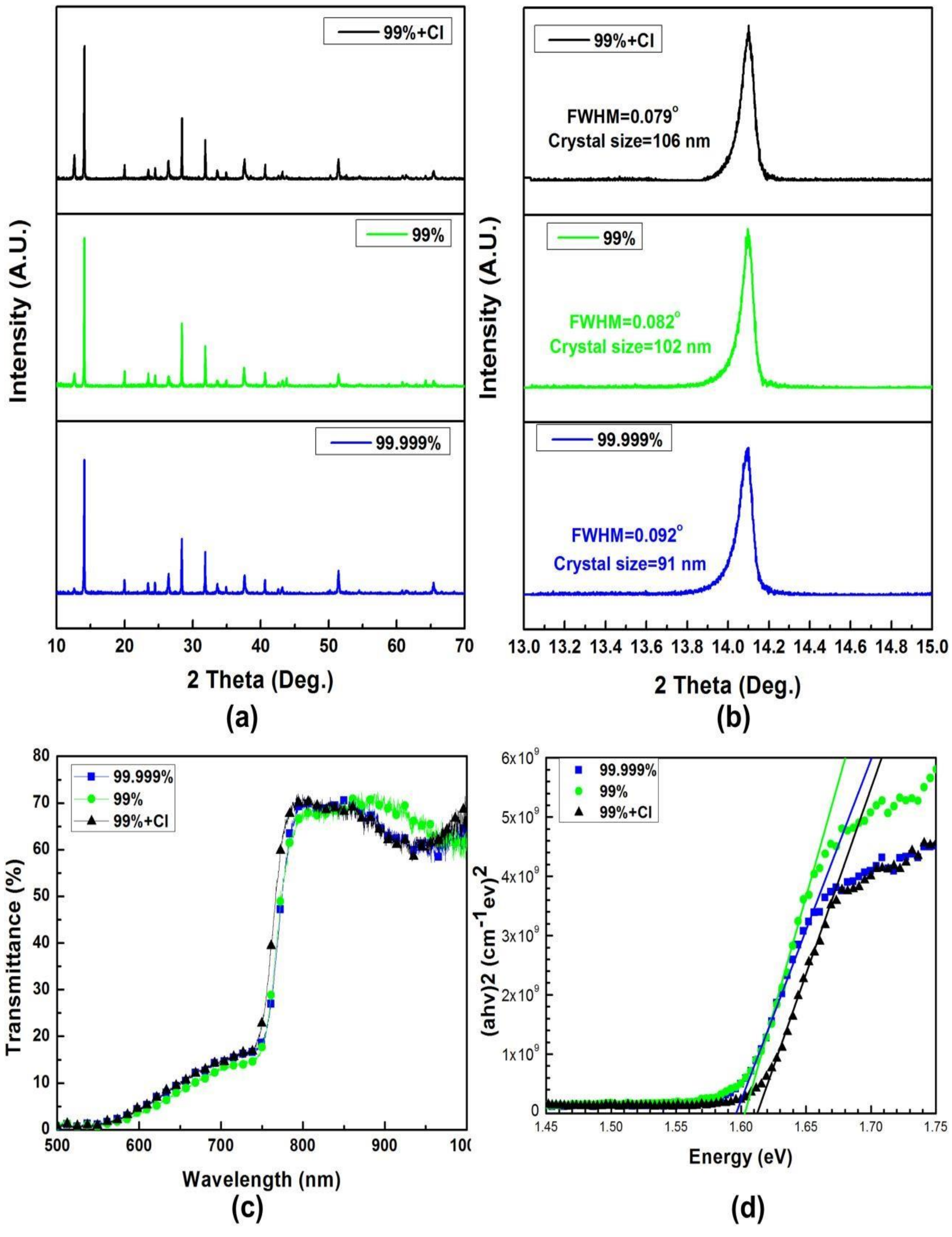

Figure 4.3 (a) XRD patterns, (b) major peak at (110), (c) transmittance, and (d) optical bandgap energies of perovskite thin films utilizing different purities of PbI_2.

The measurement of electron lifetime using OCVD method can be applied to quantify the extent of electron recombination in perovskite solar cells [116]. The dependence of the electron lifetime on the V_{OC} for perovskite solar cells fabricated with different purities of PbI_2 is shown in Fig. 4.4. It clearly demonstrates that the electron lifetime of the low purity perovskite solar cells is the lowest and it is significantly improved once Cl is added.

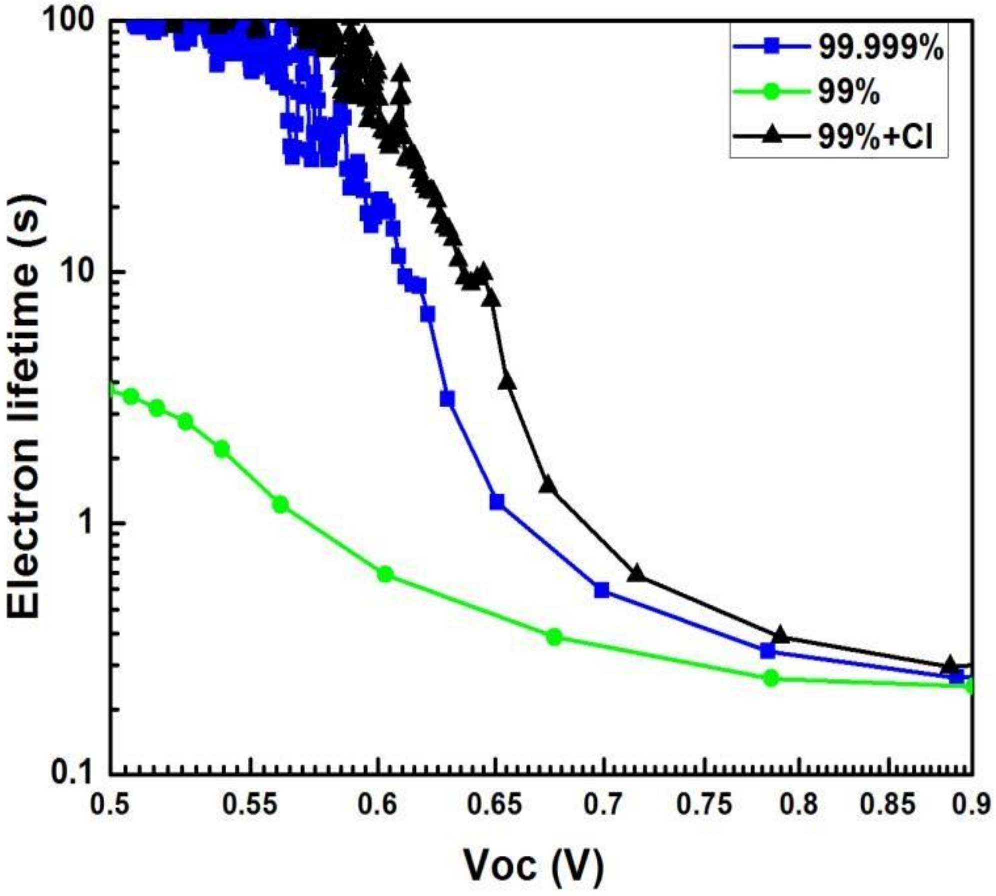

Figure 4.4 The electron lifetime derived from OCVD method as a function of V_{OC}.

It is well known that low purity absorber materials in solar cells usually demonstrate high defect density caused by the high impurity concentration, leading to a decreased carrier lifetime, and therefore reduced conversion efficiency [124-127]. Admittance spectroscopy (AS) is widely applied to derive the distribution of defect density and the energy levels of the defects in the bandgap by measuring the capacitance of the solar cell at different temperatures [103, 128, 129]. Fig. 4.5 (a) shows the capacitance spectra of perovskite solar cell fabricated using low purity PbI_2 with Cl (99%+Cl) obtained at different temperatures (T=150 K to 296 K) in the dark with the frequency ranging from 10^2 to 10^6 Hz. Steps are observed in each capacitance spectrum at different temperatures. The transition frequency, where the capacitance step lies, can be found by taking the derivative of the capacitance spectra as shown in Fig. 4.5 (b). The energy levels of the defects can be obtained by linearly fitting the Arrhenius plot of the transition frequencies as illustrated in Fig. 4.5 (c). The energy level of the defect in perovskite solar cell fabricated using low purity PbI_2 with Cl is fitted to be 208.48 meV above the valence band, which is close to the energy levels of the defects in other samples (Fig. 4.6). The defect levels revealed in this work are different from the defect level of 167 meV found by Duan et al., which can be ascribed to the iodine interstitials [104, 130]. Samiee et al. found a defect level of 240 meV [103]. The origin of these two defects is not clear, which could be the impurities of the raw materials of perovskite thin films. The defect densities as a function of energy at different temperatures can be deduced from the differentiated capacitance spectra as shown in Fig. 4.5 (d).

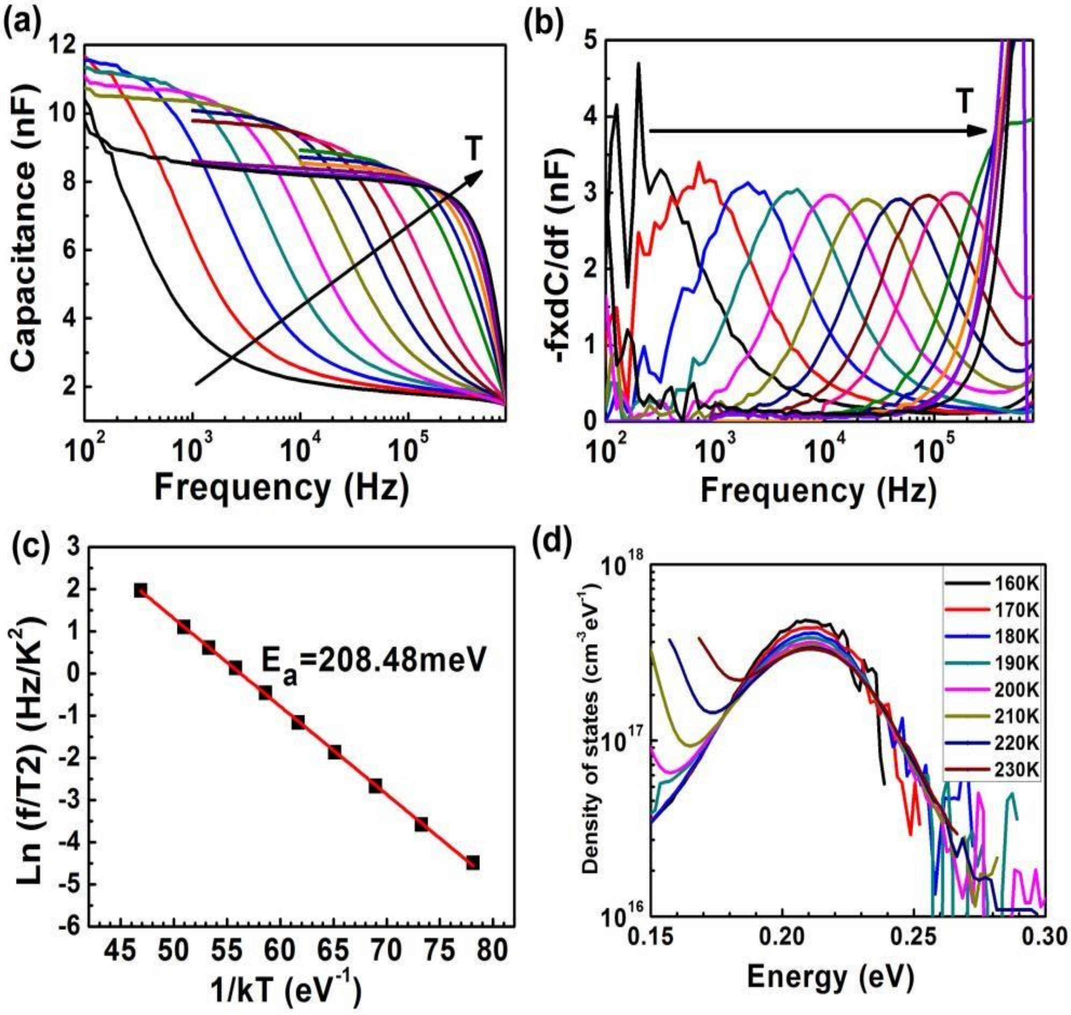

Figure 4.5 Admittance spectroscopy of perovskite solar cell fabricated using low purity PbI_2 with Cl. (a) Capacitance spectra at different temperatures. (b) The derivative of the capacitance spectra which show the transition frequency at each temperature. (c) Arrhenius plot of the transition frequencies to derive the defect energy level. (d) The distribution of the density of the defect.

The obtained defect energy distributions of perovskite solar cells are shown in Fig. 4.7. The defect states can be fitted as Gaussian distributions (solid lines). The integrated defect density of high purity perovskite solar cell is 2.79×10^{16} cm^{-3}. As expected, the defect density of low purity sample is higher (4.68×10^{16} cm^{-3}). Surprisingly, the defect density is reduced to 2.34×10^{16} cm^{-3} once Cl is added to low purity sample. Besides the effects of Cl on morphology and crystal structure as mentioned above, another reported effect is the longer carrier lifetime in Cl-incorporated perovskite thin film revealed by photoluminescence (PL) spectroscopy [121, 131]. It is often assumed that this longer carrier lifetime is attributed to reduced defect density [132], which has never been experimentally approved for perovskite solar cells. This is the first time that reduced defect density is experimentally observed in Cl-incorporated perovskite solar cells. The result is in good agreement with what has been observed in the electron lifetime measurement: Cl helps to passivate the defects in low purity perovskite solar cells, leading to a lower defect density and higher electron lifetime.

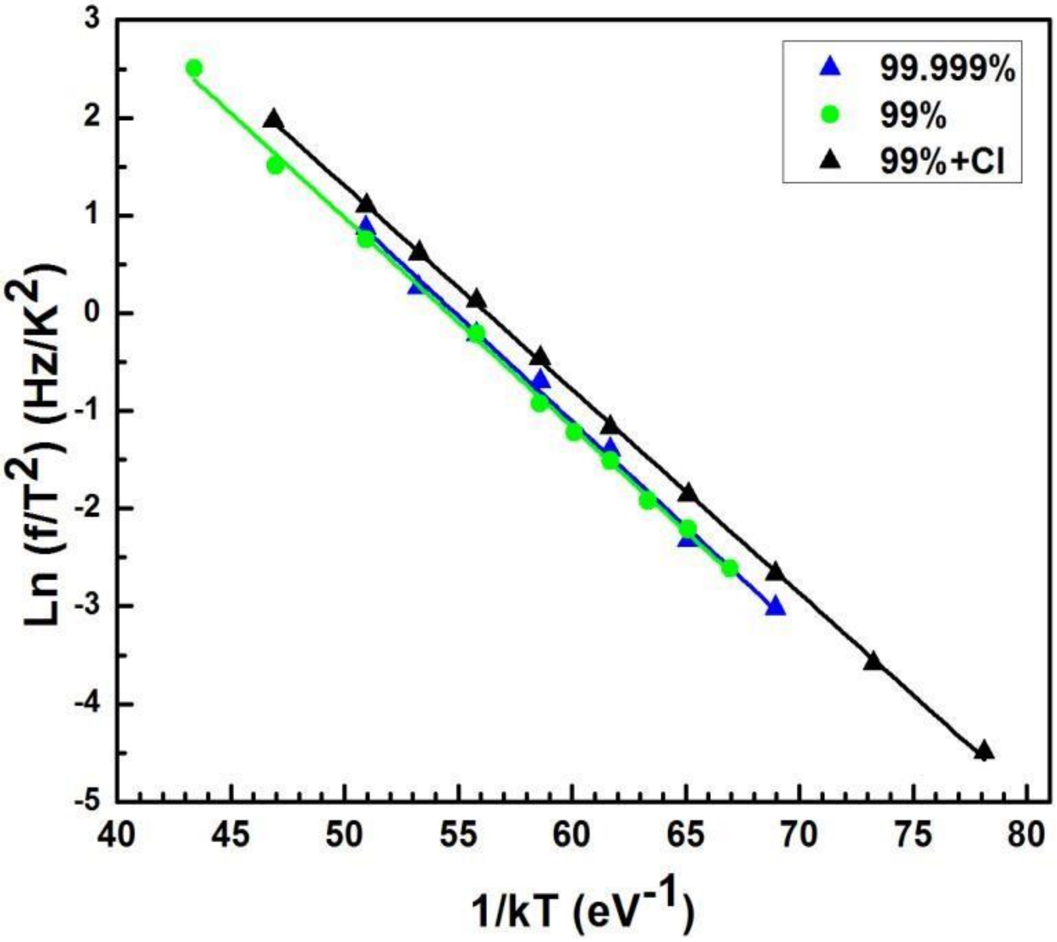

Figure 4.6 Arrhenius plots of the transition frequencies to derive the defect energy levels in perovskite solar cells utilizing different purities of PbI_2.

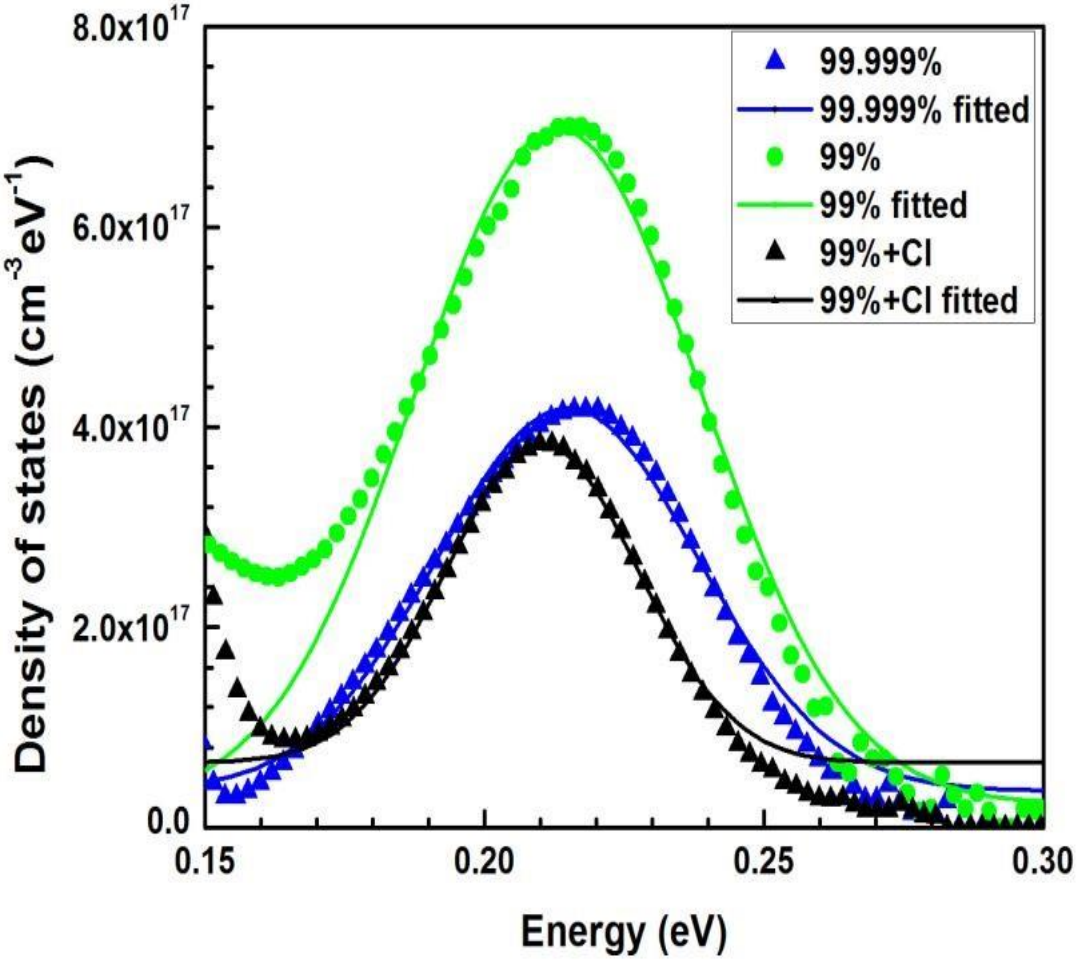

Figure 4.7 Defect density distributions of perovskite solar cell fabricated using different purities of PbI_2.

5.0 IMPROVED STABILITY OF MAPBI$_3$ SOLAR CELLS USING ALL INORGANIC CHARGE TRANSPORT LAYERS (CTLS)

Methylammonium lead halide perovskites (abbreviated as perovskite) have been proved as promising photovoltaic (PV) materials due to their excellent photoelectric properties [93]. Moreover, the abundant raw materials and the solution process capability make perovskite suitable for low cost PV technologies similarly as Cu(In,Ga)(S,Se)$_2$ (CIGS) and Cu$_2$ZnSn(S,Se)$_4$ (CZTS) for low cost PV technologies [57, 59, 87, 133]. The efficiency of perovskite solar cells has been rapidly improved from 3.8 % in 2009 [12] to 20.1% in 2015 [1]. This great advancement is mainly attributed to the numerous efforts that have been taken to deposit high quality perovskite thin films by many research groups [17-19]. The tremendous improvement can also be attributed to the two photovoltaic (PV) device structures developed for almost 20 years. One structure is based on TiO$_2$ as an electron transport layer (ETL) and 2,20,7,70-tetrakis(N,N-di-4-methoxyphenylamino)-9,90-spirobifluorene (spiro-OMeTAD) as a hole transport layer (HTL). The other structure is based on the organic ETL such as PCBM and organic HTL such as poly(3,4-ethylenedioxythiophene) polystyrene sulfonate (PEDOT:PSS) and poly(3-hexylthiophene-2,5-diyl) (P3HT). The perovskite thin film is deposited as an absorber layer to fabricate perovskite solar cells. Due to the high sensitivity of these organic materials to moisture and oxygen, a nitrogen glove box with a strict control of the moisture and oxygen levels was usually used to fabricate perovskite solar cells [17, 22-25]. However, the perovskite solar cells degrade rapidly once they are removed from the nitrogen glove box and stored in ambient environment [26-28].

It was reported that perovskite thin films were comparatively stable in ambient environment with low humidity [134]. The rapid degradation of perovskite solar cells was mainly caused by the instability of the organic charge transport layers (CTLs) [135, 136]. Encapsulation of perovskite solar cells was reported to be able to improve the stability of perovskite solar cells [137]. However, encapsulation is usually a final process step for fabrication of perovskite solar cells. The perovskite solar cell could have already degraded before being encapsulated. Another reported approach to improve the stability of perovskite solar cells was to use NiO_x thin film as HTL to replace those organic ones [138, 139]. Nevertheless, the remained organic ETL such as PCBM still significantly affect the stability of perovskite solar cells [135, 136]. The ultimate advancement in the device stability of perovskite solar cells has yet to be realized.

Here, solution-processed inorganic thin films, lithium (Li)-doped NiO_x ($Li:NiO_x$) and ZnO nanoparticles (NPs), were deposited as the HTL and ETL, respectively, to fabricate highly stable, highly performed planar perovskite solar cells. The devices were intentionally kept and tested in ambient environment without encapsulation to focus on the efficiency and stability. The employment of all inorganic thin films as CTLs has significantly improved the stability of perovskite solar cells compared to that of conventional perovskite solar cell structure with TiO_2 as the ETL and spiro-MeOTAD as the HTL. This study provides an excellent device structure for making highly stable and efficient perovskite solar cells.

5.1 EXPERIMENTAL PROCEDURES

5.1.1 Synthesis of ZnO Nanoparticles (NPs)

ZnO NPs were synthesized according to a reported procedure [140]. Zinc acetate dihydrate (molecular weight: 219.51) (2.95 g, 13.4 mmol) was dissolved in 125 ml methanol with stirring at 65 ℃. A solution of potassium hydroxide (molecular weight: 56.11) (1.48 g, 23 mmol) in 65 ml methanol was then added dropwise over a period of 15 min to the zinc acetate dehydrate solution. The reaction mixture was stirred for 2.5h at 65 ℃. After cooling to room temperature, the supernatant was decanted and the precipitate was washed twice with methanol (20 ml). n-butanol (70 ml), methanol (5 ml) and chloroform (5 ml) were added to disperse the precipitate and produce a ZnO NPs solution with a concentration of 6 mg/ml. Before use, the ZnO NPs solution was filtered through a 0.45 µm PVDF syringe filter.

5.1.2 Preparation of Li-doped NiOx (Li:NiOx) sol-gel

Li:NiOx sol-gel solution was prepared according to a reported procedure [141]. Nickel acetate tetrahydrate ($Ni(COOCH_3)_2 \cdot 4H_2O$, 746.52mg) was dissolved in 2-methoxyethanol (2ME) (10 ml), and 0.1 ml hydrochloric acid (HCl) was added as catalyst. Lithium acetate monohydrate ($LiCH_3COO \cdot H_2O$, 29.94 mg) was used as the dopant. The solution was stirred in water bath at 60 ℃for 1 h and then aged for 24 h at room temperature.

5.1.3 Fabrication of $MAPbI_3$ solar cell with all inorganic CTLs

The perovskite solar cell device structures studied in this work include: conventional structure, fluorine doped tin oxide (FTO) glass/TiO_2/perovskite/spiro-OMeTAD/Ag (Fig. 5.1 (a)), and the structure with all inorganic CTLs, FTO glass/Li:NiO_x/perovskite/ZnO NPs/Ag (Fig. 5.1 (b)). The perovskite thin films were deposited using the solvent-solvent extraction (SSE) method developed by Zhou et al. [142]. Li:NiO_x thin film was spin-coated using modified procedures reported in literature [143]. ZnO NPs were synthesized as reported and the coating procedures were optimized [144].

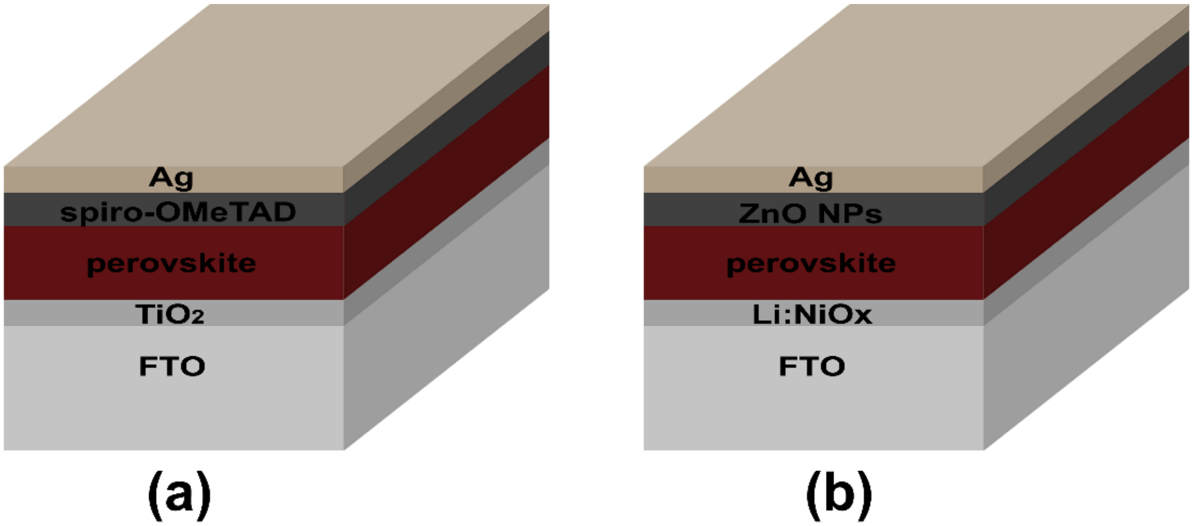

Figure 5.1 Schematic device structures of (a) conventional, and (b) all inorganic CTLs perovskite solar cells.

5.2 RESULTS AND ANALYSIS

The morphologies of the Li:NiO$_x$ thin film, perovskite thin film, and ZnO NPs were investigated by atomic force microscopy (AFM). To avoid the effects of the roughness of substrates, polished silicon wafers were used as substrates for AFM measurement. As shown in Fig. 5.2, no obvious voids can be observed in these films. The roughness of the Li:NiO$_x$, the ZnO NPs, the perovskite thin film is 0.49 nm, 2.32 nm, and 8.54 nm, respectively, indicating all films are smooth. These films are suitable for planar perovskite solar cells where the underlying layer is conveniently and fully covered by the upper layer. Direct shorting pathways are avoided.

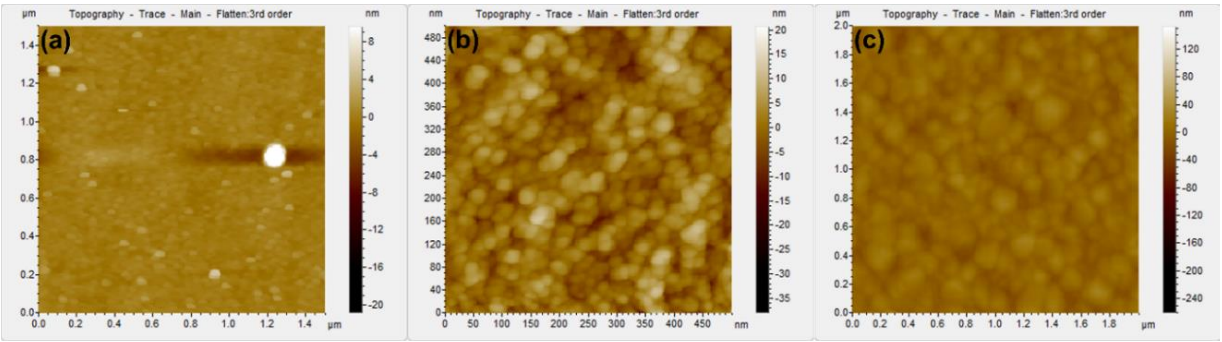

Figure 5.2 AFM images of the surface of (a) Li:NiO$_x$ thin film, (b) ZnO NPs, and (c)perovskite thin film.

Based on these results, perovskite solar cells were fabricated using the Li:NiO$_x$ thin film as HTL, and ZnO NPs as ETL. The thickness of Li:NiO$_x$ thin film was controlled to be around 25 nm (Fig. 5.3 (a) and (b)), while the thickness of ZnO NPs was approximately 10 nm (Fig. 5.3 (c) and (d)) because its comparatively low conductivity [145]. The thickness of perovskite thin film was kept at 350 nm which has been widely adopted in literatures [146, 147]. As an effort to improve the quality of the interface between the ZnO NPs and the perovskite thin film, half of the devices were annealed at 90 °C for 10 min before Ag contact was deposited.

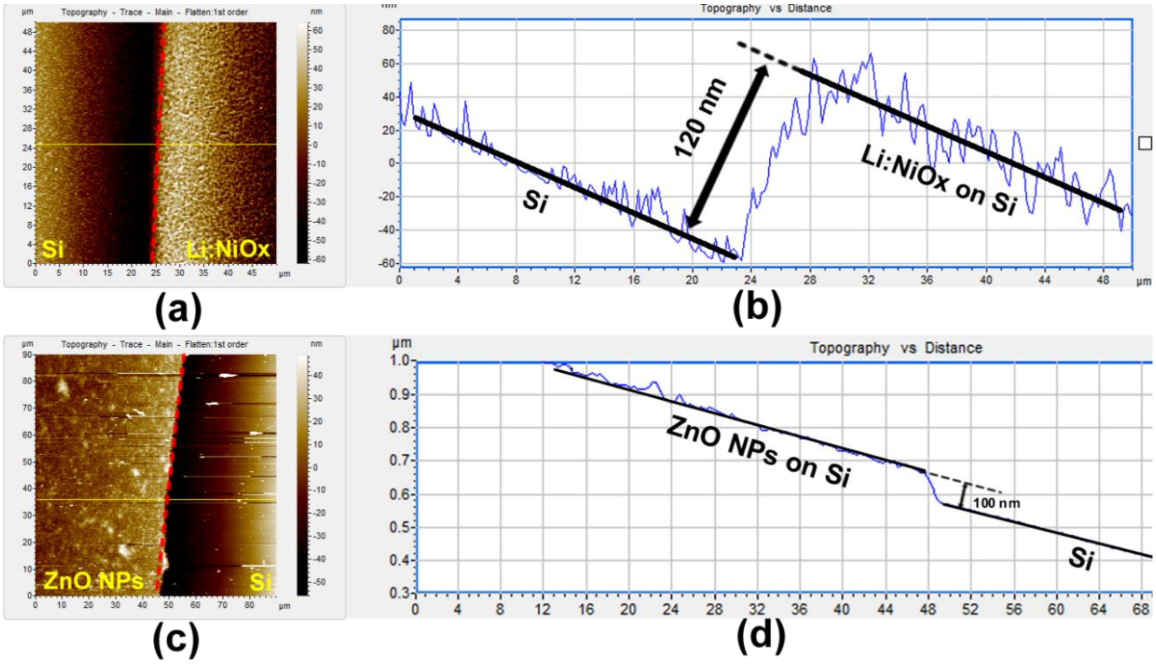

Figure 5.3 Thickness of (a) and (b) Li:NiO$_x$ thin film, (c) and (d) ZnO NPs deposited with 10 times coating.

The *J*-*V* characteristics of these perovskite solar cells under illumination were obtained. For comparison, perovskite solar cells with conventional structure of FTO/TiO$_2$/perovskite/spiro-

OMeTAD/Ag were also fabricated and characterized. It is worth nothing that all devices were fabricated and characterized in ambient environment. Ag was deposited using a high vacuum electron beam (EB) evaporation system. The *J-V* curves of the champion solar cell of each sample are shown in Fig. 5.4 and the *J-V* parameters are summarized in Table 5.1. The highest power conversion efficiency obtained from device with conventional structure of TiO_2/perovskite/spiro-OMeTAD was 14.8% with a J_{SC} of 22.3 mA/cm^2, a V_{OC} of 1.07 V, and a *FF* of 61.9 %. These parameters are comparable to those of the high-performance planar perovskite solar cells reported so far [17-19]. This is attributed to the high quality compact and smooth perovskite thin films which were deposited using SSE method [142].

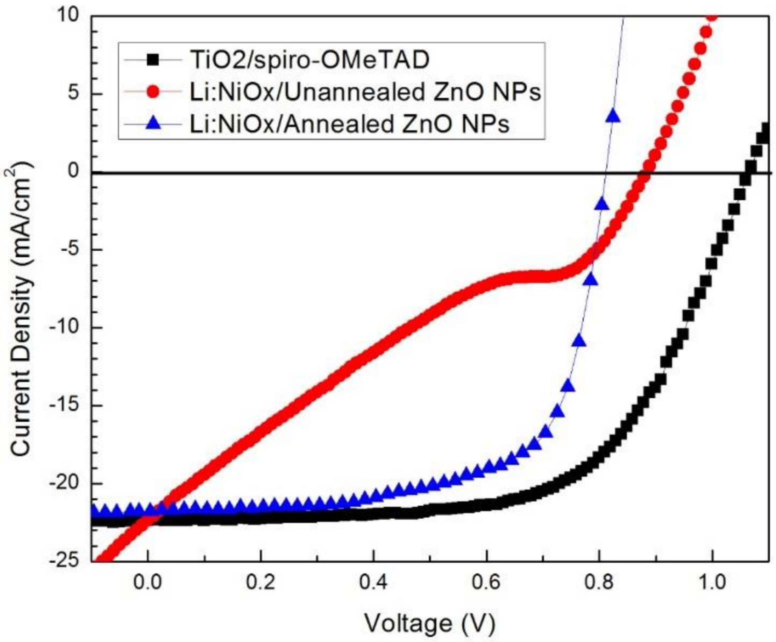

Figure 5.4 *J-V* curves of the champion perovskite solar cell with different device structures.

Table 5.1 *I-V* parameters the champion perovskite solar cell with different device structures.

	TiO_2/spiro-OMeTAD	Li:NiO_x/Unannealed ZnO NPs	Li:NiO_x/Annealed ZnO NPs
Eff. (%)	14.8	4.8	12.0
J_{SC} (mA/cm^2)	22.3	22.4	21.8
V_{OC} (V)	1.07	0.89	0.80
FF (%)	61.9	24.3	68.8

An efficiency of 12.0 % was achieved from the device with a structure of Li:NiO_x/perovskite/annealed ZnO NPs. Compared with the conventional perovskite solar cell, the efficiency is still low mainly due to the comparatively low V_{OC}. However, the efficiency of the device with structure of Li:NiO_x/perovskite/unannealed ZnO NPs is unexpectedly low. The main reason for low efficiency is its extremely low *FF*. The *FF* was significantly improved after an annealing step was applied before Ag was deposited. This annealing step probably improved the quality of the interface between the perovskite thin film and the ZnO NPs. The V_{OC} of the perovskite solar cell with annealed ZnO NPs is slightly lower than the unannealed one. To reveal the mechanism, the energy band diagrams of the three samples are shown in Fig. 5.5. All the values of the energy levels are obtained from literatures [148, 149]. The band gap of ZnO NPs with size of 5 nm is found to be 3.63 eV [150] and the band gap of annealed ZnO NPs is 3.54 eV [151]. Assuming the valence band keeps constant, the conduction band of the annealed ZnO NPs is lowered by 0.11 eV. This will bring two effects. First, the potential between the perovskite thin film and the ZnO NPs is increased, which will facilitate the transport of electrons from perovskite thin film to ZnO NPs, leading to higher *FF* and efficiency. Second, to a large extent, the V_{OC} in organic solar cell depends on the difference between the highest occupied molecular orbital

(*HOMO*) of HTL and the lowest unoccupied molecular orbital (*LUMO*) of ETL [152]. This could also be true for perovskite solar cells. When the conduction band of ZnO NPs is lowered, it will be closer to the valence band of Li:NiO$_x$. The difference between the *HOMO* of HTL and the *LUMO* of ETL is reduced, leading to a lower V_{OC}.

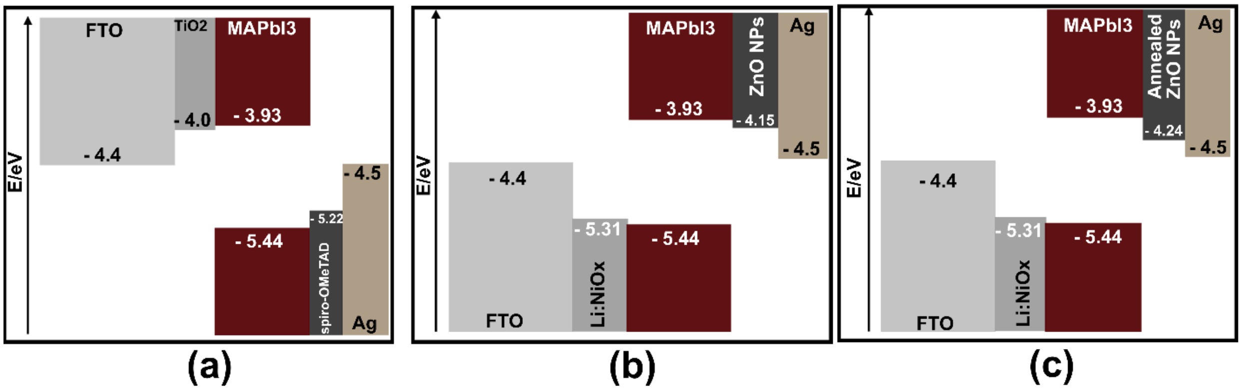

Figure 5.5 Energy band diagrams of perovskite solar cells with different device structures of (a) TiO2/spiro-OMeTAD, (b) Li:NiOx/unannealed ZnO NPs, (c) Li:NiOx/annealed ZnO NPs.

To demonstrate the robustness and repeatability of the process for fabricating perovskite solar cells with all inorganic CTLs developed in this work, 28 perovskite solar cells with device structure of Li:NiO$_x$/perovskite/annealed ZnO NPs were fabricated and tested. The distributions of *J–V* parameters are plotted in Fig. 5.6. An average efficiency of 7.7 % was achieved. Higher average efficiency is expected with further optimization of process. [153].

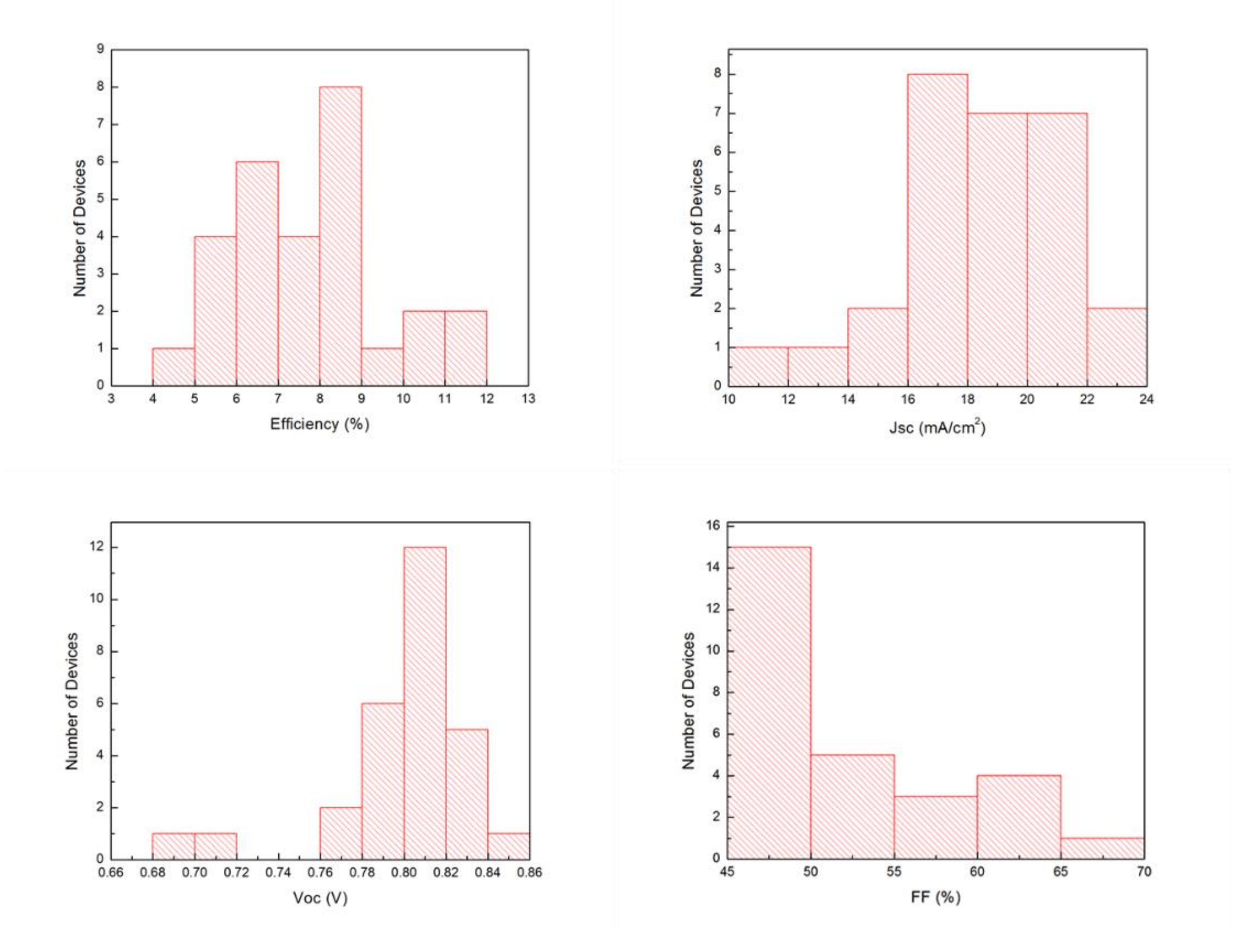

Figure 5.6 Distributions of *I*–*V* parameters obtained from 28 perovskite solar cells with device structure of Li:NiO$_x$/annealed ZnO NPs.

Spiro-OMeTAD was initially developed as a HTL in solid-state dye-sensitized solar cells (SSDSSCs) [154]. It has been widely used in highly efficient planar and mesoporous perovskite solar cells [15, 155]. The stability of perovskite solar cells with spiro-OMeTAD as the HTL has been much improved and is superior to that of perovskite solar cells that use other organic materials as HTLs [156]. So far, the device structure of TiO$_2$/perovskite/spiro-OMeTAD has been demonstrated to be one of the most stable perovskite solar cells. In order to demonstrate the advantages of the all inorganic CTL perovskite solar cells developed in this work, the perovskite solar cells with the conventional device structure of TiO_2/perovskite/spiro-OMeTAD and the device structure of Li:NiO_x/perovskite/ZnO NP were stored without encapsulation and tested in ambient environment at 22 ℃ with a relative humidity of 48.5 %. Fig. 5.7 shows the evolution of *J-V* parameters for typical devices from each device structure, which were stored in dark for 300 h. For each device structure, the *J-V* parameters were obtained from 8 solar cells with efficiencies ranging from 10 % to 5%. As shown in Fig. 4.32 (a), the efficiency of Li:NiO_x/ZnO NP structure was preserved 95 % of the initial performance, while the efficiency of TiO_2/spiro-OMeTAD structure rapidly decreased to 33 % after 100 h storage in dark. Remarkably, the J_{SC} of the Li:NiO_x/ZnO NP device improved during the first 50 h, while the V_{OC} and *FF* relatively unchanged. For devices with the TiO_2/spiro-OMeTAD structure, the J_{SC} and V_{OC} decreased rapidly, while the FF fluctuated. Unexpectedly, the efficiency of TiO_2/spiro-OMeTAD device was degraded to less than 1 % of its initial efficiency after 170 h. This was mainly caused by the severe degradation of V_{OC} which only preserved 3 % of its initial value. At this point, the efficiency of Li:NiO_x/ZnO NP device preserved 92 % mainly caused by the slight degradation of J_{SC}. The stability test of Li:NiO_x/ZnO NP device was continued to 300 h, while that of TiO_2/spiro-OMeTAD device was stopped at 170 h. At the end of the test, the values of V_{OC} and FF were comparable to their initial values. The J_{SC} slowly degraded to 62 %. As a result, the efficiency of Li:NiO_x/ZnO NP device was preserved 61 % of the initial value.

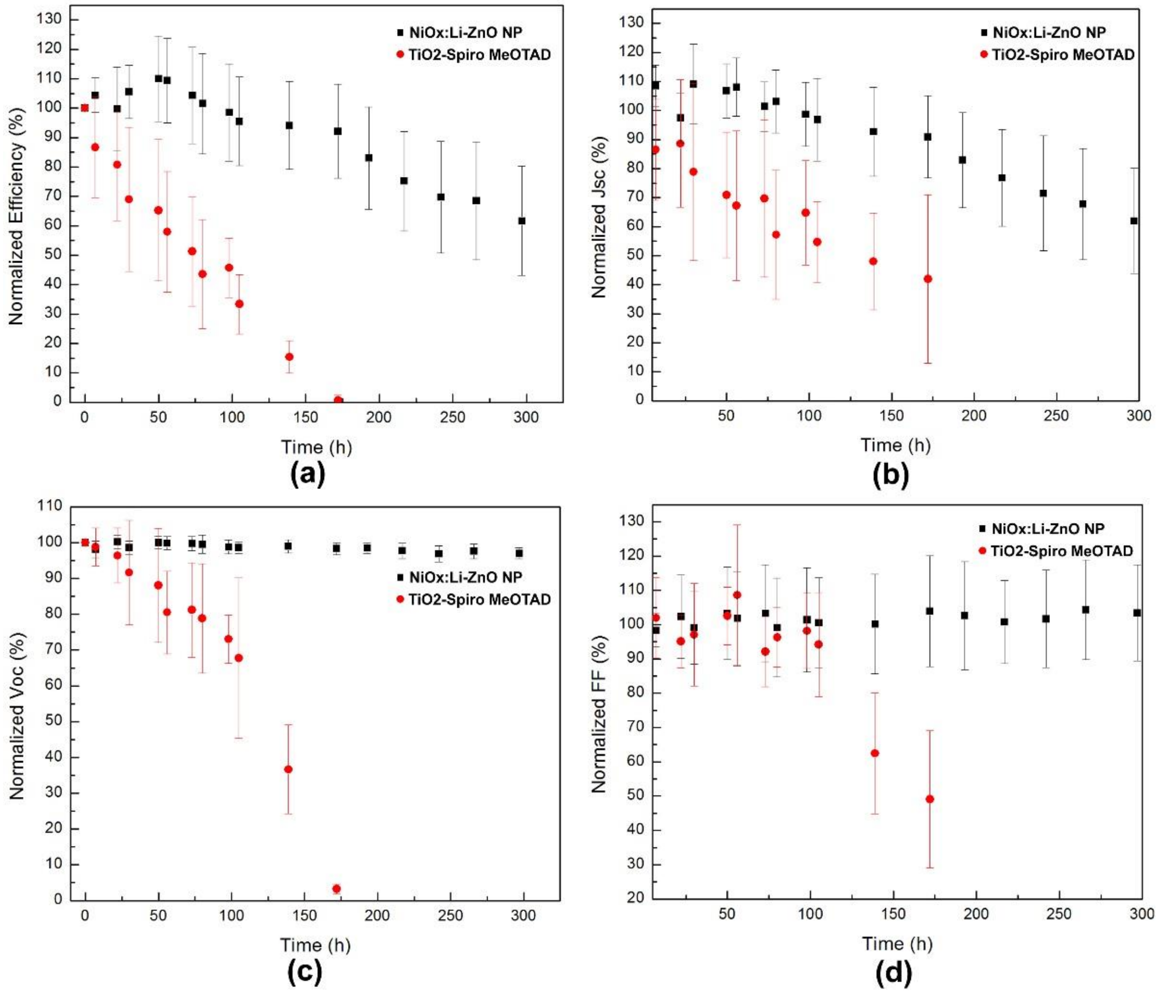

Figure 5.7 Variation of the normalized *I-V* parameters of the perovskite solar cells with time stored in air at room temperature without encapsulation.

For the TiO_2/spiro-OMeTAD device, both the spiro-OMeTAD and the perovskite thin film could degrade due to moisture. The junction between the spiro-OMeTAD and the perovskite was possibly damaged after exposure to high humidity, leading to rapid degradation of the device. For the Li:NiO_x/ZnO NP device, all other materials are stable on exposure to moisture except for the perovskite thin film which decomposes into MAI and PbI_2. The decomposed perovskite will no longer contribute to the photocurrent, resulting to lower J_{SC}. Nevertheless, moisture is more likely to damage the bulk perovskite through grain boundaries, leaving a large part of the surface of the perovskite thin film intact. Therefore, the junction between the perovskite thin film and the ZnO NP thin film has a chance to preserve its quality, resulting in a negligible degradation of V_{OC} and FF even if the devices were kept in air with a relative humidity of 48.5 % for 300 h. There are two possible solutions to improve the stability of perovskite solar cells. First, a process capable of depositing perovskite thin film with larger crystal size needs to be developed to reduce the number of paths through which the moisture gets to the bulk perovskite. Second, the metal oxides with decent ambient stability have obvious advantages over those organic CTLs. Their properties should be further investigated and developed for perovskite solar cells.

As mentioned earlier, the conventional perovskite solar cell adopted a device structure which have been developed for almost 20 years, while the device structure with all inorganic CTLs proposed in this work is new. It is reasonable to expect that its performance would be significantly improved with further optimization. As a hint, spiro-OMeTAD used in this work was doped with a lithium salt, which is a common procedure to increase the conductivity of spiro-OMeTAD, leading to higher performance of solid-state dye-sensitized solar cells (SSDSSCs) and perovskite solar cells [157]. Doping of ZnO NPs, which will increase the conductivity of ZnO NPs [158], could be a strategy to improve the efficiency of perovskite solar cells with the device structure developed in this work.

6.0 FUTURE WORK AND CONCLUSION

6.1 FUTURE WORK

6.1.1 Interface Engineering of CZTS Solar Cells

As discussed earlier, while the defect density in perovskite solar cell is as high as 2.79×10^{16} cm^{-3}, more than 18% efficiency can still be obtained. Conversely, while the defect density in CZTS solar cell is lower than what is observed in perovskite solar cell (1×10^{16} cm^{-3}), the highest efficiency obtained is less than 13%. This indicates that the quality of the CZTS absorber layer is not the major factor which limits the performance of CZTS solar cell. The low quality of the interfaces, including the interface between CdS and CZTS and the interface between CZTS and Mo, could be the origins of the poor performance in CZTS solar cells.

The employment of CdS in CZTS solar cells was based on the experiences in developing CIGS solar cells. Although CdS is reportedly to be the best n-type semiconductor to form p-n junction in CZTS solar cells, it has yet to be optimized. Recently, it has been found that the built-in homogeneous p-n junction observed in CIGS solar cell due to the diffusion of Cd into CIGS thin film does not exist in CZTS solar cell [159, 160]. This indicates that the photo-excited electrons and holes in CZTS must be separated by the heterogeneous p-n junction formed by CdS and CZTS, leading to higher possibility to be recombined. The quality of the interface of

CdS/CZTS should be improved by using alternative n-type semiconductors or by developing alternative coating processes for CdS thin films.

Similarly, the employment of Mo back contact in CZTS solar cells was also based on the experiences in developing CIGS solar cells. However, it has been found that the coating procedures which have worked pretty well with CIGS solar cell would resulted into formation of extremely thick $MoSe_2$ thin film, leading to high series resistance and deteriorated the device efficiency [161]. Materials such as TiN and TiB_2 have been deposited between the Mo and the CZTS to partly or completely suppress the formation of $MoSe_2$ thin film [162-164]. Other materials which will sufficiently suppress the formation of MoSe2 and effectively facilitate the transport of charges need to be explored.

6.1.2 Interface Engineering of $MAPbI_3$ Solar Cells

Li doping has been applied to enhance the conductivity of organic HTLs such as spiro-OMeTAD and P3HT, which greatly enhances the device efficiency of perovskite solar cells [157, 165]. For inorganic HTL such as NiO_x, Cu doping was reported to enhance its conductivity, leading to higher efficiency of perovskite solar cells [166]. Al doping is well known to improve the conductivity of ZnO thin films, ZnO nanorods, and ZnO nanoparticles [167-169]. The efficiency of solar cells was improved by using these doped materials [168]. As addressed in 4.3, the application of ZnO NPs as ETL has greatly improved the stability of perovskite solar cells. However, the efficiency lags behind. This is probably caused by the extremely low conductivity of ZnO NPs. Therefore, application of Al-doped ZnO NPs as ETL in perovskite solar cell can possibly improve both the efficiency and the stability of perovskite solar cells.

The *J-V* curves of the champion solar cell of each sample are shown in Fig. 6.1 and corresponding *I-V* parameters, namely, the conversion efficiency (*Eff.*), short-circuit current density (J_{SC}), fill factor (*FF*), and open circuit voltage (V_{OC}), which are derived from Fig. 4.38, are summarized in the table inserted in Fig. 4.38. The best perovskite solar cell without Al-doped ZnO NPs produced a J_{SC} of 18.37 mA/cm^2, a V_{OC} of 0.81 V and a *FF* of 63.2 %, while the most efficient perovskite solar cell with Al-doped ZnO solar cell had a J_{SC} of 21.52 mA/cm^2, a V_{OC} of 0.91 V and a *FF* of 55.99 %. As a result, the efficiency of perovskite solar cell was improved from 9.41 % to 10.95 %. The reasons of the enhancement of photovoltaic parameters were investigated and discussed below.

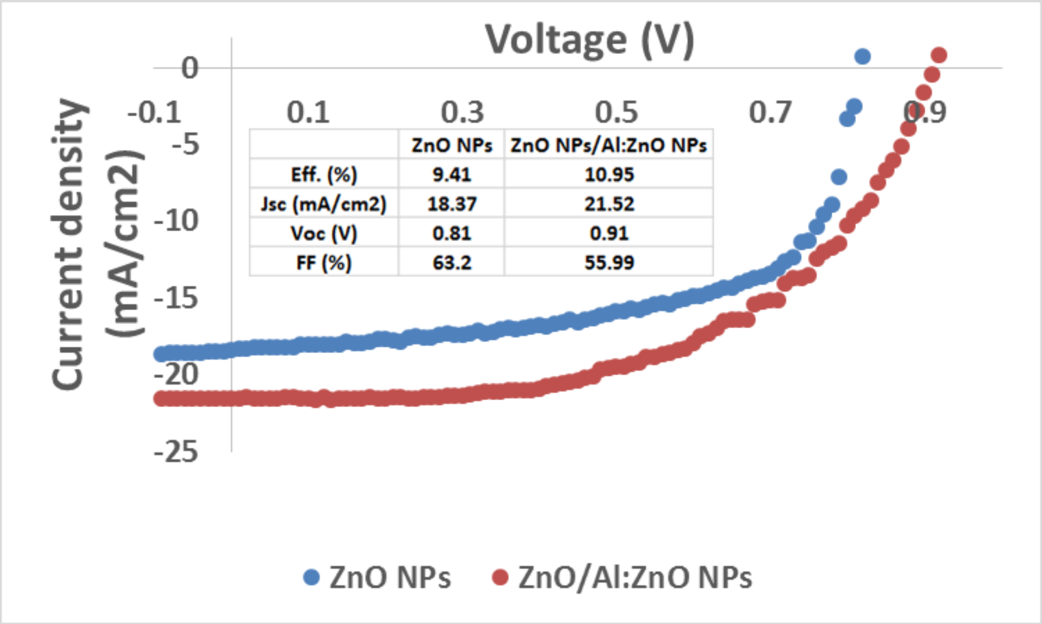

	ZnO NPs	ZnO NPs/Al:ZnO NPs
Eff. (%)	9.41	10.95
Jsc (mA/cm2)	18.37	21.52
Voc (V)	0.81	0.91
FF (%)	63.2	55.99

Figure 6.1 *J-V* curves of the champion perovskite solar cells with and without Al-doped ZnO NPs.

The noticeable improvement of the perovskite solar cell with Al-doped ZnO NPs is the increased *Jsc* and enhanced *Voc*, while the *FF* is slightly degraded. For *FF*, the affecting mechanisms are more complex than those of *Jsc* and *Voc*. For *Jsc* and *Voc*, the major factor is the recombination processes, either in the bulk, or at the interfaces. For the perovskite solar cells with and without Al-doped ZnO NPs, the only difference is the interface between ZnO NPs and the Ag contact. With a layer of Al-doped ZnO NPs, the interface between ZnO NPs and Ag contact could be improved, as what was observed in CIGS solar cells, leading to higher *Jsc* and *Voc*. As clearly demonstrated in Fig. 6.2, which shows the statistical distributions of the *Voc* of perovskite solar cells with and without Al-doped ZnO NPs, the inclusion of Al-doped ZnO NPs between the ZnO NPs and the Ag contact definitely improved the *Voc* of perovskite solar cells, indicating the recombination at the interface between the ZnO NPs and the Ag contact was suppressed.

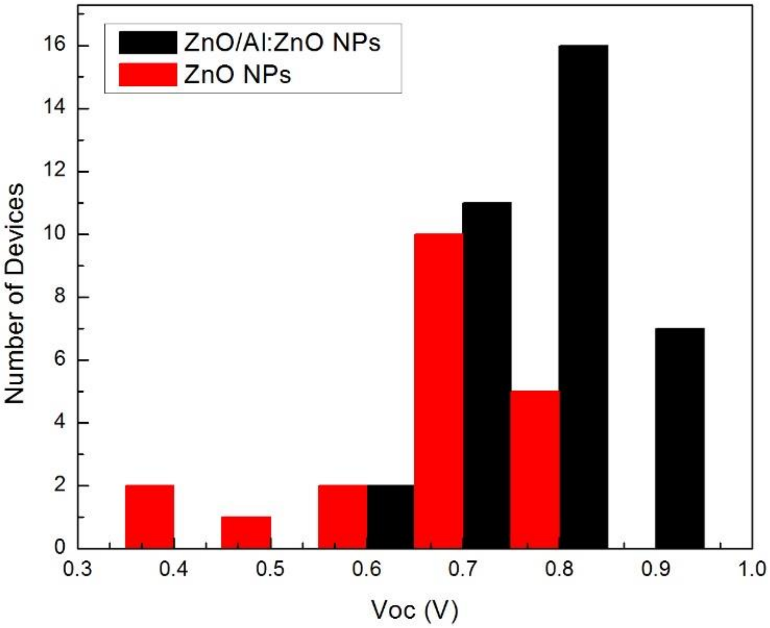

Figure 6.2 The statistical distributions of the Voc of perovskite solar cells with and without Al-doped ZnO NPs.

The temperature dependence of *Voc* of perovskite solar cells with and without Al-doped ZnO NPs are shown in Fig. 6.3. The intercept of the *Voc* versus *T* plot at 0K for perovskite solar cells without Al-doped ZnO NPs yields the *Ea* of 1.31eV, which is significantly lower than the band gap of the absorber layer, while that of perovskite solar cells with Al-doped ZnO NPs is 1.57 eV, which is the same as the band gap of the absorber layer. This indicates that the dominant recombination process occurs in the charge transport layer-absorber interfaces for perovskite solar cells without Al-doped ZnO NPs, while the dominant recombination process occurs in the space charge region for perovskite solar cells with Al-doped ZnO NPs. The inclusion of Al-doped ZnO

NPs between the ZnO NPs and the Ag contact can improve the interface by suppressing the interfacial recombination, leading to higher performance.

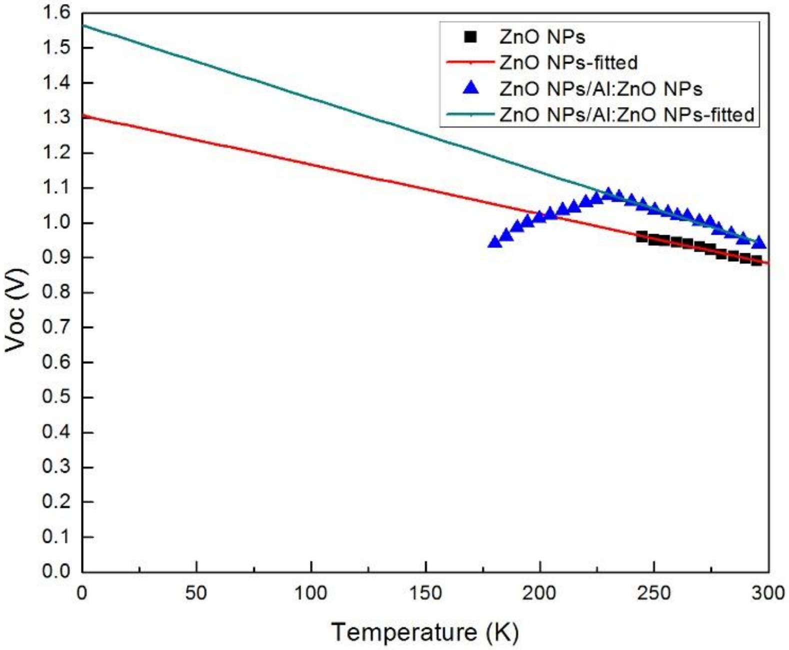

Figure 6.3 Temperature dependence of the *Voc* and its linear extrapolation line to 0 K for perovskite solar cells with and without Al-doped ZnO NPs, which helps to elucidate the dominant recombination process in the two types of devices.

While the utilization of Al-doped ZnO NPs can enhance the Voc of perovskite solar cells and therefore increase the performance of perovskite solar cells, the efficiency obtained so far is still lower than what has been obtained from perovskite solar cells with conventional structures.

Investigation on the cross section of the device using KPFM can possibly reveal how the charges are transported and where the improvement could be achieved.

6.1.3 Effects of impurities in $MAPbI_3$ Solar Cells

Cl doping has been demonstrated to be capable of effectively improve the performance of perovskite solar cells. Furthermore, introduction of negligible amount of Cl into low purity $MAPbI_3$ solar cell can significantly boost the performance. Therefore, the concentration of Cl in perovskite thin film will be investigated. Also, how and where Cl lies in perovskite thin film will also be studied. Furthermore, the impurities in PbI_2 will be revealed and their effects on the performance of perovskite solar cells will be investigated. By combining theoretical calculations with experimental results, the mechanisms behind the Cl doping-associated improvement of performance of perovskite solar cells made from low purity PbI_2 will be revealed. Doping of perovskite thin films with alternative materials with expectation to enhance device performance will be explored. The alternative doping procedures are expected to neutralize the impurities in PbI_2, passivate the grain boundaries of perovskite thin film, and improve the lifetime of the carriers.

6.2 CONCLUSION

The properties of the CZTS thin films deposited by the water-based method are greatly affected by the Se feeding time. Varying the time from 0 to 30 min resulted in CZTS thin films with ratios of Se/(Se+S) varying from 0 to 25%. The extension of Se vapor feeding time increases the bandgap, slightly increases the lattice parameters, and significantly improves the morphologies of the CZTS thin films. A remarkable enhancement of performance was achieved from the CZTS solar cells with longer Se vapor feeding times compared to those without Se vapor feeding.

The mixed halide source method proposed in this work can be applied to combine the advantages of a modified one-step process and Cl incorporation. A larger band bending at grain boundaries with Cl incorporation, revealed by KPFM measurement, suggest that a p-i-n type of heterojunction junction is formed in the devices with Cl incorporation. The p-i-n junction facilitates the charge carrier collection and reduces recombination. Planar perovskite solar cells with uniform morphology can be fabricated by the two-step solution process and the performance can be improved by the Cl incorporation. This technique can be easily combined with other highly efficient growth methods. Higher performance could be expected for solution-processed, planar perovskite solar cells.

Additionally, we have successfully prepared inorganic metal oxides which can be used as CTLs in highly performed perovskite solar cells. The stability of the perovskite solar cells has been significantly enhanced due to the stability of these inorganic metal oxides in ambient environment. The slow degradation observed in corresponding perovskite solar cells was suggested to be mainly caused by the moisture infiltrated into the perovskite thin film through grain boundaries, while the rapid loss of performance observed in the conventional perovskite solar cell with device structure of TiO_2/spiro-OMeTAD resulted from the degradation of the perovskite thin film and the junction. This study provides an excellent device structure for making highly stable and efficient perovskite solar cells.

Finally, the defect density of CZTS solar cell is reported to be 1×10^{16} cm^{-3}, while that of perovskite solar cell is found to be more than 2×10^{16} cm^{-3}. Although the defect density in perovskite solar cell is higher than that in CZTS solar cell, the efficiency obtained so far from perovskite solar cell is much higher than that obtained from CZTS solar cell. This indicates that the quality of the interfaces in CZTS solar cell is much worse than that of perovskite solar cell, and should be prioritized in the future work.

BIBLIOGRAPHY

[1] Available: http://www1.umn.edu/iree/e3/archive/archive_2010/E3_Aydil.pdf

[2] M. A. Green, "Estimates of Te and In Prices from Direct Mining of Known Ores," *Progress in Photovoltaics,* vol. 17, pp. 347-359, Aug 2009.

[3] W. Wang, M. T. Winkler, O. Gunawan, T. Gokmen, T. K. Todorov, Y. Zhu, *et al.*, "Device Characteristics of CZTSSe Thin-Film Solar Cells with 12.6% Efficiency," *Advanced Energy Materials,* vol. 4, May 2014.

[4] N. J. Jeon, J. H. Noh, W. S. Yang, Y. C. Kim, S. Ryu, J. Seo, *et al.*, "Compositional engineering of perovskite materials for high-performance solar cells," *Nature,* vol. 517, pp. 476-480, 01/22/print 2015.

[5] S. Wagner and P. M. Bridenbaugh, "Multicomponent tetrahedral compounds for solar cells," *Journal of Crystal Growth,* vol. 39, pp. 151-159, 7// 1977.

[6] I. Kentaro and N. Tatsuo, "Electrical and Optical Properties of Stannite-Type Quaternary Semiconductor Thin Films," *Japanese Journal of Applied Physics,* vol. 27, p. 2094, 1988.

[7] H. Katagiri, N. Sasaguchi, S. Hando, S. Hoshino, J. Ohashi, and T. Yokota, "Preparation and evaluation of Cu_2ZnSnS_4 thin films by sulfurization of E · B evaporated precursors," *Solar Energy Materials and Solar Cells,* vol. 49, pp. 407-414, 12// 1997.

[8] R. Haight, A. Barkhouse, O. Gunawan, B. Shin, M. Copel, M. Hopstaken, *et al.*, "Band alignment at the $Cu_2ZnSn(S_xSe_{1-x})_4$/CdS interface," *Applied Physics Letters,* vol. 98, Jun 20 2011.

[9] S. Y. Chen, J. H. Yang, X. G. Gong, A. Walsh, and S. H. Wei, "Intrinsic point defects and complexes in the quaternary kesterite semiconductor Cu_2ZnSnS_4," *Physical Review B,* vol. 81, Jun 8 2010.

[10] P. Jackson, D. Hariskos, R. Wuerz, O. Kiowski, A. Bauer, T. M. Friedlmeier, *et al.*, "Properties of $Cu(In,Ga)Se_2$ solar cells with new record efficiencies up to 21.7%," *Physica Status Solidi-Rapid Research Letters,* vol. 9, pp. 28-31, Jan 2015.

[11] L. Yin, G. M. Cheng, Y. Feng, Z. H. Li, C. L. Yang, and X. D. Xiao, "Limitation factors for the performance of kesterite Cu_2ZnSnS_4 thin film solar cells studied by defect characterization," *Rsc Advances,* vol. 5, pp. 40369-40374, 2015.

[12] A. Kojima, K. Teshima, Y. Shirai, and T. Miyasaka, "Organometal Halide Perovskites as Visible-Light Sensitizers for Photovoltaic Cells," *Journal of the American Chemical Society,* vol. 131, pp. 6050-6051, 2009/05/06 2009.

[13] J.-H. Im, C.-R. Lee, J.-W. Lee, S.-W. Park, and N.-G. Park, "6.5% efficient perovskite quantum-dot-sensitized solar cell," *Nanoscale,* vol. 3, pp. 4088-4093, 2011.

[14] H.-S. Kim, C.-R. Lee, J.-H. Im, K.-B. Lee, T. Moehl, A. Marchioro*, et al.*, "Lead Iodide Perovskite Sensitized All-Solid-State Submicron Thin Film Mesoscopic Solar Cell with Efficiency Exceeding 9%," *Sci. Rep.*, vol. 2, 08/21/online 2012.

[15] J. Burschka, N. Pellet, S.-J. Moon, R. Humphry-Baker, P. Gao, M. K. Nazeeruddin*, et al.*, "Sequential deposition as a route to high-performance perovskite-sensitized solar cells," *Nature,* vol. 499, pp. 316-319, 07/18/print 2013.

[16] M. Liu, M. B. Johnston, and H. J. Snaith, "Efficient planar heterojunction perovskite solar cells by vapour deposition," *Nature,* vol. 501, pp. 395-398, 09/19/print 2013.

[17] M. Xiao, F. Huang, W. Huang, Y. Dkhissi, Y. Zhu, J. Etheridge*, et al.*, "A Fast Deposition-Crystallization Procedure for Highly Efficient Lead Iodide Perovskite Thin-Film Solar Cells," *Angewandte Chemie International Edition,* vol. 53, pp. 9898-9903, 2014.

[18] C.-W. Chen, H.-W. Kang, S.-Y. Hsiao, P.-F. Yang, K.-M. Chiang, and H.-W. Lin, "Efficient and Uniform Planar-Type Perovskite Solar Cells by Simple Sequential Vacuum Deposition," *Advanced Materials,* vol. 26, pp. 6647-6652, 2014.

[19] J.-W. Lee, D.-J. Seol, A.-N. Cho, and N.-G. Park, "High-Efficiency Perovskite Solar Cells Based on the Black Polymorph of $HC(NH_2)_2PbI_3$," *Advanced Materials,* vol. 26, pp. 4991-4998, 2014.

[20] A. Suzuki, H. Okada, and T. Oku, "Fabrication and Characterization of $CH_3NH_3PbI_{3-x-y}Br_xCl_y$ Perovskite Solar Cells," *Energies,* vol. 9, May 2016.

[21] C. C. Chen, Z. R. Hong, G. Li, Q. Chen, H. P. Zhou, and Y. Yang, "One-step, low-temperature deposited perovskite solar cell utilizing small molecule additive," *Journal of Photonics for Energy,* vol. 5, Jan 16 2015.

[22] D. Vak, K. Hwang, A. Faulks, Y.-S. Jung, N. Clark, D.-Y. Kim*, et al.*, "3D Printer Based Slot-Die Coater as a Lab-to-Fab Translation Tool for Solution-Processed Solar Cells," *Advanced Energy Materials,* vol. 5, pp. n/a-n/a, 2015.

[23] M. Lv, X. Dong, X. Fang, B. Lin, S. Zhang, J. Ding*, et al.*, "A promising alternative solvent of perovskite to induce rapid crystallization for high-efficiency photovoltaic devices," *RSC Advances,* vol. 5, pp. 20521-20529, 2015.

[24] P.-W. Liang, C.-Y. Liao, C.-C. Chueh, F. Zuo, S. T. Williams, X.-K. Xin*, et al.*, "Additive Enhanced Crystallization of Solution-Processed Perovskite for Highly Efficient Planar-Heterojunction Solar Cells," *Advanced Materials,* vol. 26, pp. 3748-3754, 2014.

[25] D. Yang, Z. Yang, W. Qin, Y. Zhang, S. Liu, and C. Li, "Alternating precursor layer deposition for highly stable perovskite films towards efficient solar cells using vacuum deposition," *Journal of Materials Chemistry A,* vol. 3, pp. 9401-9405, 2015.

[26] H. Zhou, Q. Chen, G. Li, S. Luo, T.-b. Song, H.-S. Duan*, et al.*, "Interface engineering of highly efficient perovskite solar cells," *Science,* vol. 345, pp. 542-546, August 1, 2014 2014.

[27] S. N. Habisreutinger, T. Leijtens, G. E. Eperon, S. D. Stranks, R. J. Nicholas, and H. J. Snaith, "Carbon Nanotube/Polymer Composites as a Highly Stable Hole Collection Layer in Perovskite Solar Cells," *Nano Letters,* vol. 14, pp. 5561-5568, 2014/10/08 2014.

[28] J. H. Noh, S. H. Im, J. H. Heo, T. N. Mandal, and S. I. Seok, "Chemical Management for Colorful, Efficient, and Stable Inorganic-Organic Hybrid Nanostructured Solar Cells," *Nano Letters,* vol. 13, pp. 1764-1769, Apr 2013.

[29] Y. Yamada, T. Nakamura, M. Endo, A. Wakamiya, and Y. Kanemitsu, "Photocarrier Recombination Dynamics in Perovskite $CH_3NH_3PbI_3$ for Solar Cell Applications," *Journal of the American Chemical Society,* vol. 136, pp. 11610-11613, 2014/08/20 2014.

[30] M. Powalla, M. Cemernjak, J. Eberhardt, F. Kessler, R. Kniese, H. D. Mohring*, et al.*, "Large-area CIGS modules: Pilot line production and new developments," *Solar Energy Materials and Solar Cells,* vol. 90, pp. 3158-3164, Nov 23 2006.

[31] C. S. Jiang, R. Noufi, J. A. AbuShama, K. Ramanathan, H. R. Moutinho, J. Pankow*, et al.*, "Local built-in potential on grain boundary of $Cu(In,Ga)Se_2$ thin films," *Applied Physics Letters,* vol. 84, pp. 3477-3479, May 3 2004.

[32] I. Visoly-Fisher, S. R. Cohen, K. Gartsman, A. Ruzin, and D. Cahen, "Understanding the beneficial role of grain boundaries in polycrystalline solar cells from single-grain-boundary scanning probe microscopy," *Advanced Functional Materials,* vol. 16, pp. 649-660, Mar 20 2006.

[33] A. Zaban, M. Greenshtein, and J. Bisquert, "Determination of the Electron Lifetime in Nanocrystalline Dye Solar Cells by Open-Circuit Voltage Decay Measurements," *ChemPhysChem,* vol. 4, pp. 859-864, 2003.

[34] S. R. Lederhandler and L. J. Giacoletto, "Measurement of Minority Carrier Lifetime and Surface Effects in Junction Devices," *Proceedings of the Institute of Radio Engineers,* vol. 43, pp. 477-483, 1955.

[35] T. Pisarkiewicz, "Photodecay method in investigation of materials and photovoltaic structures," *Opto-Electronics Review,* vol. 12, pp. 33-40, Mar 2004.

[36] G. P. Li and K. L. Wang, "Detection Sensitivity and Spatial-Resolution of Reverse-Bias Pulsed Deep-Level Transient Spectroscopy for Studying Electric Field-Enhanced Carrier Emission," *Journal of Applied Physics,* vol. 57, pp. 1016-1021, 1985.

[37] J. H. a. P. Zabierowski, *Advanced Characterization Techniques for Thin Film Solar Cells*: Wiley-VCH, 2011.

[38] A. Jasenek, U. Rau, V. Nadenau, and H. W. Schock, "Electronic properties of $CuGaSe_2$-based heterojunction solar cells. Part II. Defect spectroscopy," *Journal of Applied Physics,* vol. 87, pp. 594-602, 2000.

[39] M. Rusu, W. Eisele, R. Wurz, A. Ennaoui, M. C. Lux-Steiner, T. P. Niesen*, et al.*, "Current transport in ZnO/ZnS/Cu(In,Ga)$(S,Se)_2$ solar cell," *Journal of Physics and Chemistry of Solids,* vol. 64, pp. 2037-2040, Sep-Oct 2003.

[40] D. B. Mitzi, O. Gunawan, T. K. Todorov, and D. A. R. Barkhouse, *Prospects and performance limitations for Cu–Zn–Sn–S–Se photovoltaic technology* vol. 371, 2013.

[41] A. Doukkali, S. Ledain, C. Guasch, and J. Bonnet, "Surface potential mapping of biased pn junction with kelvin probe force microscopy: application to cross-section devices," *Applied surface science*, vol. 235, pp. 507-512, 2004.

[42] F. Lan and G. Li, "Direct Observation of Hole Transfer from Semiconducting Polymer to Carbon Nanotubes," *Nano Letters,* vol. 13, pp. 2086-2091, 2013/05/08 2013.

[43] C.-S. Jiang, M. Yang, Y. Zhou, B. To, S. U. Nanayakkara, J. M. Luther*, et al.*, "Carrier separation and transport in perovskite solar cells studied by nanometre-scale profiling of electrical potential," *Nature communications,* vol. 6, 2015.

[44] R. Saive, M. Scherer, C. Mueller, D. Daume, J. Schinke, M. Kroeger*, et al.*, "Imaging the electric potential within organic solar cells," *Advanced Functional Materials,* vol. 23, pp. 5854-5860, 2013.

[45] Q. Chen, L. Mao, Y. Li, T. Kong, N. Wu, C. Ma*, et al.*, "Quantitative operando visualization of the energy band depth profile in solar cells," *Nature communications,* vol. 6, 2015.

[46] G. Li, B. Mao, F. Lan, and L. Liu, "Practical aspects of single-pass scan Kelvin probe force microscopy," *Review of Scientific Instruments,* vol. 83, p. 113701, 2012.

[47] W. Wang, M. T. Winkler, O. Gunawan, T. Gokmen, T. K. Todorov, Y. Zhu, *et al.*, "Device Characteristics of CZTSSe Thin-Film Solar Cells with 12.6% Efficiency," *Advanced Energy Materials*, vol. 4, pp. n/a-n/a, 2014.

[48] I. Repins, C. Beall, N. Vora, C. DeHart, D. Kuciauskas, P. Dippo, *et al.*, "Co-evaporated $Cu_2ZnSnSe_4$ films and devices," *Solar Energy Materials and Solar Cells*, vol. 101, pp. 154-159, 6// 2012.

[49] K. Woo, Y. Kim, and J. Moon, "A non-toxic, solution-processed, earth abundant absorbing layer for thin-film solar cells," *Energy & Environmental Science*, vol. 5, pp. 5340-5345, 2012.

[50] Y. Sun, Y. Zhang, H. Wang, M. Xie, K. Zong, H. Zheng, *et al.*, "Novel non-hydrazine solution processing of earth-abundant $Cu_2ZnSn(S,Se)_4$ absorbers for thin-film solar cells," *Journal of Materials Chemistry A*, vol. 1, pp. 6880-6887, 2013.

[51] Q. Guo, G. M. Ford, W.-C. Yang, B. C. Walker, E. A. Stach, H. W. Hillhouse, *et al.*, "Fabrication of 7.2% Efficient CZTSSe Solar Cells Using CZTS Nanocrystals," *Journal of the American Chemical Society*, vol. 132, pp. 17384-17386, 2010/12/15 2010.

[52] W. Yang, H.-S. Duan, K. C. Cha, C.-J. Hsu, W.-C. Hsu, H. Zhou, *et al.*, "Molecular Solution Approach To Synthesize Electronic Quality Cu_2ZnSnS_4 Thin Films," *Journal of the American Chemical Society*, vol. 135, pp. 6915-6920, 2013/05/08 2013.

[53] W. Yang, H.-S. Duan, B. Bob, H. Zhou, B. Lei, C.-H. Chung, *et al.*, "Novel Solution Processing of High-Efficiency Earth-Abundant $Cu_2ZnSn(S,Se)_4$ Solar Cells," *Advanced Materials*, vol. 24, pp. 6323-6329, 2012.

[54] Y. Cao, M. S. Denny, J. V. Caspar, W. E. Farneth, Q. Guo, A. S. Ionkin, *et al.*, "High-Efficiency Solution-Processed $Cu_2ZnSn(S,Se)_4$ Thin-Film Solar Cells Prepared from Binary and Ternary Nanoparticles," *Journal of the American Chemical Society*, vol. 134, pp. 15644-15647, 2012/09/26 2012.

[55] W. Ki and H. W. Hillhouse, "Earth-Abundant Element Photovoltaics Directly from Soluble Precursors with High Yield Using a Non-Toxic Solvent," *Advanced Energy Materials*, vol. 1, pp. 732-735, 2011.

[56] J. Minlin, R. Dhakal, L. Yong, P. Thapaliya, and Y. Xingzhong, "Cu_2ZnSnS_4 (CZTS) polycrystalline thin films prepared by sol-gel method," in *Photovoltaic Specialists Conference (PVSC), 2011 37th IEEE*, 2011, pp. 001283-001286.

[57] M. Jiang, Y. Li, R. Dhakal, P. Thapaliya, M. Mastro, J. D. Caldwell, *et al.*, "Cu_2ZnSnS_4 polycrystalline thin films with large densely packed grains prepared by sol-gel method," *Journal of Photonics for Energy*, vol. 1, pp. 019501-019501-6, 2011.

[58] J. Minlin, W. Fanan, L. Fei, L. Guangyong, and Y. Xingzhong, "Bandgap tuning and morphology amelioration of sol-gel derived Cu_2ZnSnS_4 (CZTS) thin films by selenium

incorporation," in *Photovoltaic Specialists Conference (PVSC), 2013 IEEE 39th*, 2013, pp. 2602-2604.

[59] M. Jiang, F. Lan, X. Yan, and G. Li, "$Cu_2ZnSn(S_{1-x}Se_x)_4$ thin film solar cells prepared by water-based solution process," *physica status solidi (RRL) – Rapid Research Letters,* vol. 8, pp. 223-227, 2014.

[60] M. Jiang, K. Tang, and X. Yan, "Characterization of intrinsic ZnO thin film deposited by sputtering and its effects on $CuIn_{1-x}Ga_xSe_2$ solar cells," *Journal of Photonics for Energy,* vol. 2, pp. 028502-1-028502-11, 2012.

[61] C. J. Doona and D. M. Stanbury, "Equilibrium and Redox Kinetics of Copper(II) −Thiourea Complexes," *Inorganic Chemistry,* vol. 35, pp. 3210-3216, 1996/01/01 1996.

[62] P. Bombicz, I. Mutikainen, M. Krunks, T. Leskelä, J. Madarász, and L. Niinistö, "Synthesis, vibrational spectra and X-ray structures of copper(I) thiourea complexes," *Inorganica Chimica Acta,* vol. 357, pp. 513-525, 1/30/ 2004.

[63] J. Madarász, P. Bombicz, M. Okuya, and S. Kaneko, "Thermal decomposition of thiourea complexes of Cu(I), Zn(II), and Sn(II) chlorides as precursors for the spray pyrolysis deposition of sulfide thin films," *Solid State Ionics,* vol. 141–142, pp. 439-446, 5/1/ 2001.

[64] A. Weber, R. Mainz, T. Unold, S. Schorr, and H.-W. Schock, "In-situ XRD on formation reactions of Cu_2ZnSnS_4 thin films," *physica status solidi (c),* vol. 6, pp. 1245-1248, 2009.

[65] S. Chen, J.-H. Yang, X. G. Gong, A. Walsh, and S.-H. Wei, "Intrinsic point defects and complexes in the quaternary kesterite semiconductor $CuZnSnS_4$," *Physical Review B,* vol. 81, p. 245204, 06/08/ 2010.

[66] P. M. P. Salomé, P. A. Fernandes, and A. F. d. Cunha, "Influence of selenization pressure on the growth of $Cu_2ZnSnSe_4$ films from stacked metallic layers," *physica status solidi (c),* vol. 7, pp. 913-916, 2010.

[67] P. M. P. Salomé, P. A. Fernandes, A. F. da Cunha, J. P. Leitão, J. Malaquias, A. Weber, *et al.*, "Growth pressure dependence of $Cu_2ZnSnSe_4$ properties," *Solar Energy Materials and Solar Cells,* vol. 94, pp. 2176-2180, 12// 2010.

[68] A. Weber, R. Mainz, and H. W. Schock, "On the Sn loss from thin films of the material system Cu–Zn–Sn–S in high vacuum," *Journal of Applied Physics,* vol. 107, pp. -, 2010.

[69] A. Redinger, D. M. Berg, P. J. Dale, and S. Siebentritt, "The Consequences of Kesterite Equilibria for Efficient Solar Cells," *Journal of the American Chemical Society,* vol. 133, pp. 3320-3323, 2011/03/16 2011.

[70] K. Wang, O. Gunawan, T. Todorov, B. Shin, S. J. Chey, N. A. Bojarczuk, *et al.*, "Thermally evaporated Cu_2ZnSnS_4 solar cells," *Applied Physics Letters,* vol. 97, pp. -, 2010.

[71] A. Wangperawong, J. S. King, S. M. Herron, B. P. Tran, K. Pangan-Okimoto, and S. F. Bent, "Aqueous bath process for deposition of Cu_2ZnSnS_4 photovoltaic absorbers," *Thin Solid Films,* vol. 519, pp. 2488-2492, 2/1/ 2011.

[72] R. J. Deokate, A. D. Adsool, N. S. Shinde, S. M. Pawar, and C. D. Lokhande, "Structural and Optical Properties of Spray-deposited Cu_2ZnSnS_4 thin Films," *Energy Procedia,* vol. 54, pp. 627-633, // 2014.

[73] S. C. Riha, B. A. Parkinson, and A. L. Prieto, "Compositionally Tunable $Cu_2ZnSn(S_{1-x}Se_x)_4$ Nanocrystals: Probing the Effect of Se-Inclusion in Mixed Chalcogenide Thin Films," *Journal of the American Chemical Society,* vol. 133, pp. 15272-15275, 2011/10/05 2011.

[74] K. Wang, O. Gunawan, T. Todorov, B. Shin, S. J. Chey, N. A. Bojarczuk, *et al.*, "Thermally evaporated Cu_2ZnSnS_4 solar cells," *Applied Physics Letters,* vol. 97, pp. 143508-143508-3, 2010.

[75] I. P. Parkin, L. S. Price, T. G. Hibbert, and K. C. Molloy, "The first single source deposition of tin sulfide coatings on glass: aerosol-assisted chemical vapour deposition using [Sn(SCHCHS)]," *Journal of Materials Chemistry,* vol. 11, pp. 1486-1490, 2001.

[76] L. A. Isac, A. Duta, A. Kriza, I. A. Enesca, and M. Nanu, "The growth of CuS thin films by Spray Pyrolysis," *Journal of Physics: Conference Series,* vol. 61, p. 477, 2007.

[77] M. Bär, B.-A. Schubert, B. Marsen, R. G. Wilks, S. Pookpanratana, M. Blum, *et al.*, "Cliff-like conduction band offset and KCN-induced recombination barrier enhancement at the CdS/Cu2ZnSnS4 thin-film solar cell heterojunction," *Applied Physics Letters,* vol. 99, pp. -, 2011.

[78] M. Grossberg, J. Krustok, J. Raudoja, K. Timmo, M. Altosaar, and T. Raadik, "Photoluminescence and Raman study of $Cu_2ZnSn(Se_xS_{1-x})_4$ monograins for photovoltaic applications," *Thin Solid Films,* vol. 519, pp. 7403-7406, 8/31/ 2011.

[79] M. Bär, B.-A. Schubert, B. Marsen, S. Krause, S. Pookpanratana, T. Unold, *et al.*, "Impact of KCN etching on the chemical and electronic surface structure of Cu_2ZnSnS_4 thin-film solar cell absorbers," *Applied Physics Letters,* vol. 99, pp. -, 2011.

[80] N. B. Chaure, S. Bordas, A. P. Samantilleke, S. N. Chaure, J. Haigh, and I. M. Dharmadasa, "Investigation of electronic quality of chemical bath deposited cadmium sulphide layers used in thin film photovoltaic solar cells," *Thin Solid Films,* vol. 437, pp. 10-17, 8/1/ 2003.

[81] A. Fairbrother, E. García-Hemme, V. Izquierdo-Roca, X. Fontané, F. A. Pulgarín-Agudelo, O. Vigil-Galán, *et al.*, "Development of a Selective Chemical Etch To Improve the Conversion Efficiency of Zn-Rich Cu_2ZnSnS_4 Solar Cells," *Journal of the American Chemical Society,* vol. 134, pp. 8018-8021, 2012/05/16 2012.

[82] G. Zoppi, I. Forbes, R. W. Miles, P. J. Dale, J. J. Scragg, and L. M. Peter, "$Cu_2ZnSnSe_4$ thin film solar cells produced by selenisation of magnetron sputtered precursors," *Progress in Photovoltaics: Research and Applications,* vol. 17, pp. 315-319, 2009.

[83] M. Bär, W. Bohne, J. Röhrich, E. Strub, S. Lindner, M. C. Lux-Steiner, *et al.*, "Determination of the band gap depth profile of the penternary $Cu(In_{(1-X)}Ga_X)(S_YSe_{(1-Y)})_2$ chalcopyrite from its composition gradient," *Journal of Applied Physics,* vol. 96, pp. 3857-3860, 2004.

[84] H. Wei, Z. Ye, M. Li, Y. Su, Z. Yang, and Y. Zhang, "Tunable band gap $Cu_2ZnSnS_{4x}Se_{4(1-x)}$ nanocrystals: experimental and first-principles calculations," *CrystEngComm,* vol. 13, pp. 2222-2226, 2011.

[85] D. A. R. Barkhouse, O. Gunawan, T. Gokmen, T. K. Todorov, and D. B. Mitzi, "Device characteristics of a 10.1% hydrazine-processed $Cu_2ZnSn(Se,S)_4$ solar cell," *Progress in Photovoltaics: Research and Applications,* vol. 20, pp. 6-11, 2012.

[86] T. K. Todorov, J. Tang, S. Bag, O. Gunawan, T. Gokmen, Y. Zhu, *et al.*, "Beyond 11% Efficiency: Characteristics of State-of-the-Art $Cu_2ZnSn(S,Se)_4$ Solar Cells," *Advanced Energy Materials,* vol. 3, pp. 34-38, 2013.

[87] S. Ye, X. Tan, M. Jiang, B. Fan, K. Tang, and S. Zhuang, "Impact of different Na-incorporating methods on $Cu(In,Ga)Se_2$ thin film solar cells with a low-Na substrate," *Applied Optics,* vol. 49, pp. 1662-1665, 2010/03/20 2010.

[88] V. D'Innocenzo, G. Grancini, M. J. P. Alcocer, A. R. S. Kandada, S. D. Stranks, M. M. Lee, *et al.*, "Excitons versus free charges in organo-lead tri-halide perovskites," *Nat Commun,* vol. 5, 04/08/online 2014.

[89] N. Ahn, D. Y. Son, I. H. Jang, S. M. Kang, M. Choi, and N. G. Park, "Highly Reproducible Perovskite Solar Cells with Average Efficiency of 18.3% and Best Efficiency of 19.7% Fabricated via Lewis Base Adduct of Lead(II) Iodide," *Journal of the American Chemical Society,* vol. 137, pp. 8696-8699, Jul 15 2015.

[90] G. E. Eperon, V. M. Burlakov, P. Docampo, A. Goriely, and H. J. Snaith, "Morphological Control for High Performance, Solution-Processed Planar Heterojunction Perovskite Solar Cells," *Advanced Functional Materials,* vol. 24, pp. 151-157, 2014.

[91] Y. Ogomi, A. Morita, S. Tsukamoto, T. Saitho, N. Fujikawa, Q. Shen, *et al.*, "$CH_3NH_3Sn_xPb_{(1-x)}I_3$ Perovskite Solar Cells Covering up to 1060 nm," *Journal of Physical Chemistry Letters,* vol. 5, pp. 1004-1011, Mar 20 2014.

[92] D. Q. Bi, A. M. El-Zohry, A. Hagfeldt, and G. Boschloo, "Unraveling the Effect of PbI_2 Concentration on Charge Recombination Kinetics in Perovskite Solar Cells," *Acs Photonics,* vol. 2, pp. 589-594, May 2015.

[93] Z. Xiao, C. Bi, Y. Shao, Q. Dong, Q. Wang, Y. Yuan, *et al.*, "Efficient, high yield perovskite photovoltaic devices grown by interdiffusion of solution-processed precursor stacking layers," *Energy & Environmental Science,* vol. 7, pp. 2619-2623, 2014.

[94] J. M. Ball, M. M. Lee, A. Hey, and H. J. Snaith, "Low-temperature processed meso-superstructured to thin-film perovskite solar cells," *Energy & Environmental Science,* vol. 6, pp. 1739-1743, 2013.

[95] E. Edri, S. Kirmayer, A. Henning, S. Mukhopadhyay, K. Gartsman, Y. Rosenwaks, *et al.*, "Why Lead Methylammonium Tri-Iodide Perovskite-Based Solar Cells Require a Mesoporous Electron Transporting Scaffold (but Not Necessarily a Hole Conductor)," *Nano Letters,* vol. 14, pp. 1000-1004, Feb 2014.

[96] Z. G. Xiao, C. Bi, Y. C. Shao, Q. F. Dong, Q. Wang, Y. B. Yuan, *et al.*, "Efficient, high yield perovskite photovoltaic devices grown by interdiffusion of solution-processed precursor stacking layers," *Energy & Environmental Science,* vol. 7, pp. 2619-2623, Aug 2014.

[97] S. L. Ye, X. H. Tan, M. L. Jiang, B. Fan, K. Tang, and S. L. Zhuang, "Impact of different Na-incorporating methods on Cu(In,Ga)Se_2 thin film solar cells with a low-Na substrate," *Applied Optics,* vol. 49, pp. 1662-1665, Mar 20 2010.

[98] S. D. Stranks, G. E. Eperon, G. Grancini, C. Menelaou, M. J. P. Alcocer, T. Leijtens, *et al.*, "Electron-Hole Diffusion Lengths Exceeding 1 Micrometer in an Organometal Trihalide Perovskite Absorber," *Science,* vol. 342, pp. 341-344, October 18, 2013 2013.

[99] G. Xing, N. Mathews, S. Sun, S. S. Lim, Y. M. Lam, M. Grätzel, *et al.*, "Long-Range Balanced Electron- and Hole-Transport Lengths in Organic-Inorganic $CH_3NH_3PbI_3$," *Science,* vol. 342, pp. 344-347, October 18, 2013 2013.

[100] Z. Djebbour, A. Darga, A. M. Dubois, D. Mencaraglia, N. Naghavi, J. F. Guillemoles, *et al.*, "Admittance spectroscopy of cadmium free CIGS solar cells heterointerfaces," *Thin Solid Films,* vol. 511, pp. 320-324, Jul 26 2006.

[101] Y. Y. Proskuryakov, K. Durose, B. M. Taele, G. P. Welch, and S. Oelting, "Admittance spectroscopy of CdTe/CdS solar cells subjected to varied nitric-phosphoric etching conditions," *Journal of Applied Physics,* vol. 101, Jan 1 2007.

[102] J. V. Li and D. H. Levi, "Determining the defect density of states by temperature derivative admittance spectroscopy," *Journal of Applied Physics,* vol. 109, Apr 15 2011.

[103] M. Samiee, S. Konduri, B. Ganapathy, R. Kottokkaran, H. A. Abbas, A. Kitahara, *et al.*, "Defect density and dielectric constant in perovskite solar cells," *Applied Physics Letters,* vol. 105, Oct 13 2014.

[104] H. S. Duan, H. P. Zhou, Q. Chen, P. Y. Sun, S. Luo, T. B. Song, *et al.*, "The identification and characterization of defect states in hybrid organic-inorganic perovskite photovoltaics," *Physical Chemistry Chemical Physics*, vol. 17, pp. 112-116, 2015.

[105] H. B. Xu, R. J. Hong, B. Ai, L. Zhuang, and H. Shen, "Application of phosphorus diffusion gettering process on upgraded metallurgical grade Si wafers and solar cells," *Applied Energy*, vol. 87, pp. 3425-3430, Nov 2010.

[106] M. T. Zarmai, N. N. Ekere, C. F. Oduoza, and E. H. Amalu, "A review of interconnection technologies for improved crystalline silicon solar cell photovoltaic module assembly," *Applied Energy*, vol. 154, pp. 173-182, Sep 15 2015.

[107] S. G. Chen, "An efficient sizing method for a stand-alone PV system in terms of the observed block extremes," *Applied Energy*, vol. 91, pp. 375-384, Mar 2012.

[108] G. F. Hou, H. H. Sun, Z. Y. Jiang, Z. Q. Pan, Y. B. Wang, X. D. Zhang, *et al.*, "Life cycle assessment of grid-connected photovoltaic power generation from crystalline silicon solar modules in China," *Applied Energy*, vol. 164, pp. 882-890, Feb 15 2016.

[109] L. J. Geerligs and D. Macdonald, "Base doping and recombination activity of impurities in crystalline silicon solar cells," *Progress in Photovoltaics*, vol. 12, pp. 309-316, Jun 2004.

[110] J. R. Davis, A. Rohatgi, R. H. Hopkins, P. D. Blais, P. Raichoudhury, J. R. Mccormick, *et al.*, "Impurities in Silicon Solar-Cells," *Ieee Transactions on Electron Devices*, vol. 27, pp. 677-687, 1980.

[111] J. W. Bishop, "Microplasma Breakdown and Hot-Spots in Silicon Solar-Cells," *Solar Cells*, vol. 26, pp. 335-349, Sep 1989.

[112] G. Buzanich, M. Radtke, U. Reinholz, H. Riesemeier, A. F. Thunemann, and C. Streli, "Impurities in multicrystalline silicon wafers for solar cells detected by synchrotron micro-beam X-ray fluorescence analysis," *Journal of Analytical Atomic Spectrometry*, vol. 27, pp. 1875-1881, Nov 2012.

[113] A. M. Salama and L. J. Cheng, "The Effects of Titanium Impurities in N+-P Silicon Solar-Cells," *Journal of the Electrochemical Society*, vol. 127, pp. 1164-1167, 1980.

[114] W. P. Lee, E. P. Teh, H. K. Yow, C. L. Choong, and T. Y. Tou, "Enhanced gettering of iron impurities in bulk silicon by using external direct current electric field," *Journal of Electronic Materials*, vol. 34, pp. L25-L29, Jul 2005.

[115] M. I. Asghar, M. Yli-Koski, H. Savin, A. Haarahiltunen, H. Talvitie, and J. Sinkkonen, "Competitive iron gettering between internal gettering sites and boron implantation in CZ-silicon," *Materials Science and Engineering B-Advanced Functional Solid-State Materials*, vol. 159-60, pp. 224-227, Mar 15 2009.

[116] M. L. Jiang, J. M. Wu, F. Lan, Q. Tao, D. Gao, and G. Y. Li, "Enhancing the performance of planar organo-lead halide perovskite solar cells by using a mixed halide source," *Journal of Materials Chemistry A*, vol. 3, pp. 963-967, 2015.

[117] A. Babayigit, D. D. Thanh, A. Ethirajan, J. Manca, M. Muller, H. G. Boyen, *et al.*, "Assessing the toxicity of Pb- and Sn-based perovskite solar cells in model organism Danio rerio," *Scientific Reports*, vol. 6, Jan 13 2016.

[118] L. Kaake, X. D. Dang, W. L. Leong, Y. Zhang, A. Heeger, and T. Q. Nguyen, "Effects of Impurities on Operational Mechanism of Organic Bulk Heterojunction Solar Cells," *Advanced Materials*, vol. 25, pp. 1706-1712, Mar 25 2013.

[119] J. Y. Cho, K. H. Seo, B. H. Kang, and K. Y. Kim, "The Effect of the Purity of Raw Materials on the Purity of Silicon Extracted by Solvent Refining and Centrifugation," *Korean Journal of Metals and Materials*, vol. 50, pp. 907-911, Dec 2012.

[120] J. J. Chang, H. Zhu, B. C. Li, F. H. Isikgor, Y. Hao, Q. H. Xu, *et al.*, "Boosting the performance of planar heterojunction perovskite solar cell by controlling the precursor purity of perovskite materials," *Journal of Materials Chemistry A*, vol. 4, pp. 887-893, 2016.

[121] P. Docampo, F. C. Hanusch, S. D. Stranks, M. Doblinger, J. M. Feckl, M. Ehrensperger, *et al.*, "Solution Deposition-Conversion for Planar Heterojunction Mixed Halide Perovskite Solar Cells," *Advanced Energy Materials*, vol. 4, Oct 7 2014.

[122] N. Tripathi, M. Yanagida, Y. Shirai, T. Masuda, L. Y. Han, and K. Miyano, "Hysteresis-free and highly stable perovskite solar cells produced via a chlorine-mediated interdiffusion method," *Journal of Materials Chemistry A*, vol. 3, pp. 12081-12088, 2015.

[123] H. Yu, F. Wang, F. Y. Xie, W. W. Li, J. Chen, and N. Zhao, "The Role of Chlorine in the Formation Process of "$CH_3NH_3PbI_{3-x}Cl_x$" Perovskite," *Advanced Functional Materials*, vol. 24, pp. 7102-7108, Dec 3 2014.

[124] S. R. Cowan, W. L. Leong, N. Banerji, G. Dennler, and A. J. Heeger, "Identifying a Threshold Impurity Level for Organic Solar Cells: Enhanced First-Order Recombination Via Well-Defined PC84BM Traps in Organic Bulk Heterojunction Solar Cells," *Advanced Functional Materials*, vol. 21, pp. 3083-3092, Aug 23 2011.

[125] M. M. Mandoc, F. B. Kooistra, J. C. Hummelen, B. de Boer, and P. W. M. Blom, "Effect of traps on the performance of bulk heterojunction organic solar cells," *Applied Physics Letters*, vol. 91, Dec 24 2007.

[126] P. K. Johnson, J. T. Heath, J. D. Cohen, K. Ramanathan, and J. R. Sites, "A comparative study of defect states in evaporated and selenized CIGS(S) solar cells," *Progress in Photovoltaics*, vol. 13, pp. 579-586, Nov 2005.

[127] P. T. Erslev, J. W. Lee, W. N. Shafarman, and J. D. Cohen, "The influence of Na on metastable defect kinetics in CIGS materials," *Thin Solid Films,* vol. 517, pp. 2277-2281, Feb 2 2009.

[128] J. Serhan, Z. Djebbour, D. Mencaraglia, F. Couzinie-Devy, N. Barreau, and J. Kessler, "Influence of Ga content on defects in $CuIn_xGa_{1-x}Se_2$ based solar cell absorbers investigated by sub gap modulated photocurrent and admittance spectroscopy," *Thin Solid Films,* vol. 519, pp. 7312-7316, Aug 31 2011.

[129] A. S. Gudovskikh, J. P. Kleider, R. Chouffot, N. A. Kalyuzhnyy, S. A. Mintairov, and V. M. Lantratov, "III-phosphides heterojunction solar cell interface properties from admittance spectroscopy," *Journal of Physics D-Applied Physics,* vol. 42, Aug 21 2009.

[130] M. H. Du, "Efficient carrier transport in halide perovskites: theoretical perspectives," *Journal of Materials Chemistry A,* vol. 2, pp. 9091-9098, 2014.

[131] Y. Z. Xu, L. F. Zhu, J. J. Shi, S. T. Lv, X. Xu, J. Y. Xiao*, et al.*, "Efficient Hybrid Mesoscopic Solar Cells with Morphology-Controlled $CH_3NH_3PbI_{3-x}Cl_x$ Derived from Two-Step Spin Coating Method," *Acs Applied Materials & Interfaces,* vol. 7, pp. 2242-2248, Feb 4 2015.

[132] J. Qing, H. T. Chandran, Y. H. Cheng, X. K. Liu, H. W. Li, S. W. Tsang*, et al.*, "Chlorine Incorporation for Enhanced Performance of Planar Perovskite Solar Cell Based on Lead Acetate Precursor," *Acs Applied Materials & Interfaces,* vol. 7, pp. 23110-23116, Oct 21 2015.

[133] M. Jiang, J. Wu, G. Di, and G. Li, "Nanostructured solar cell based on solution processed Cu_2ZnSnS_4 nanoparticles and vertically aligned ZnO nanorod array," *physica status solidi (RRL) – Rapid Research Letters,* vol. 8, pp. 971-975, 2014.

[134] Y. Han, S. Meyer, Y. Dkhissi, K. Weber, J. M. Pringle, U. Bach*, et al.*, "Degradation observations of encapsulated planar $CH_3NH_3PbI_3$ perovskite solar cells at high temperatures and humidity," *Journal of Materials Chemistry A,* vol. 3, pp. 8139-8147, 2015.

[135] M. O. Reese, A. J. Morfa, M. S. White, N. Kopidakis, S. E. Shaheen, G. Rumbles*, et al.*, "Pathways for the degradation of organic photovoltaic P3HT:PCBM based devices," *Solar Energy Materials and Solar Cells,* vol. 92, pp. 746-752, 7// 2008.

[136] E. Voroshazi, B. Verreet, T. Aernouts, and P. Heremans, "Long-term operational lifetime and degradation analysis of P3HT:PCBM photovoltaic cells," *Solar Energy Materials and Solar Cells,* vol. 95, pp. 1303-1307, 5// 2011.

[137] O. Malinkiewicz, C. Roldán-Carmona, A. Soriano, E. Bandiello, L. Camacho, M. K. Nazeeruddin*, et al.*, "Metal-Oxide-Free Methylammonium Lead Iodide Perovskite-Based Solar Cells: the Influence of Organic Charge Transport Layers," *Advanced Energy Materials,* vol. 4, pp. n/a-n/a, 2014.

[138] J. Cui, F. Meng, H. Zhang, K. Cao, H. Yuan, Y. Cheng, *et al.*, "$CH_3NH_3PbI_3$-Based Planar Solar Cells with Magnetron-Sputtered Nickel Oxide," *ACS Applied Materials & Interfaces,* vol. 6, pp. 22862-22870, 2014/12/24 2014.

[139] J. H. Kim, P.-W. Liang, S. T. Williams, N. Cho, C.-C. Chueh, M. S. Glaz, *et al.*, "High-Performance and Environmentally Stable Planar Heterojunction Perovskite Solar Cells Based on a Solution-Processed Copper-Doped Nickel Oxide Hole-Transporting Layer," *Advanced Materials,* vol. 27, pp. 695-701, 2015.

[140] C. Pacholski, A. Kornowski, and H. Weller, "Self-assembly of ZnO: From nanodots to nanorods.," *Abstracts of Papers of the American Chemical Society,* vol. 224, pp. U351-U351, Aug 18 2002.

[141] K. H. Kim, C. Takahashi, Y. Abe, and M. Kawamura, "Effects of Cu doping on nickel oxide thin film prepared by sol-gel solution process," *Optik,* vol. 125, pp. 2899-2901, 2014.

[142] Y. Y. Zhou, M. J. Yang, W. W. Wu, A. L. Vasiliev, K. Zhu, and N. P. Padture, "Room-temperature crystallization of hybrid-perovskite thin films via solvent-solvent extraction for high-performance solar cells," *Journal of Materials Chemistry A,* vol. 3, pp. 8178-8184, 2015.

[143] I. Sta, M. Jlassi, M. Hajji, and H. Ezzaouia, "Structural, optical and electrical properties of undoped and Li-doped NiO thin films prepared by sol–gel spin coating method," *Thin Solid Films,* vol. 555, pp. 131-137, 3/31/ 2014.

[144] W. J. E. Beek, M. M. Wienk, M. Kemerink, X. Yang, and R. A. J. Janssen, "Hybrid Zinc Oxide Conjugated Polymer Bulk Heterojunction Solar Cells," *The Journal of Physical Chemistry B,* vol. 109, pp. 9505-9516, 2005/05/01 2005.

[145] J. B. Baxter and C. A. Schmuttenmaer, "Conductivity of ZnO Nanowires, Nanoparticles, and Thin Films Using Time-Resolved Terahertz Spectroscopy†," *The Journal of Physical Chemistry B,* vol. 110, pp. 25229-25239, 2006/12/01 2006.

[146] S. Ryu, J. H. Noh, N. J. Jeon, Y. Chan Kim, W. S. Yang, J. Seo, *et al.*, "Voltage output of efficient perovskite solar cells with high open-circuit voltage and fill factor," *Energy & Environmental Science,* vol. 7, pp. 2614-2618, 2014.

[147] F. X. Xie, D. Zhang, H. Su, X. Ren, K. S. Wong, M. Grätzel, *et al.*, "Vacuum-Assisted Thermal Annealing of $CH_3NH_3PbI_3$ for Highly Stable and Efficient Perovskite Solar Cells," *ACS Nano,* vol. 9, pp. 639-646, 2015/01/27 2015.

[148] I. A. Garduño, J. C. Alonso, M. Bizarro, R. Ortega, L. Rodríguez-Fernández, and A. Ortiz, "Optical and electrical properties of lithium doped nickel oxide films deposited by spray pyrolysis onto alumina substrates," *Journal of Crystal Growth,* vol. 312, pp. 3276-3281, 11/1/ 2010.

[149] C.-Y. Chang, C.-Y. Chu, Y.-C. Huang, C.-W. Huang, S.-Y. Chang, C.-A. Chen, *et al.*, "Tuning Perovskite Morphology by Polymer Additive for High Efficiency Solar Cell," *ACS Applied Materials & Interfaces,* vol. 7, pp. 4955-4961, 2015/03/04 2015.

[150] M. K. Debanath and S. Karmakar, "Study of blueshift of optical band gap in zinc oxide (ZnO) nanoparticles prepared by low-temperature wet chemical method," *Materials Letters,* vol. 111, pp. 116-119, 11/15/ 2013.

[151] S. Shayesteh and A. Dizgah, "Effect of doping and annealing on the physical properties of ZnO:Mg nanoparticles," *Pramana,* vol. 81, pp. 319-330, 2013/08/01 2013.

[152] C. J. Brabec, A. Cravino, D. Meissner, N. S. Sariciftci, T. Fromherz, M. T. Rispens, *et al.*, "Origin of the Open Circuit Voltage of Plastic Solar Cells," *Advanced Functional Materials,* vol. 11, pp. 374-380, 2001.

[153] M. Jiang, J. Wu, F. Lan, Q. Tao, D. Gao, and G. Li, "Enhancing the performance of planar organo-lead halide perovskite solar cells by using a mixed halide source," *Journal of Materials Chemistry A,* vol. 3, pp. 963-967, 2015.

[154] U. Bach, D. Lupo, P. Comte, J. E. Moser, F. Weissortel, J. Salbeck, *et al.*, "Solid-state dye-sensitized mesoporous TiO_2 solar cells with high photon-to-electron conversion efficiencies," *Nature,* vol. 395, pp. 583-585, 10/08/print 1998.

[155] M. Xiao, F. Huang, W. Huang, Y. Dkhissi, Y. Zhu, J. Etheridge, *et al.*, "A Fast Deposition-Crystallization Procedure for Highly Efficient Lead Iodide Perovskite Thin-Film Solar Cells," *Angewandte Chemie,* vol. 126, pp. 10056-10061, 2014.

[156] L. Yang, U. B. Cappel, E. L. Unger, M. Karlsson, K. M. Karlsson, E. Gabrielsson, *et al.*, "Comparing spiro-OMeTAD and P3HT hole conductors in efficient solid state dye-sensitized solar cells," *Physical Chemistry Chemical Physics,* vol. 14, pp. 779-789, 2012.

[157] W. H. Nguyen, C. D. Bailie, E. L. Unger, and M. D. McGehee, "Enhancing the Hole-Conductivity of Spiro-OMeTAD without Oxygen or Lithium Salts by Using Spiro(TFSI)$_2$ in Perovskite and Dye-Sensitized Solar Cells," *Journal of the American Chemical Society,* vol. 136, pp. 10996-11001, 2014/08/06 2014.

[158] K. J. Chen, T. H. Fang, F. Y. Hung, L. W. Ji, S. J. Chang, S. J. Young, *et al.*, "The crystallization and physical properties of Al-doped ZnO nanoparticles," *Applied Surface Science,* vol. 254, pp. 5791-5795, 7/15/ 2008.

[159] T. Nakada and A. Kunioka, "Direct evidence of Cd diffusion into Cu(In,Ga)Se_2 thin films during chemical-bath deposition process of CdS films," *Applied Physics Letters,* vol. 74, pp. 2444-2446, 1999.

[160] C. X. Xiao, C. S. Jiang, H. Moutinho, D. Levi, Y. F. Yan, B. Gorman, *et al.*, "Locating the electrical junctions in Cu(In,Ga)Se_2 and $Cu_2ZnSnSe_4$ solar cells by scanning capacitance spectroscopy," *Progress in Photovoltaics,* vol. 25, pp. 33-40, Jan 2017.

[161] B. Shin, N. A. Bojarczuk, and S. Guha, "On the kinetics of $MoSe_2$ interfacial layer formation in chalcogen-based thin film solar cells with a molybdenum back contact," *Applied Physics Letters,* vol. 102, Mar 4 2013.

[162] J. J. Scragg, T. Kubart, J. T. Watjen, T. Ericson, M. K. Linnarsson, and C. Platzer-Bjorkman, "Effects of Back Contact Instability on Cu_2ZnSnS_4 Devices and Processes," *Chemistry of Materials,* vol. 25, pp. 3162-3171, Aug 13 2013.

[163] B. Shin, Y. Zhu, N. A. Bojarczuk, S. J. Chey, and S. Guha, "Control of an interfacial $MoSe_2$ layer in $Cu_2ZnSnSe_4$ thin film solar cells: 8.9% power conversion efficiency with a TiN diffusion barrier," *Applied Physics Letters,* vol. 101, Jul 30 2012.

[164] F. Y. Liu, K. W. Sun, W. Li, C. Yan, H. T. Cui, L. X. Jiang, *et al.*, "Enhancing the Cu_2ZnSnS_4 solar cell efficiency by back contact modification: Inserting a thin TiB_2 intermediate layer at Cu_2ZnSnS_4/Mo interface," *Applied Physics Letters,* vol. 104, Feb 3 2014.

[165] J. H. Heo and S. H. Im, "$CH_3NH_3PbI_3$/poly-3-hexylthiophen perovskite mesoscopic solar cells: Performance enhancement by Li-assisted hole conduction," *Physica Status Solidi-Rapid Research Letters,* vol. 8, pp. 816-821, Oct 2014.

[166] J. H. Kim, P. W. Liang, S. T. Williams, N. Cho, C. C. Chueh, M. S. Glaz, *et al.*, "High-Performance and Environmentally Stable Planar Heterojunction Perovskite Solar Cells Based on a Solution-Processed Copper-Doped Nickel Oxide Hole-Transporting Layer," *Advanced Materials,* vol. 27, pp. 695-701, Jan 27 2015.

[167] H. K. Park and J. Heo, "Improved efficiency of aluminum doping in ZnO thin films grown by atomic layer deposition," *Applied Surface Science,* vol. 309, pp. 133-137, Aug 1 2014.

[168] M. Eskandari, V. Ahmadi, S. Kohnehpoushi, and M. Y. Rad, "Improvement of ZnO nanorod based quantum Dot (cadmium sulfide) sensitized solar cell efficiency by aluminum doping," *Physica E-Low-Dimensional Systems & Nanostructures,* vol. 66, pp. 275-282, Feb 2015.

[169] G. Srinet, R. Kumar, and V. Sajal, "Effects of aluminium doping on structural and photoluminescence properties of ZnO nanoparticles," *Ceramics International,* vol. 40, pp. 4025-4031, Apr 2014.